LOCKHEED MARTIN

LOCKHEED MARTIN MISSILES & SPACE

Contract No.
DE-AC03-91SF18852

GPHS - RTGs

In Support of the

Cassini RTG Program

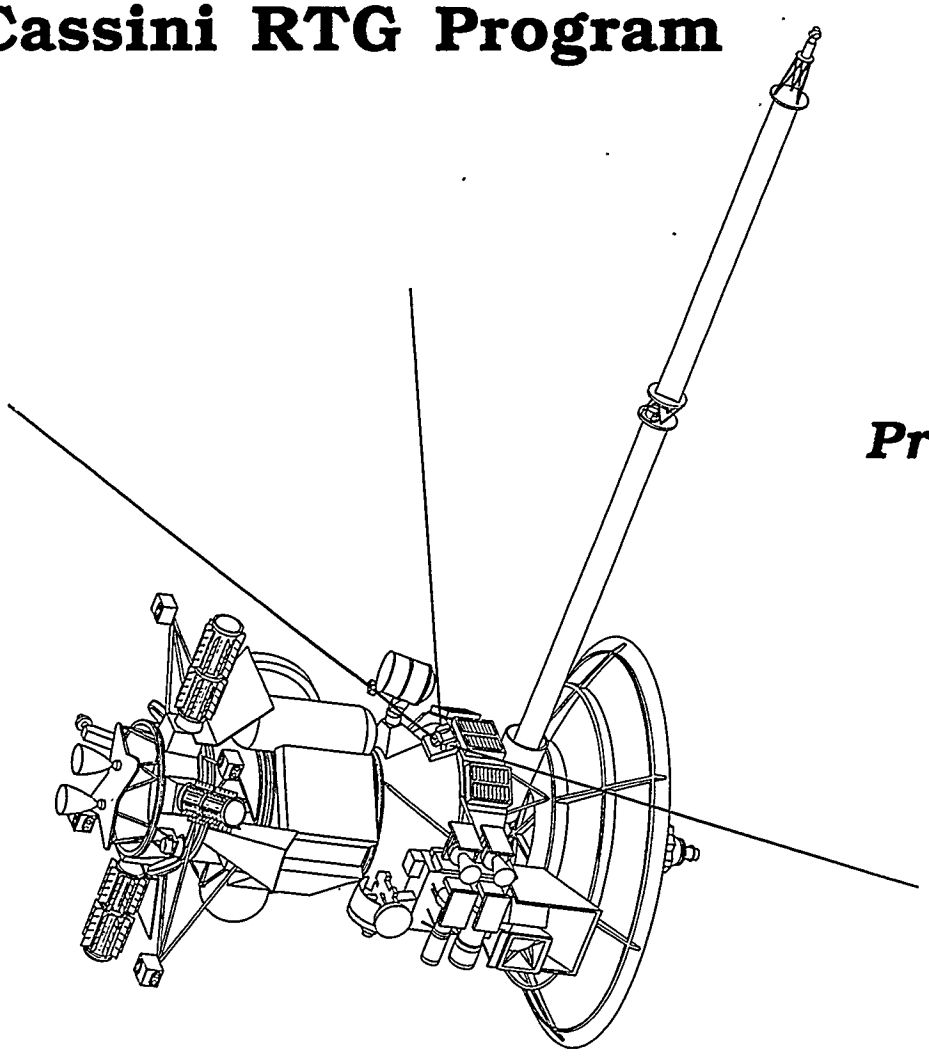

Semi Annual Technical Progress Report

Document No. RR16

1 April 1996
through
29 September 1996

20 October 1996

Space Power Programs

Cassini RTG Program CDRL Transmittal

TO:
U.S. Department of Energy
Lawrence Livermore Nat'l Lab
7000 East Ave., Bldg. 311 L-293
Attention: Ken Quitoriano

DISTRIBUTION:

Symbol	*Copies*
A	5
B	1
C	1
H	2
J	24
K	1

Cassini RTG Program
Contract No: DE-AC03-91SF18852

In Reply Refer to: **CON#1718**
Date: **20 October 1996**

CDRL Number: **Reporting Requirement 4.F (Document No. RR16)**

Title: **Semi Annual Technical Progress Report (1 April through 29 September 1996)**

Approval Requirements:

Approval ☐ None ☒

Contract Period: **11 January 1991 through 30 April 1998**

Approved: R. J. Hemler, Manager
Space Power Programs

Internal Distribution:
Technical Report List

From: Lockheed Martin Missiles & Space
Room 10B50 Building B
720 Vandenberg Road
King of Prussia, PA 19406

Signature:
Joseph M. Waks
Contracts Manager

Semi Annual Technical Report

Contract No.
DE-AC03-91SF18852

GPHS-RTGs in Support of the Cassini Mission

Document No. RR16

1 April 1996
through
29 September 1996

Prepared for:

U.S. Department of Energy
Oakland Operations Office
1301 Clay Street
Oakland, CA 94612-5208

Prepared by:

Lockheed Martin Missiles & Space
P.O. Box 8555
Philadelphia, PA 19101

LOCKHEED MARTIN

Space Power Programs

Semi Annual Technical Progress Report

The technical progress achieved during the period 1 April through 29 September 1996 on Contract No. DE-AC03-91SF18852, Radioisotope Generators and Ancillary Activities is described herein.

This report is organized by the program task structure as follows:

Table of Contents

List of Illustrations

Figure **Page**

List of Illustrations (Cont'd)

Figure **Page**

List of Illustrations (Cont'd)

Figure **Page**

List of Illustrations (Cont'd)

Figure **Page**

List of Tables

List of Tables (Cont'd)

Task 1

Spacecraft Integration and Liaison

Semi Annual Technical Report
Progress by Major Task

TASK 1 SPACECRAFT INTEGRATION AND LIAISON

Magnetics acceptance testing of the F-2 RTG took place at Mound during this reporting period. Prior to the test, JPL specification revisions were issued concerning instrumentation accuracy, the sequencing of acceptance tests, and the selection of magnetometers to be used to determine compliance with test limits. Instrumentation accuracy requirements were revised to be compliant with the capabilities of the currently available instruments. The test sequencing revision was provided to allow greater test scheduling flexibility. The magnetometers located horizontally from the RTG are to be used for compliance determination and those inclined from the horizontal plane are for engineering information only. After evaluating F-2 test data it was evident that one of the six measurements in one RTG position exceeded the 78 nanotesla limit by less than one percent when the RTG current was determined using the minimum beginning of mission power. JPL indicated that the rated current at Saturn orbit insertion (a lower value) should be used along with the average of the measurements to determine specification compliance. With this guidance, the F-2 RTG as well as the F-5 RTG were in compliance with JPL magnetics requirements.

During this reporting period, JPL consulted with LMMS concerning the possible effects on the RTGs of oscillations in the spacecraft engine thrust levels. Such oscillations may occur during limited periods of engine operation. LMMS personnel reviewed available records and spacecraft test data supplied by JPL. Based on this information and data, it is doubtful the thrust oscillation described by JPL and the resulting loads reaching the RTG would be cause for serious concern. A final confirmation must be based on JPL data and test results which are still pending.

Task 2

Engineering Support

TASK 2 ENGINEERING SUPPORT

RTG Fuel Form, Fueling, and Test Support/Liaison

Work continued, as necessary, on the evaluation and disposition of fuel processing related non conformances at LANL.

Discussions were held with Oak Ridge National Laboratory (ORNL) personnel related to gathering data concerning widening the clad vent set welding vent notches. The data requested was related to weld bead thickness for vent hole sizes corresponding to the largest openings permitted by drawing tolerances. ORNL performed some additional testing to develop the requested information. The widened vent hole size was approved and subsequently was adopted for flight hardware use.

During this reporting period LMMS continued to provide support for RTG assembly and test operations at Mound. Changes to assembly and test operations manuals were reviewed and approved. Some changes to the sequence of testing, calibration of magnetometers, and acceptance criteria required coordination with JPL as well as agreement on the changes required to governing specifications.

Direct assistance was provided to Mound in resolving the cause of problems with the vacuum system for the IAAC, and in defining proposed modifications. After system modifications were completed and the system was prepared for production use, LMMS personnel visited Mound to observe a demonstration of the system and its response to up-set conditions. The demonstrations were acceptable and preparations proceeded to return the system to production use.

LMMS also assisted Mound in preparing documentation for the F-5 Buy-Off Review, which was held during this reporting period. Test preparations and procedures were reviewed for the planned start of F-2 dynamic testing at Mound. Agreement was reached on various aspects of the hardware test set up and changes to the test procedures.

LMMS supported the fueling of the E-7 ETG at Mound. The E-7 ETG, when opened at Mound, showed no evidence of internal contamination and fueling proceeded. A leak

was detected after the inboard dome was installed and the RTG pressurized. LMMS recommended the C-seal and dome be replaced with the spares available at Mound. The F-7 leak rate was within specified values after the hardware was replaced. The C-seal and pressure dome are to be returned to LMMS for evaluation.

Specifications and Drawings

ECNs were prepared and processed through CCB which affected the following:

a) Clarification of ETG and RTG requirements

b) All unicouple activities

c) Support of System Testing at Mound

d) Ground Support Equipment for the Cape

Prior to magnetic testing, the F-2 gas management flex hose could not be removed from the fitting saver assembly. An evaluation of the hose-to-fitting saver joint was initiated and it was determined that a flared joint (rather than the flareless joint) would better meet all requirements. As a result, a new modified fitting adapter drawing was prepared and issued. This change also required ECNs to be prepared and processed through CCB for the following drawings:

1) Fitting saver assembly

2) Flexible hose

3) Flexible hose assembly

4) Gas Management Assembly

5) Shell Sub Assembly

6) ETG Assembly

7) RTG Assembly

Task 3

Safety

TASK 3 SAFETY ANALYSIS TASK

The safety analysis task is comprised of four major activities: 1) Launch Accident Analysis; 2) Reentry Analysis; 3) Consequence and Risk Analysis and 4) the Safety Test Program. An overview of the significant issues related to this task for this period, followed by details in each of the four major activities, is provided in the following subsections.

A listing of the INSRP meetings held this year through September 1996 is provided in Table 3-1.

Table 3-1. Safety Analysis Task – Completed INSRP Reviews

Date	*Review*
17-19 January 1996	INSRP Review of LASEP-T and Out-of-Orbit Preliminary Analysis Results
13-14 February 1996	RESP Review of VVEJGA and Out-of-Orbit Preliminary Reentry Analysis Results
7-8 May 1996	INSRP Review of the Sandia National Laboratory Liquid Propellant FIREBALL Model
6 June 1996	RESP Review of RTG Reentry Analysis Results
28 August 1996	INSRP Coordinator and Panel Chairmen Draft FSAR Debriefing
29 August 1996	INSRP Briefing of the Full Stack Intact Impact
4 September 1996	MET/BEES Draft FSAR Debriefing
5 September 1996	PSSP/LASP Draft FSAR Debriefing

Draft Final Safety Analysis (DFSAR) Report

The DFSAR (Volume I, Reference Design Document; Volume II, Accident Model Document; and Volume III, Nuclear Risk Analysis Document) was prepared and submitted first as a Draft for Approval (CDRL C.2) and finally, with DOE comments incorporated, was issued on 3 July 1996. Comments on this document were then received from INSRP, NASA-JPL, NASA-LeRC, and Sandia National Labs. These comments were dispositioned for inclusion in the Final Safety Analysis Report. Preparation of the Final Safety Analysis Report (FSAR) was initiated during this reporting period for delivery in November 1996.

Launch Accident Analysis

The launch accident analysis effort during this reporting period centers on the execution of LASEP-T code for the variability-only simulation reported in the DFSAR and for the variability-only and variability/uncertainty runs for the FSAR, and the modeling of several accident scenarios whose environments are being finalized. These accident model developments include SRMU propellant fallback, full stack intact impact, SV collateral damage, RTG impact within the payload fairing, and Sandia fireball comparative analyses. Discussions of these activities are provided below.

LASEP-T Code Simulations

As part of the verification process, LASEP-T Revision 2.0 variability-only source terms results were compared against detailed tracing output. Additional runs were performed to verify the maximum release versus the initial seed used to start the run. These additional studies were used primarily to analyze the release distributions at several standard deviations from the mean.

Documentation of the Revision 2.0 models was completed during this reporting period. Variability-only simulations were performed with the Revision 2.0 code for 11 composite accident cases (cases 0.1 through 1.9) reported in the Draft FSAR.

Results of the Draft FSAR simulation indicate that large fuel releases are governed by the SV intact impact (SVII) event which occurs in all composite accident cases, but at a very low probability. In order to obtain sufficient statistical representation of this event in the simulation, a 200,000 trial run was performed for case 1.1 - Total Boost Vehicle Destruct, as compared to the typical 10,000 trials and the results are included in the FSAR.

The Revision 2.0 code was updated to include a correction for RTG module dispersion calculations following at-altitude Centaur explosion and fragment impact as well as to remove heterogeneous agglomeration effects from the LMMS fireball model. This Revision 3.0 code was then exercised for variability-only simulations for all accident cases reported in the Draft FSAR for final incorporation into the FSAR. Uncertainty simulations were also made for cases 0.1/0.2 - On Pad Explosion, case 1.1, and case 1.3 - Total Boost Vehicle Destruct with Aft Segment Impact.

SRMU Propellant Fallback

The development of the SRMU propellant fallback model continued in this reporting period. A new algorithm was implemented to determine the set of conditions which can be used to eliminate certain trajectories that will not lead to coincident impact of SRMU propellant with modules. This new algorithm will greatly reduce computational run time needed to determine the coincident impact probability. Time distributions were extracted from the LASEP-T trials for used in the calculation of impact timings between modules and SRMU fragments.

Hydrocode results of SRMU fragments impacting modules received from Orbital Sciences Corporation (OSC) were reviewed in order to develop a fueled clad damage database that will encompass a range of impact configurations, such as impact velocity, fragment mass and thickness, surface type, burning versus non-burning fragment, etc. Analyses to date indicate that direct impact of the large propellant sections on the module produces significant fueled clad distortions, however, the blast portion of the environment seems to have little effect. Modules located on concrete surface are also subjected to much larger damage than modules on sand, including the near-miss configuration. Additional hydrocode analyses are being performed at OSC to assist in further understanding of these various impact scenarios.

Full Stack Intact Impact

An early assessment of the response of the GPHS-RTG to the full stack intact impact (FSII) of Titan IV launch vehicle was performed in order to provide NASA with information to support the decision to proceed with ground system enhancements at CCAS. The probability of FSII occurrences and the specified vehicle impact characteristics were defined by NASA. The subsequent blast environments and their effects on the RTGs were determined by JPL and OSC, respectively. Based on these FSII definitions, a Monte Carlo simulation model was developed and executed, consistent with the approach used to evaluate other Cassini launch accidents.

Under most conditions, the Titan IV launch vehicle can impact the ground surface either with tail-first or nose-first. For tail-first impact cases, an ADS of the entire vehicle would be activated within milliseconds of initial vehicle contact with ground. The ADS will, in most cases, remove the RTG housing, resulting in a free fall of modules to the ground. For nose-first impacts, the insult environment for RTGs are similar to that for space vehicle intact

impacts (SVIIs). For this preliminary assessment, SVII was modeled for both impact geometries, resulting in a more conservative estimate of the source terms.

The FSII event also results in the fragmentation and dispersion of SRMU segments which may impact RTGs on the ground. The fragment sizes and the corresponding ejection velocities for each of the aft, center and forward segments were selected in each Monte Carlo simulation trial such that their cumulative mass equal the total mass of the segment at the given MET when the vehicle impacts the ground. The trajectory of each fragment was then calculated to determine its impact location and proximity to RTGs on the ground. Fueled clad damage assessment was made based on the solid propellant impact hydrocode analyses performed by OSC for the SRMU propellant fallback task described above. The effects of solid propellant fires on fueled clads was not considered in this study.

SV Collateral Damage

The SV collateral damage model has been developed to address the threat environment which occurs when the propellant and pressurant tanks on the SV are damaged by fragments produced by failure of the Centaur or an SRMU. This environment is applicable to each of the Phase 0 and Phase 1 composite accident cases.

As defined in the Databook, the probability of failure (POF) of the pressurant tanks is a function of the fragment energies produced by the Centaur explosion. Analysis performed to determine the range of this POF shows that based on the mean Centaur overpressure, the POF for the bipropellant pressurant tank is between 0.0025 and 0.094, while the POF for the monopropellant pressurant tank is between 0.0018 and 0.14.

Based on the SV layout, the overpressure from the bipropellant pressurant tank affects RTGs 1 and 2. The SV PMS structure shields RTG 3 from the effects of this tank. The monopropellant pressurant tank overpressure was assessed by the Databook as benign. The end dome of the bipropellant pressurant tank is the only threat to RTG 2, while fragments from the monopropellant pressure tank affect RTGs 1 and 3 only.

Preliminary LASEP-T runs including SV collateral damage effects for composite accident case 1.1 indicate that this environment has a very small influence on predicted release probability or source terms. The bipropellant pressurant tank failed in 270 of 17,390 trials while the monopropellant pressurant tank failed 388 times with only one trial in which a monopropellant pressurant tank fragment struck an RTG.

Sandia Fireball Model Comparative Assessment

An advanced liquid fireball model has been developed by SNL (Figure 3-1) which incorporates refinements in the treatment of aerosol physics and combustion thermodynamics from the LMMS model employed in the current FSAR analyses. A series of studies have been performed comparing the post-fireball particle size distributions predicted by the LMMS and SNL models.

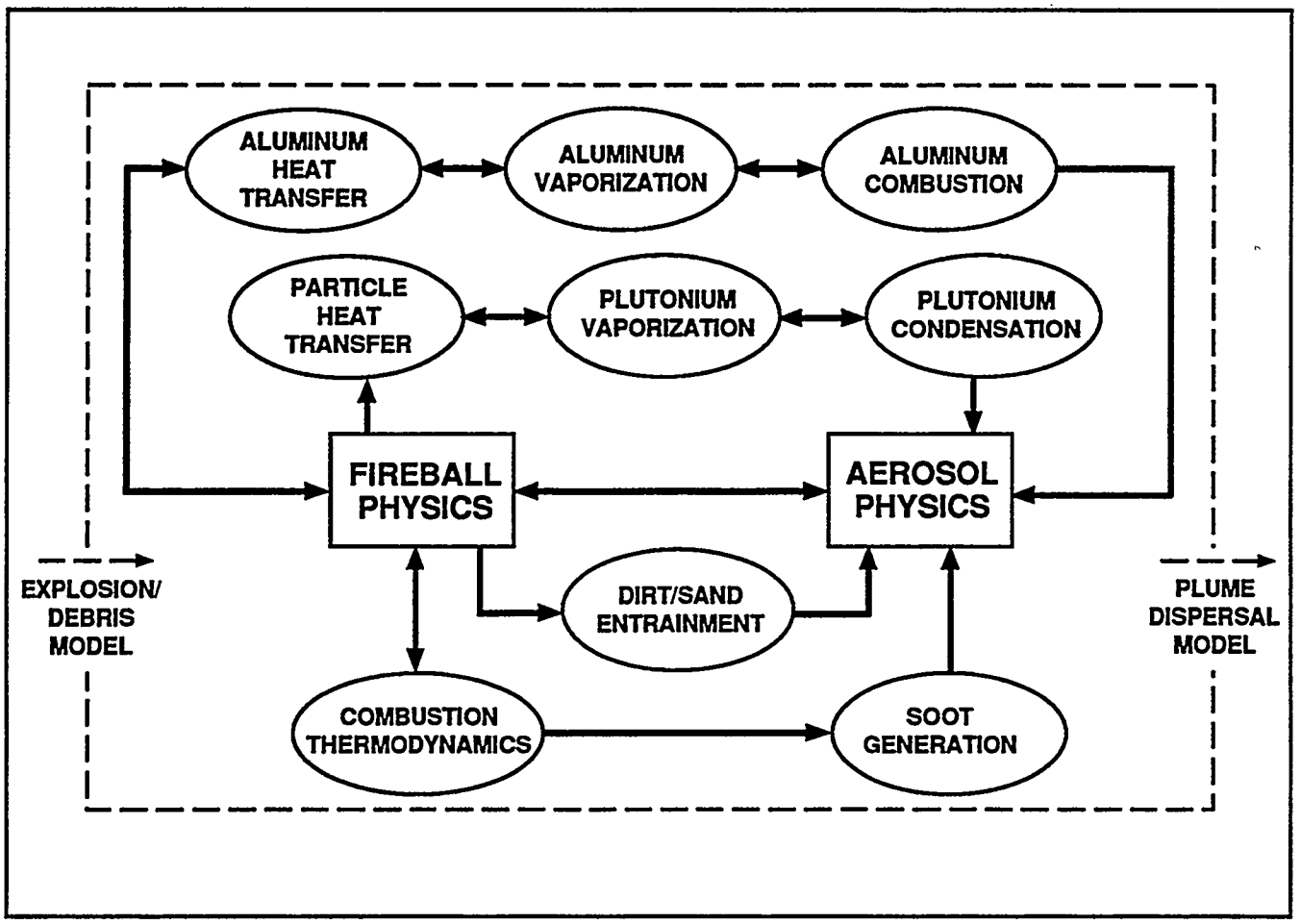

Figure 3-1. Schematic of the Fireball Model

The sensitivity of SNL model parameters was first examined in order to select the nominal (baseline) values for the critical parameters for comparative studies. A LASEP-T variability-only run for case 1.1 was conducted where the first 2,000 trials with releases were examined. A total of 161 of these trials contain a release in the presence of a core (type 2), SV (type 3), or core + SV (type 4) fireball. Given the relatively small mass of SV propellant compared to the core, types 2 and 4 releases were lumped together as core fireball releases in the comparative studies.

Pre-fireball particle size distributions for each of the 161 releases were analyzed with the Sandia fireball model with a set of initial conditions representative of minimal heterogeneous agglomeration (i.e., agglomeration with non-plutonium particulates). This provided a baseline comparison against the LMMS fireball model which was modified during this reporting period to exclude heterogeneous agglomeration effects. The relative impact of source term modifications on health consequences as the result of a fireball was evaluated by calculating a mass weighted Inhalation Effective Dose (IED) from the post-fireball source term distributions generated by the LMMS and Sandia fireball models.

Comparative studies provide a first order comparison between the models utilizing the dose effectiveness associated with one of the principal pathways for dose delivery, i.e., inhalation. Results indicate that for a low heterogeneous agglomeration condition the two models agree to within 50% across the full range of IED values, corresponding to the full range of mass values within the 161 trial sample set.

EGA Reentry Analysis

Intermediate Trajectory: Previous aero/thermo/structural analyses predicted that the GPHS aeroshell will survive the shallow ($\gamma = -7°$) trajectory and structurally fail on the steep ($\gamma = -90°$). An intermediate trajectory ($\gamma = -20°$) was selected (based on structural failure criteria) for additional analyses in order to establish the nominal survive/fail path angle boundary. Figure 3-1 shows the velocity/altitude profile of the three trajectories. Analysis of the intermediate trajectory is now complete. Some comparative results are presented below.

The trajectory points that were selected for CFD analyses are shown in Figure 3-2. Analyses for the intermediate trajectory did not continue past the seventh CFD point because of predicted structural failure. From tables of CFD solutions (solutions were obtained for three selected wall-temperature distributions at each trajectory point) the SINRAP in-depth transient heating code computes the aeroshell temperature history by iteratively solving the surface energy balance (SEB). SINRAP also integrates the ablation rate to obtain surface recession.

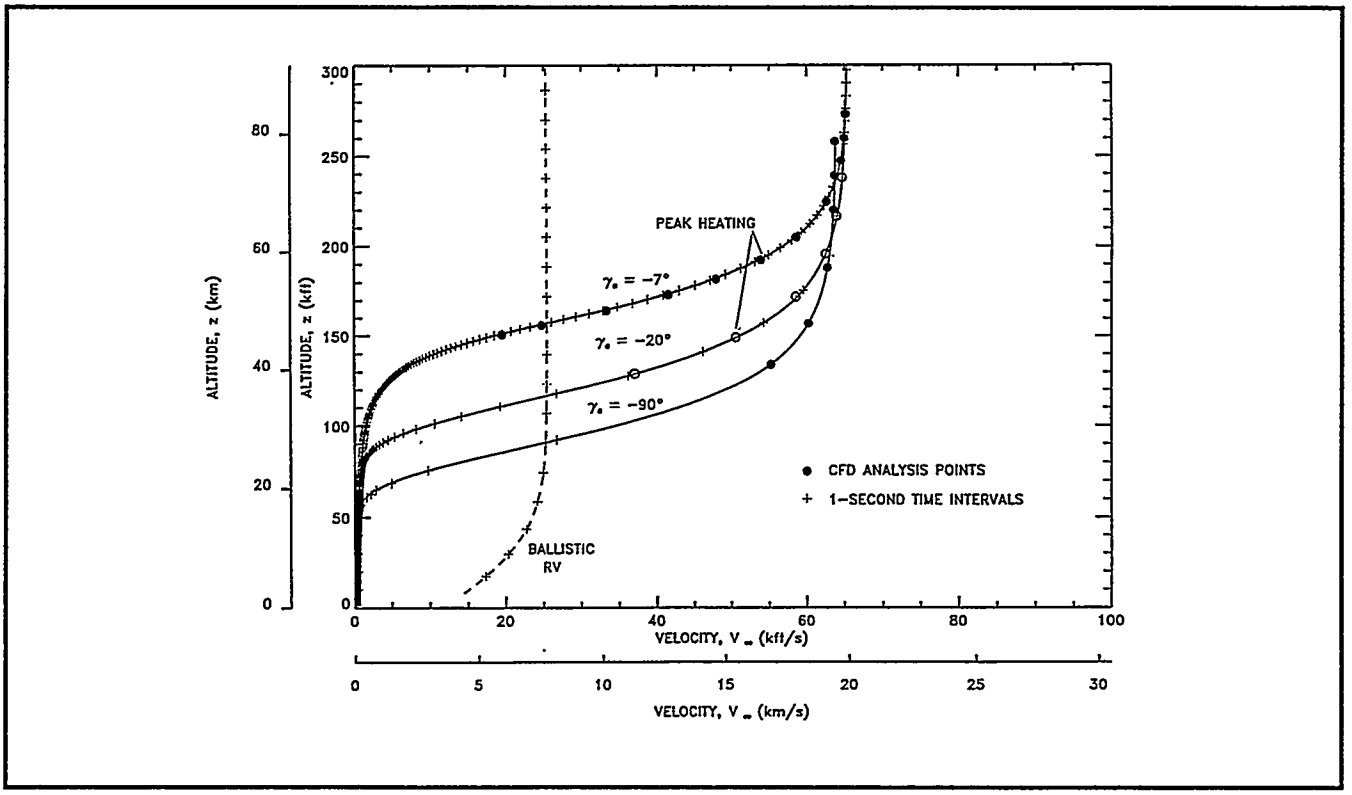

Figure 3-2. Selected Points on the Steep, Intermediate, and Shallow Trajectories for CFD (RACER / LORAN-C) Analyses

The components of the heat flux to the surface of the GPHS module for the steep, intermediate, and shallow trajectories, are shown in Figure 3-3. Similar to the steep trajectory, radiation was found to be the dominant heat source on the intermediate trajectory, approaching 10,000 BTU/(ft^2-sec). The total heat flux history is shown in Figure 3-4. The aeroshell passes through peak-heating at approximately 6 seconds on the intermediate trajectory. The ablation-rate history for the steep, intermediate, and shallow trajectories is shown in Figure 3-5. The ablation-rate history is approximately linearly proportional to the total heat flux history (from the surface energy balance) as is evident by comparing Figure 3-5 with Figure 3-4.

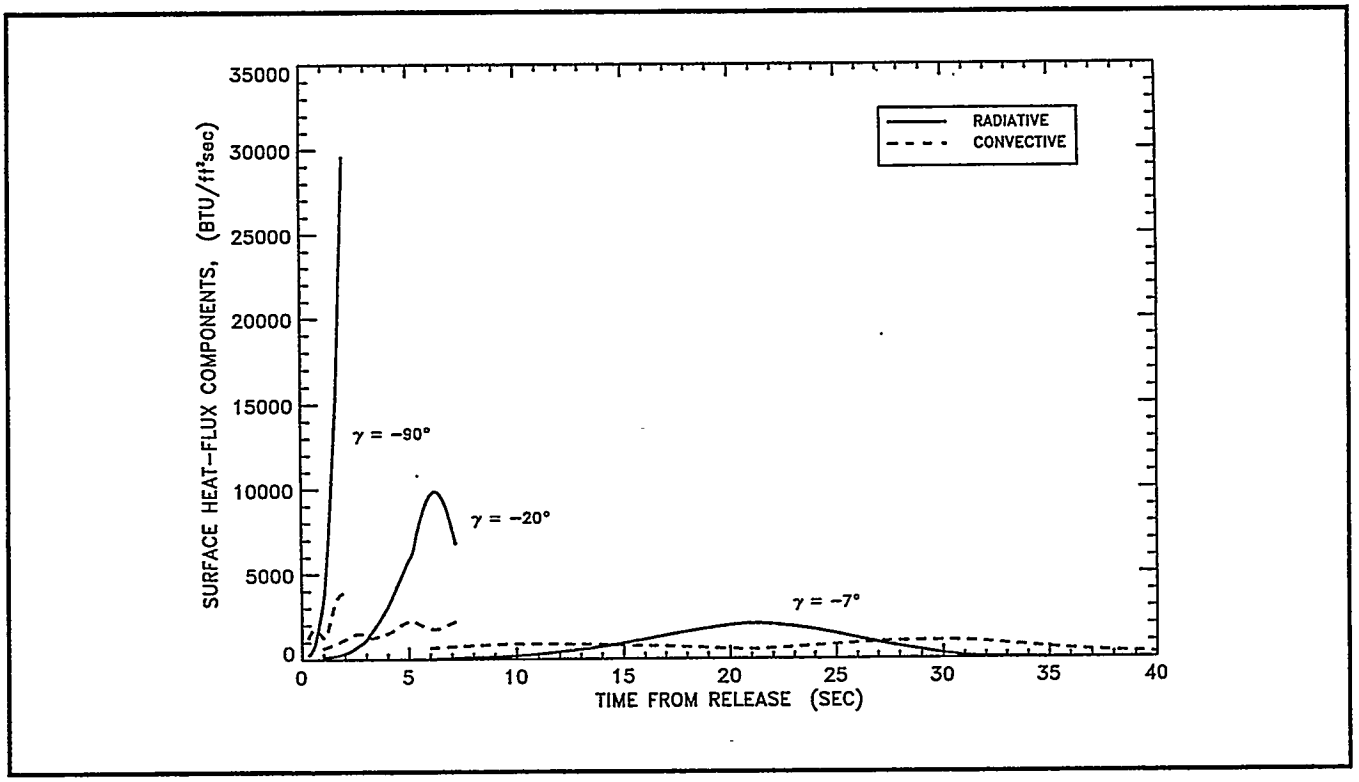

Figure 3-3. Comparison of the Radiative and Convective (Gas Conduction and Diffusion) Heat-Flux Components for the Steep, Intermediate, and Shallow Trajectories

GIS CFD Analyses: Analyses are now in progress to assess the aerothermostructural performance of the graphite impact shell (GIS) under the assumption that the GIS is released following failure of the GPHS aeroshell. Coupled RACER (flowfield) and LORAN-C (radiation) solutions are being obtained for a non-spinning, broad-side stable, GIS. Although the GIS would probably be spinning, the non-spinning analysis will be "worst-case" for survival to impact. A broad-side stable orientation was selected because it is far more likely than edge-on stable and more stressing than random tumbling.

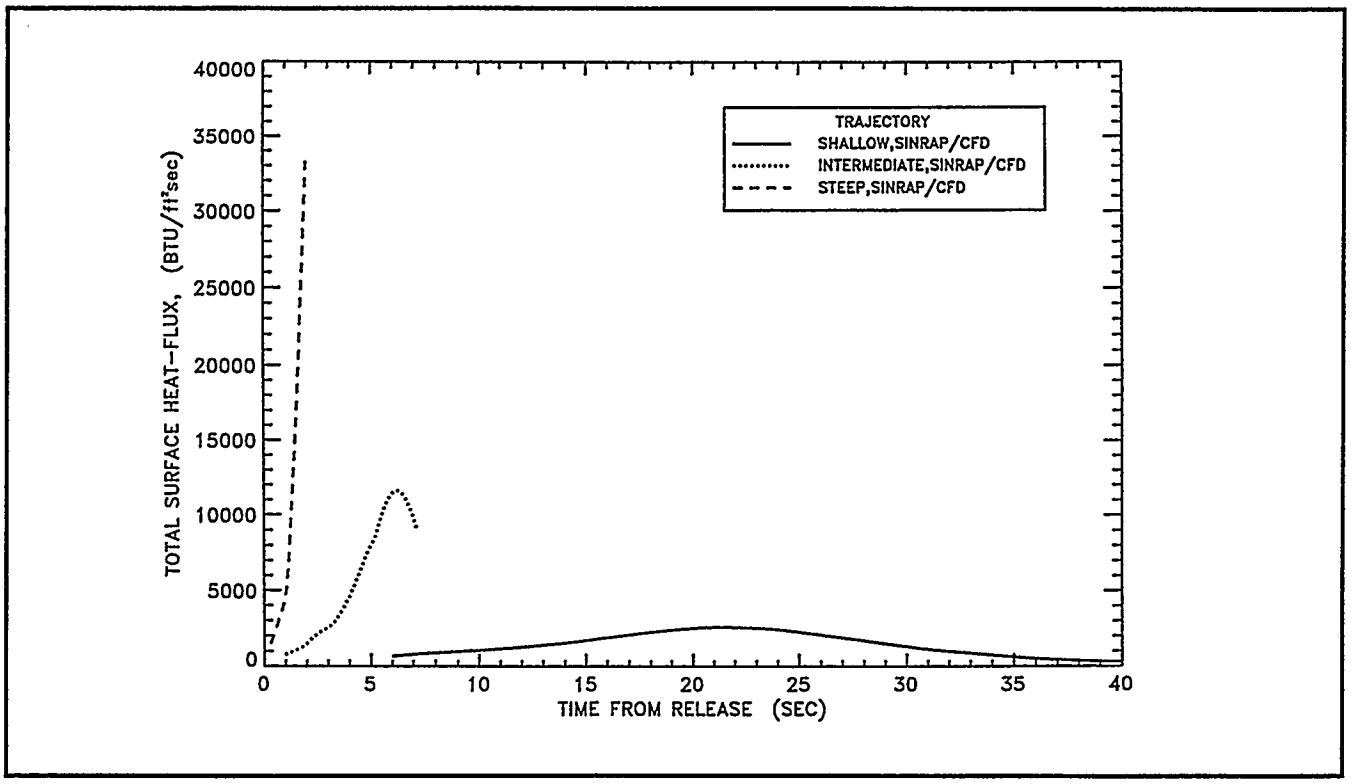

Figure 3-4. Comparison of the Total Heat-Flux History along the Steep, Intermediate, and Shallow Trajectories

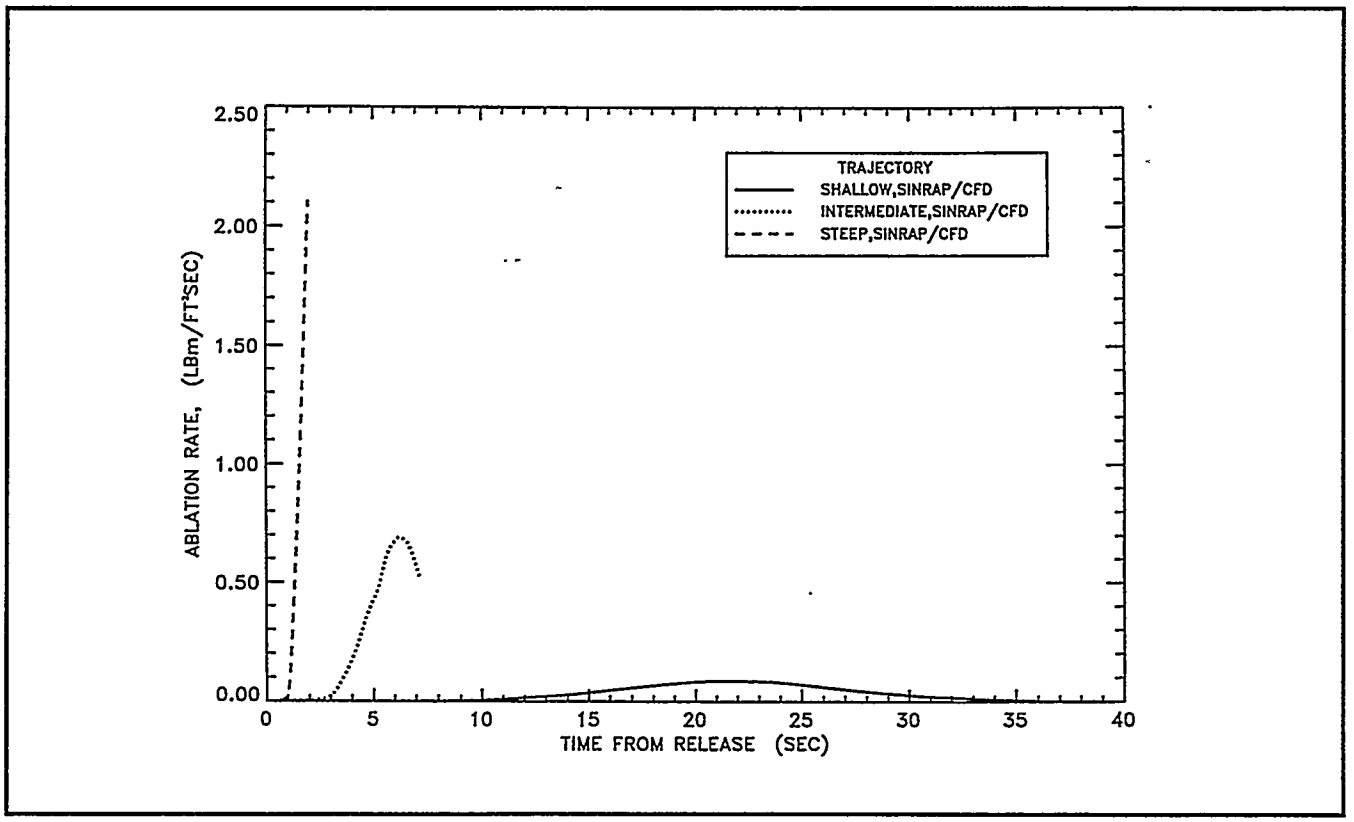

Figure 3-5. Comparison of the Ablation-Rate History along the Steep, Intermediate, and Shallow Trajectories

A two-dimensional version of the axisymmetric RACER code has been developed to compute the flow about an infinite cylinder. Test cases, such as shown in Figure 3-6, were performed to validate the development of the two-dimensional option. Figure 3-6 also shows that for two-dimensional flow, compared to axisymmetric flow, the bow shock is further from the body.

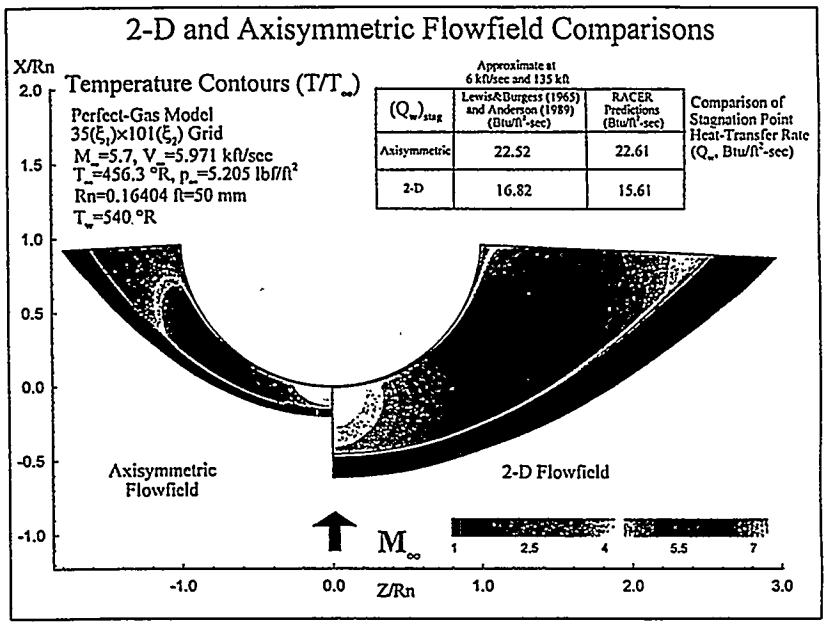

Figure 3-6. One of the Test Cases for Validation of the Two-Dimensional Version of RACER for GIS Analyses

GIS computations were initiated at the time of predicted structural failure on the steep trajectory. The selected CFD matrix for the initial points on the GIS steep trajectory are shown in Table 3-2.

Table 3-2. GIS Steep Trajectory Cases

Trajectory Point	Time (sec)	Velocity (kft/sec)	Altitude (kft)	T_{stag} (°R)
1	1.9	56.820	139.705	2560 2660 2760
2	2.1	54.147	128.595	7060 7560 8360
3	2.4	48.042	113.205	7460 7860 8560

The stagnation-point (stagnation-line for the GIS) temperature history is shown in Figure 3-7. The GIS initial temperature at release (around 2660°R) was obtained from the SINRAP solution of the GPHS module. The temperature rapidly climbs to over 8000°R.

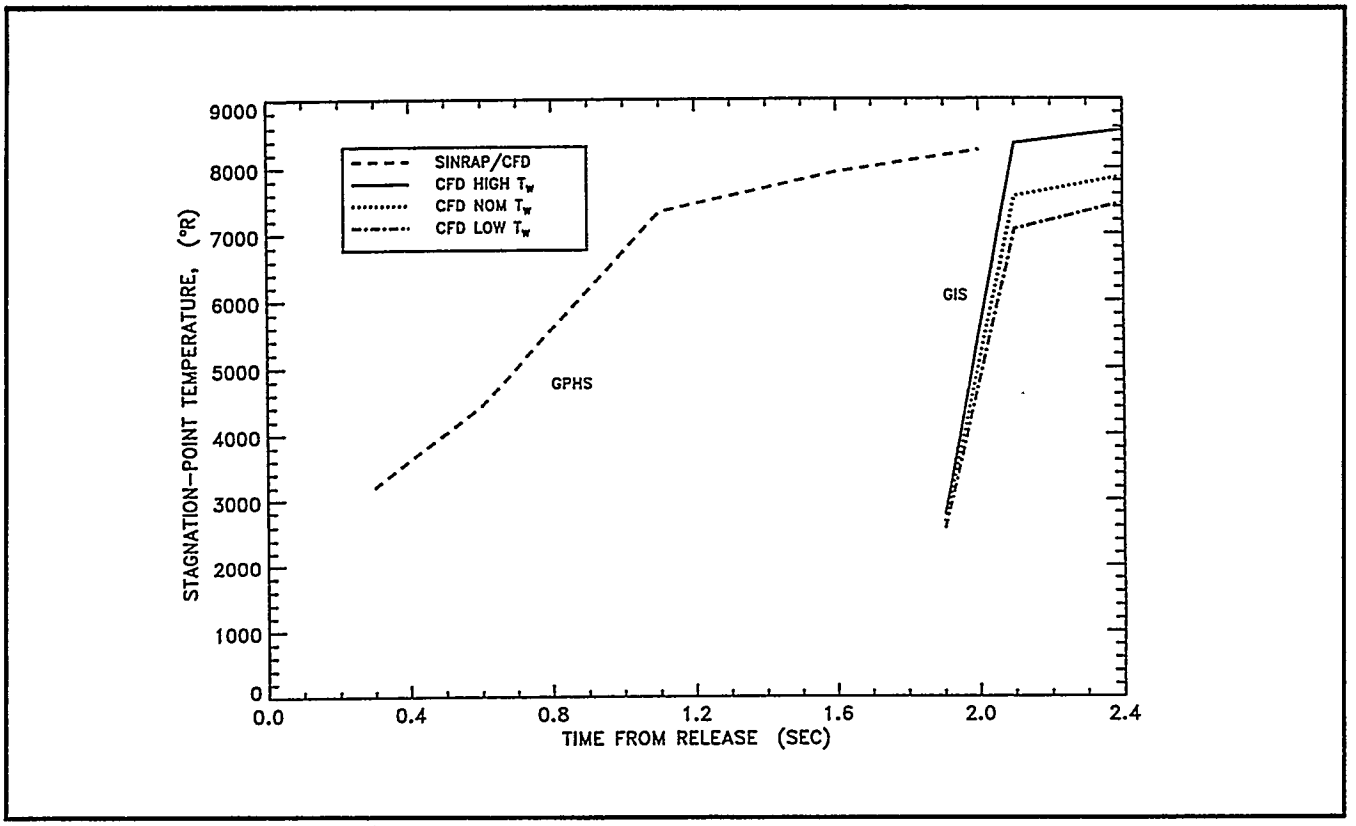

Figure 3-7. Stagnation-Point Temperature History for the GPHS Aeroshell and the GIS along the Steep Trajectory. Temperatures Selected for GIS CFD Solution Matrix

The convective component of the surface heat flux, Figure 3-8, is much greater for the GIS (compared to the flat-face aeroshell) for the 'low' and 'nominal' wall temperature cases because of the small radius of the GIS cylinder. However, for the 'high' wall temperature GIS cases shown in Figure 3-8 the convective component drops dramatically. This decrease in heating is due to high ablation rates.

At the time of GIS release (1.9 seconds) the radiative heating of the GIS, Figure 3-9, is less than the aeroshell because the shock layer for the two-dimensional cylinder is thicker than the shock layer encompassing the GPHS module. This difference is somewhat reduced by the high ablation rate of the GPHS module which provides some radiation blockage.

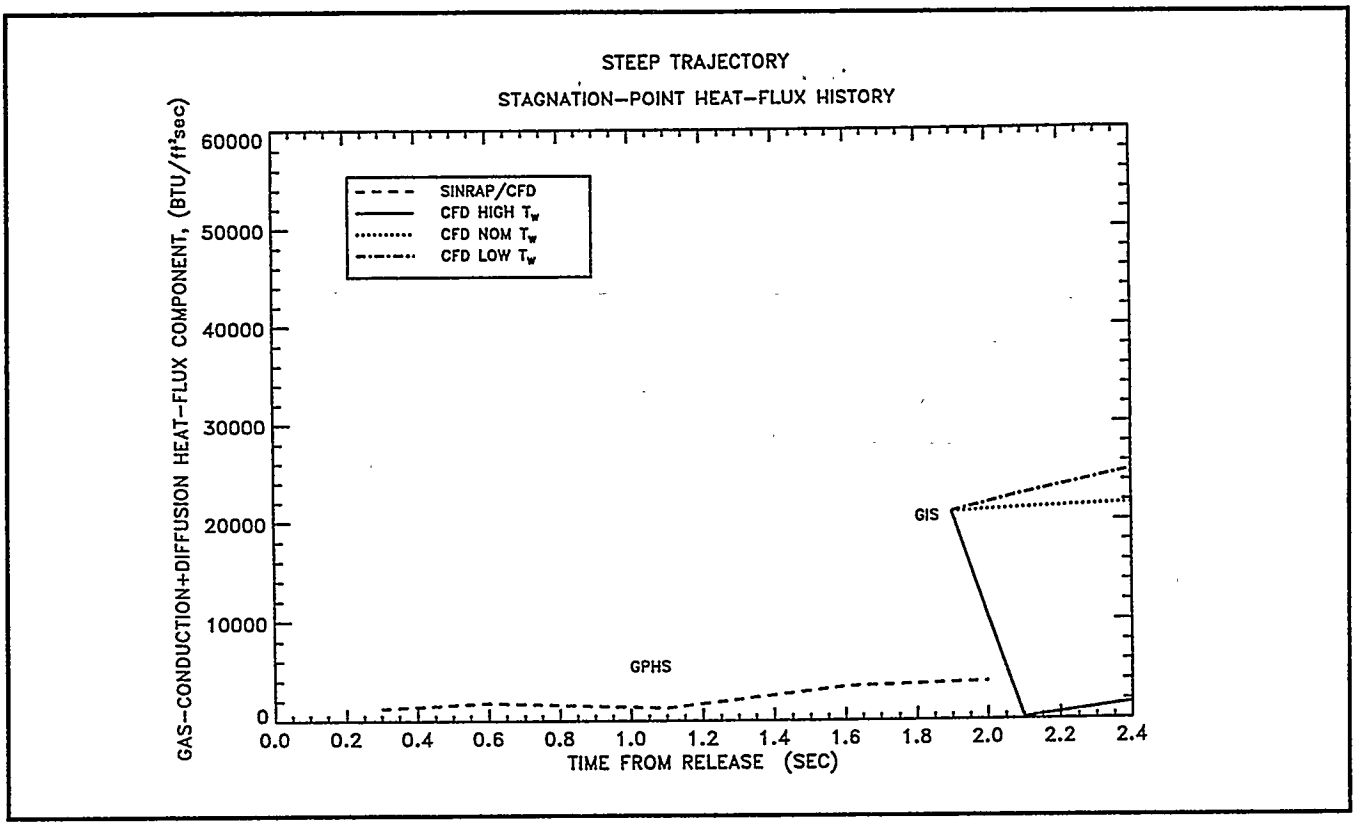

Figure 3-8. Convective Component of the Stagnation-Point Heat Flux for the GPHS Aeroshell along the Steep Trajectory. GIS CFD Solutions for SINRAP Interpolation

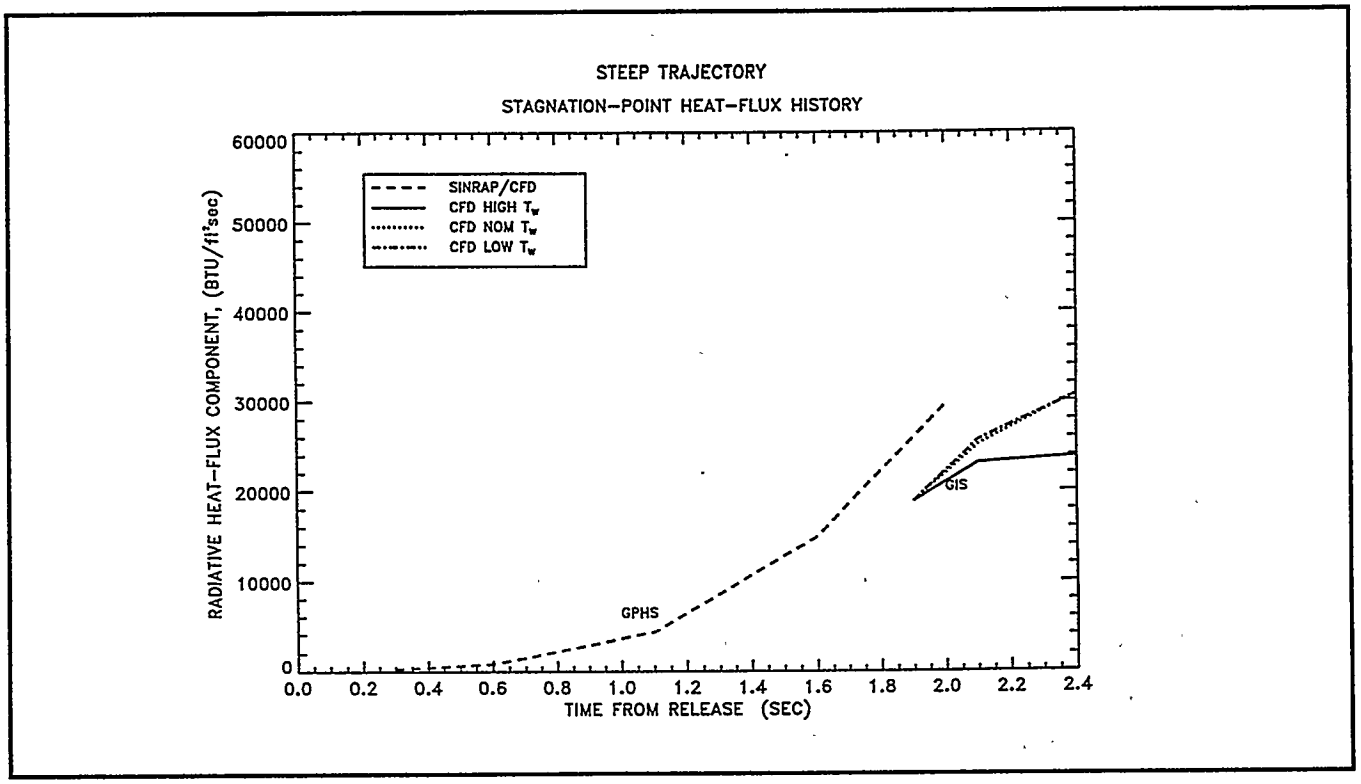

Figure 3-9. Radiative Component of the Stagnation-Point Heat Flux for the GPHS Aeroshell along the Steep Trajectory. GIS CFD Solutions for SINRAP Interpolation

The sum of the convection plus radiation components of the heat flux is shown in Figure 3-10. Initially (at 1.9 seconds), heating to the GIS is about 25% greater than that to the GPHS aeroshell. The surface ablation rates are shown in Figure 3-11. The exponential character of the ablation rate with wall temperature is revealed by the dramatic rise for the 'high' wall temperature solutions. This large ablation rate causes the drop in total heating shown in Figure 3-10.

These CFD solutions will be used for transient-heating analyses to advance the GIS to 2.4 seconds on the steep trajectory. The next set of wall temperatures and trajectory points for CFD solutions will then be selected.

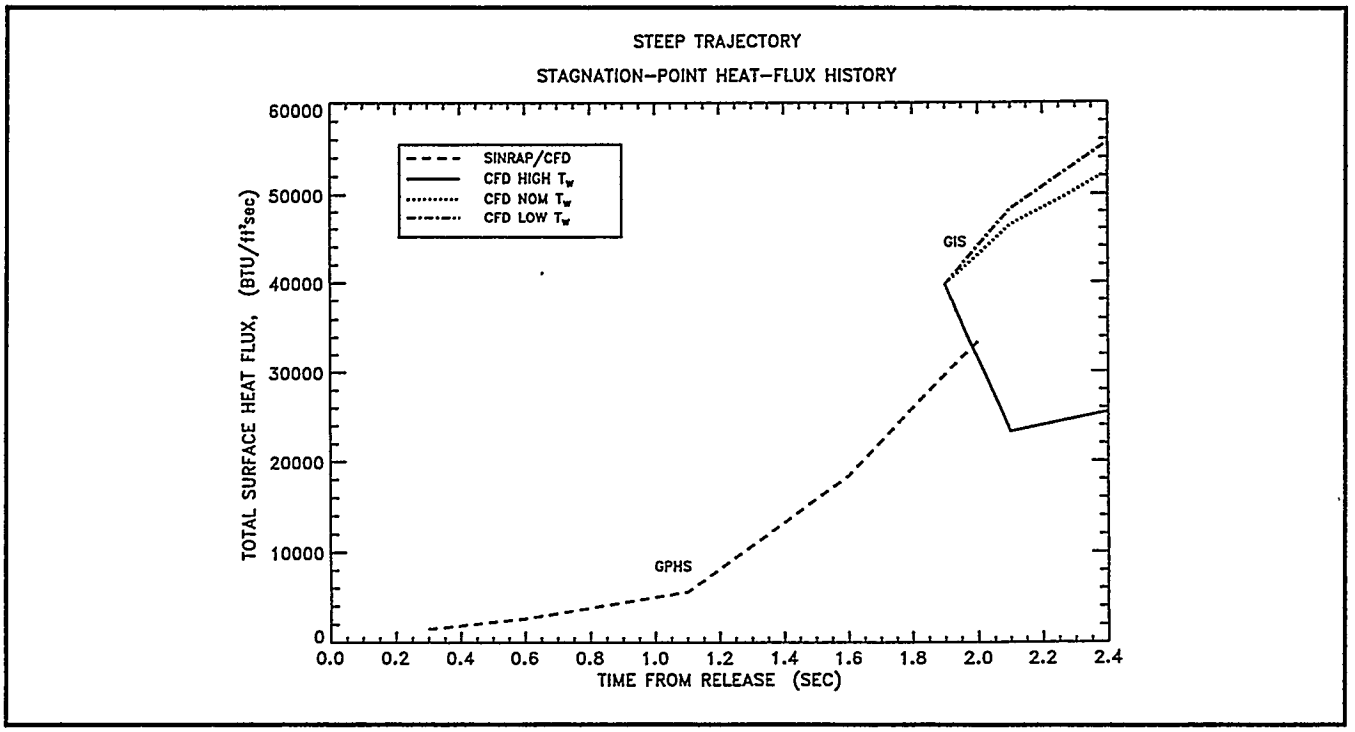

Figure 3-10. Stagnation-Point Heat Flux for the GPHS Aeroshell along the Steep Trajectory. GIS CFD Solutions for SINRAP Interpolation

Assessment of Uncertainty and Variability in the CFD Results: A systematic assessment has been performed to establish the level of confidence to be placed in the CFD predictions.

As shown in Figure 3-12, input data to the prediction techniques (RACER / LORAN-C) that are subject to uncertainty and variability have been identified. Each of these input quantities was then assessed. In addition, inputs and assumptions in the models that bias the results were also examined.

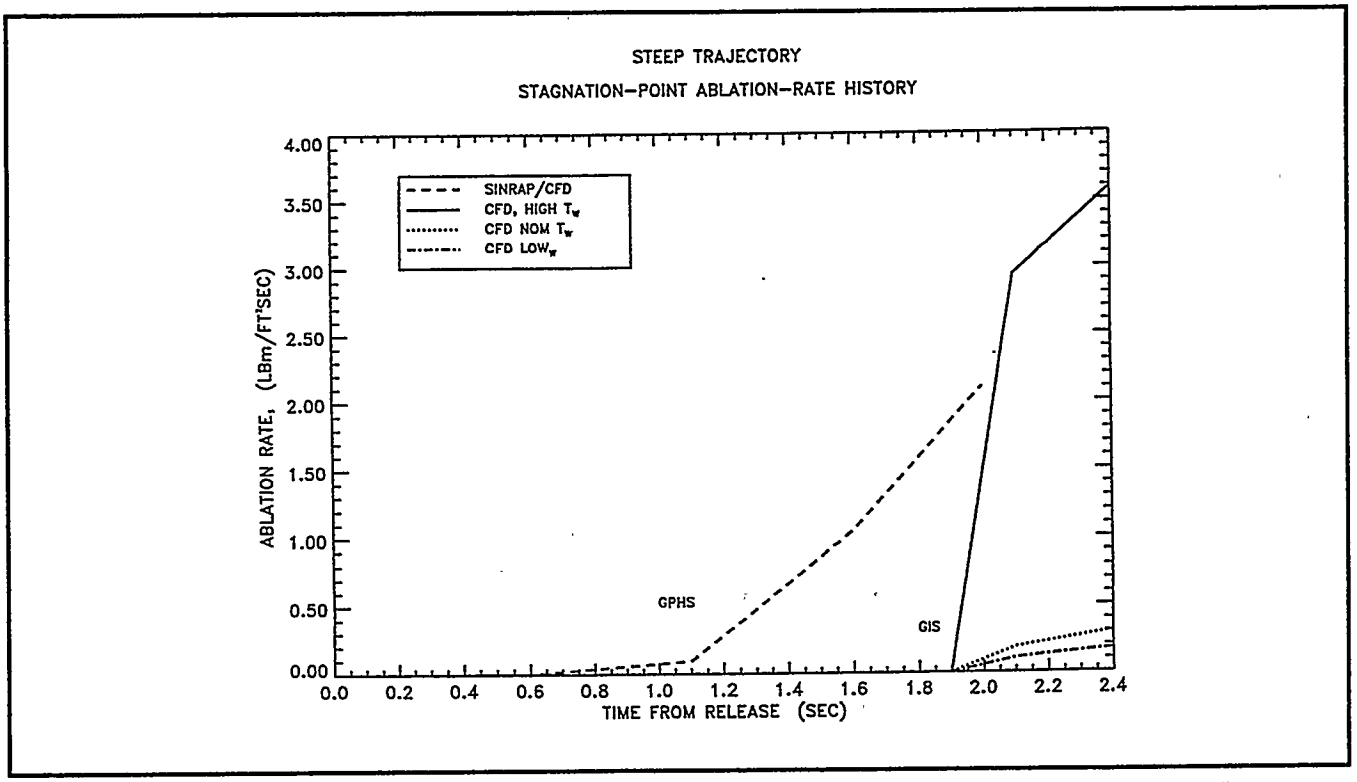

Figure 3-11. Stagnation-Point Ablation Rate for the GPHS Aeroshell along the Steep Trajectory. GIS CFD Solutions for SINRAP Interpolation

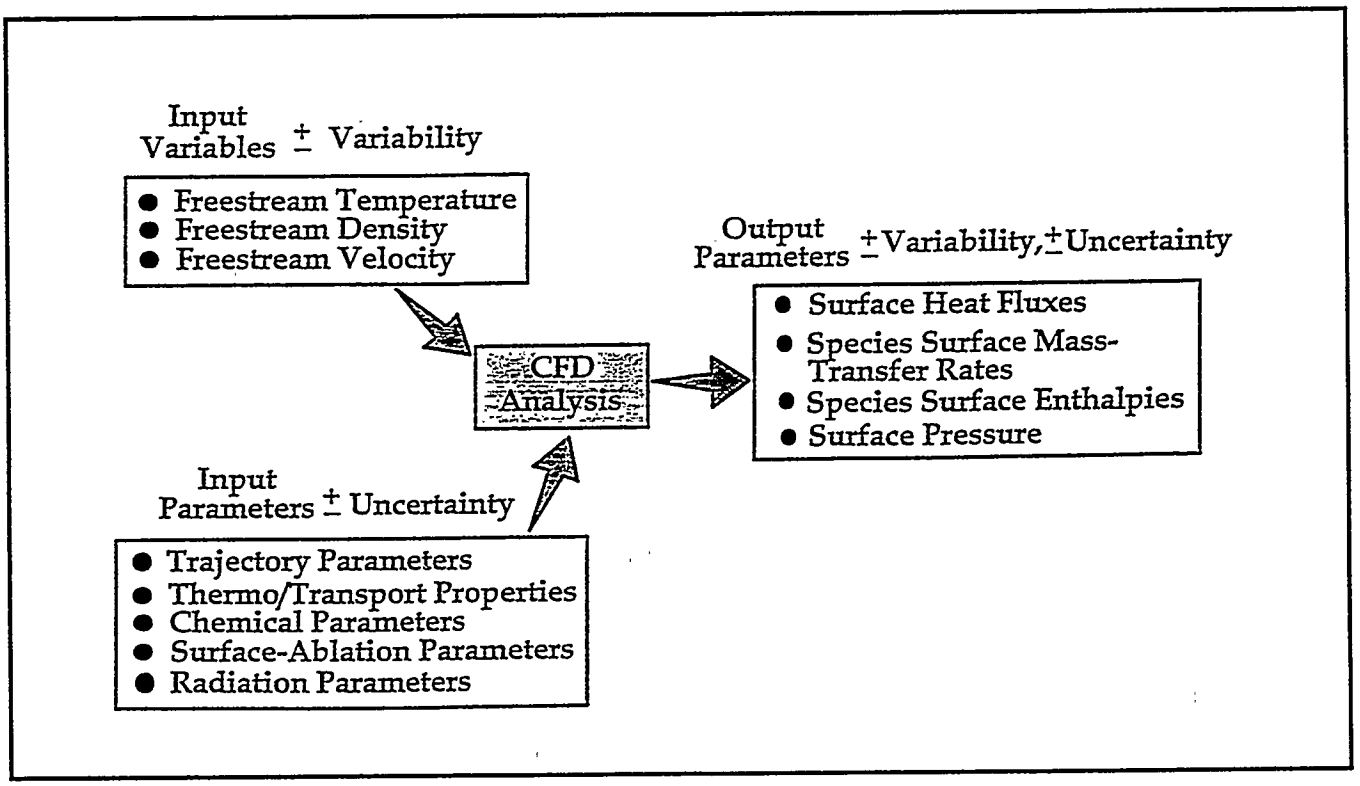

Figure 3-12. Schematic of Potential Sources of Uncertainty and Variability in the CFD Input Quantities

Uncertainty ranges on the input parameters were established and the parameters were identified as biased (causing an over-prediction or an under-prediction) or unbiased (causing ± departures from the nominal). It was also determined that the only significant input to the flowfield/radiation code subject to variability is the freestream density.

Table 3-3 lists the primary quantities that were examined after an initial screening eliminated quantities having only a secondary effect on the results. Following the approach of Rochelle, each quantity was then identified as an 'M-type' (biased) or 'U-type' (unbiased). The last column in Table 3-2 lists the estimated uncertainty or variability (as a percentage of the nominal) in predicted surface heat flux and ablation rate. The basis of these estimates, such as numerical tests and other studies, will be detailed in the Final Safety Analysis Report.

Table 3-3. Summary of Uncertainty and Variability Components in the Flowfield/Radiation Predictions

Input Parameter	Type	Uncertainty (%)
Species Convergence	U	~ 0
Choice of Sublimation Species	M	~ 0
Element Diffusion Data	M	~ 0
Thermodynamic Equilibrium Assumption	M	–5
Reaction-Rate Data and Third-Body Efficiency Matrix	U	±2
Species Enthalpy Data	U	~0
Species Viscosity, Thermal-Conductivity, and Diffusion Data	M	–5
Absorption/Emission Coefficients and Species Spectrum Data	U	± 10
Radiation Convergence	M	+5
Tangent-Slab Approximation	M	-2
Equilibrium–Catalytic Wall Assumption	M	-10
Species Vapor-Pressure Data	U	±5
Freestream Velocity/Altitude (Drag)	U	±3
Input Variable		
Freestream Density	U	±5

The combined effect of all M-type (biased) uncertainties in the net heat flux to the wall and the ablation rate is approximately -15% (where a minus sign indicates an over-prediction). A +2% margin has been added to this bias for conservatism. Based on this bias estimate, the most probable value of the net heat-transfer rate and the ablation rate is approximately 0.85 times their nominal values. The root mean-square of all U-type uncertainties around this most probable value is approximately ±15%, and the additional effect of variability is approximately ±5%.

Aeroshell Response: Thermal Analysis

Steep Trajectory: Thermal analysis for the steep trajectory, which was partially described in the last semi-annual report, has been completed. CFD results for the sixth trajectory point at 2.0 seconds have been incorporated into SINRAP, and after solving a convergence problem, a successful SINRAP run through 2.0 seconds was made. The CFD results (at the stagnation point) for the six trajectory points are summarized in Table 3-4. For the sixth trajectory point the results show a sharp increase in ablation with surface temperature, with a corresponding decrease in shock layer radiation and convection. The rapid change in radiation with surface temperature was the cause of the recent convergence problem. The solution was to average the radiation values obtained for two wall temperatures between successive iterations at a given time step. The convection and ablation, which vary even more rapidly with temperature than radiation, were averaged between successive time steps in the original version of SINRAP to achieve convergence. In that version the shock layer radiation was calculated outside of SINRAP and independent of wall temperature, so radiation averaging was not a consideration. Convergence was obtained with SINRAP, Rev. C., without radiation averaging until data from the sixth trajectory point were included.

Table 3-4. CFD Results at Stagnation Point – Steep Trajectory

Trajectory Point #	Time (Sec)	Altitude (Ft)	Surface Temperature (°F)	$Q_{RAD}\left(\frac{Btu}{Ft^2 \cdot S}\right)$	$Q_{CONV}\left(\frac{Btu}{Ft^2 \cdot S}\right)$	$\dot{m}\left(\frac{lbm}{Ft^2 \cdot S}\right)$	$\sum_{i=1}^{3} m_{ia} h_{ia}\left(\frac{Btu}{Ft^2 \cdot S}\right)$
1	0	258000	1900	94	774	.0	0
			1950	94	774	.0	0
			2000	93	774	.0	0
2	0.3	238864	3000	275	1245	.0	0
			3500	301	1252	.0	0
			4000	302	1257	.0	0
3	0.6	219764	4500	838	1739	.000016	0
			5500	806	1611	.0041	76
			6500	941	738	.0391	667
4	1.1	188149	6000	4752	3438	.0155	264
			6500	4554	2843	.0314	537
			7000	4225	715	.1384	2370
5	1.6	157306	6500	19617	8027	.0362	617
			7000	17412	5444	.0864	1490
			7150	16317	4192	.1222	2106
			7450	15070	3469	.8966	15404
6	2.0	134104	7500	36254	7046	.242	4174
			7800	32197	5441	2.340	40488
			7900	23862	696	3.914	68005

The calculated stagnation node temperature for the first six trajectory points are shown in Figure 3-13. Also shown are the imposed surface temperatures from the CFD cases of Table 3-4. The temperatures between trajectory points five and six have been added since the last report. The temperature is still increasing at 2.0 seconds, implying a net conduction from the surface into the solid.

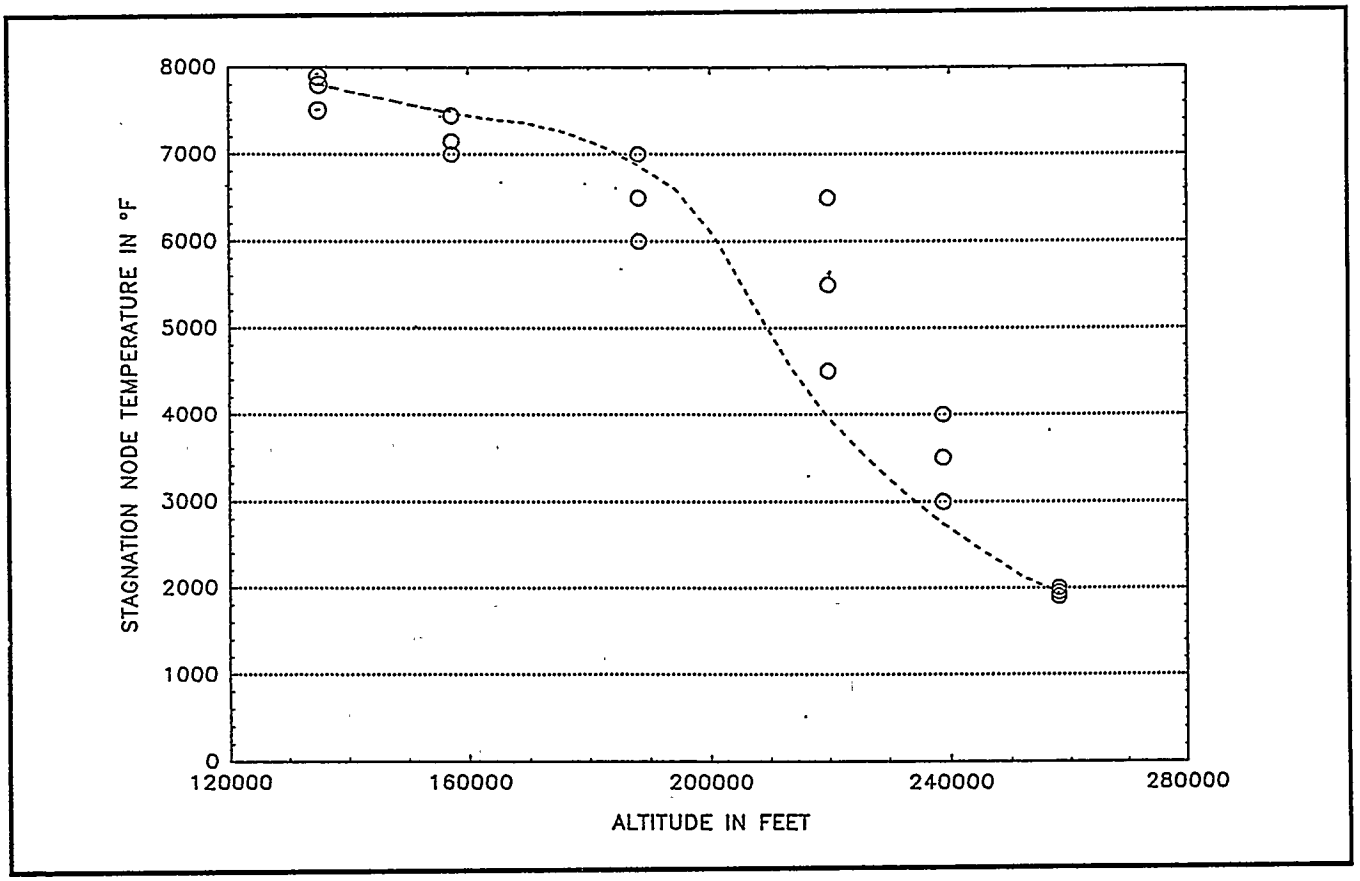

Figure 3-13. -90° Face-On Stable (CFD) Stagnation Node Temperature vs. Altitude

The front face average recession versus time is shown in Figure 3-14. The high ablation rates at the high temperatures produced 55 mils of recession between 1.6 and 2.0 seconds.

Table 3-5 shows the converged SINRAP results for the stagnation point at times and altitudes of trajectory points 2–6 (trajectory point 1 is at time zero so there is no converged solution). The value of Q_{COND} at point 6, as mentioned earlier, is consistent with the increasing temperature at this time. The recession and temperature results were made available for input to the structural analysis.

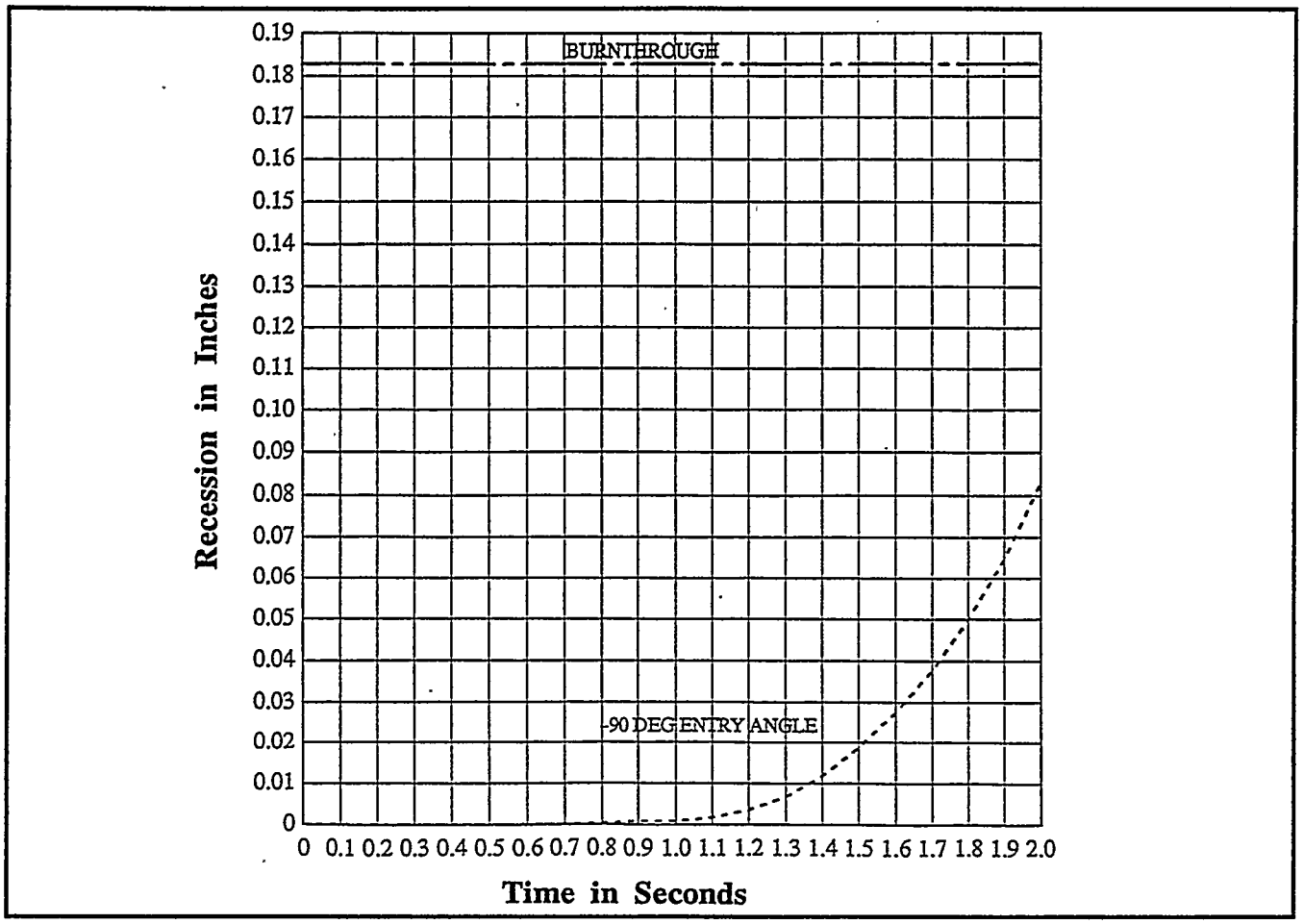

Figure 3-14. Front Face Average Recession – Face On Stable

Table 3-5. Summary of Converged SINRAP Results for Stagnation Point – Steep Trajectory

Trajectory Point #	Time (Sec)	Altitude (Ft)	Surface Temperature (°F)	$Q_{RAD}\left(\frac{Btu}{Ft^2 \cdot S}\right)$	$Q_{CONV}\left(\frac{Btu}{Ft^2 \cdot S}\right)$	$\dot{m}\left(\frac{lbm}{Ft^2 \cdot S}\right)$	$\sum_{i=1}^{3} m_{i\omega} h_{i\omega}\left(\frac{Btu}{Ft^2 \cdot S}\right)$	$Q_{COND}\left(\frac{Btu}{Ft^2 \cdot S}\right)$
2	0.3	238864	2744	264	1249	0	0	1466
3	0.6	219764	3961	850	1806	.17E-5	.0340	2485
4	1.1	188149	6871	4303	1299	.0936	1601	2984
5	1.6	157306	7472	14952	3443	1.048	17992	2159
6	2.0	134104	7798	29594	3874	2.105	36469	2363

Aeroshell Response: Thermal Analysis

Intermediate Trajectory: For the intermediate entry angle of -20°, SINRAP runs were made, without CFD input, for the face-on-stable and random tumbling orientations. Surface temperatures from these runs formed the basis for selecting imposed CFD temperatures for the first three trajectory points. Imposed temperatures for the remaining points were selected based on the SINRAP results without CFD, plus extrapolation of the results with CFD from the previous points. The CFD results at the stagnation point for the first seven trajectory points are summarized in Table 3-6. The calculated stagnation node temperature versus altitude is shown in Figure 3-15. Also shown in this figure are the imposed surface temperatures for the CFD cases and the previously calculated temperature without CFD. Since the CFD analysis started at 1.0 seconds, the calculated temperatures by both methods are the same up to this point. The switch to CFD input with the corresponding lower heat fluxes results in a temporary reduction in surface temperature. This effect is rapidly dissipated as altitude decreases. Notice that for the CFD solution the calculated surface temperature is within the imposed temperature range at each altitude. The CFD run was terminated at 7.3 seconds when one of the last ablatable nodes on the front face reached 10% of its thickness.

Table 3-6. CFD Results at Stagnation Point - Intermediate Trajectory

Trajectory Point #	Time (Sec)	Altitude (Ft)	Surface Temperature (°F)	$Q_{RAD}\left(\frac{Btu}{Ft^2 \cdot S}\right)$	$Q_{CONV}\left(\frac{Btu}{Ft^2 \cdot S}\right)$	$\dot{m}\left(\frac{lbm}{Ft^2 \cdot S}\right)$	$\sum_{i=1}^{3} m_{i\omega} h_{i\omega}\left(\frac{Btu}{Ft^2 \cdot S}\right)$
1	1.0	259257	4300	137	639	.00213	-34
			4600	146	621	.00249	-31
			4900	155	619	.00266	-26
2	2.0	237710	5000	332	1162	.00474	-46
			5600	328	1204	.00524	92
			6000	312	976	.0104	176
3	3.0	216454	5800	1133	1782	.00849	145
			6200	1106	1589	.0159	270
			6600	1194	721	.0499	851
4	4.1	193643	6500	3377	2575	.0298	510
			6800	3376	1384	.0692	1186
			7100	3199	2008	.5770	9895
5	5.2	171922	6800	7686	3355	.0549	945
			7100	6956	2521	.2136	3654
			7250	5932	2006	.6210	10644
6	6.4	150462	7000	10654	3378	.0753	1302
			7250	10214	1937	.1520	2621
			7500	9634	1779	1.259	21670
7	7.8	130197	6900	3815	3142	.0796	1366
			7100	3764	3547	.1504	2581
			7300	3682	2520	.2579	4428

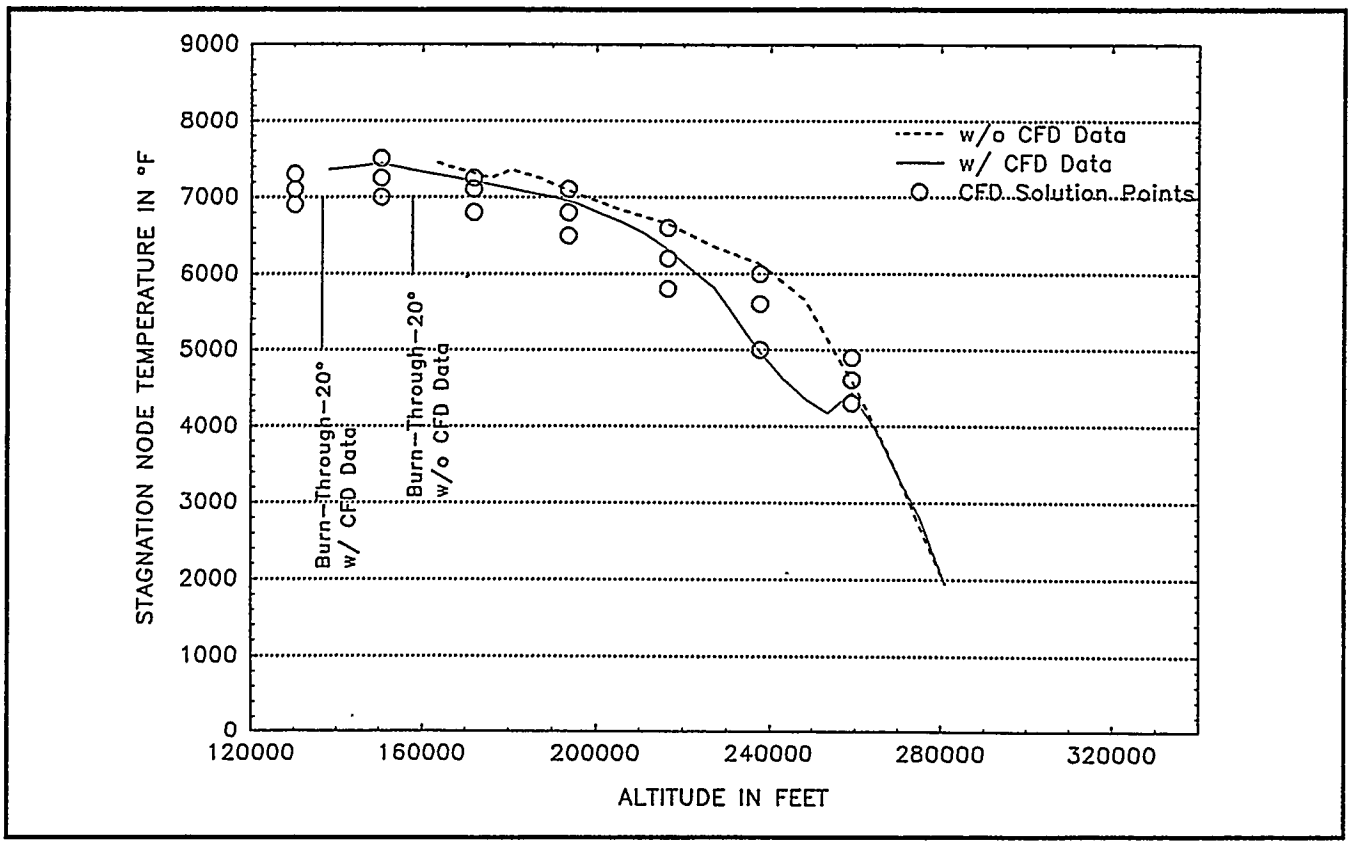

Figure 3-15. Stagnation Node Surface Temperature

The front face average recession versus time is shown in Figure 3-16. After about 4 seconds the recession increases rapidly due to the high surface temperature and correspondingly high ablation rates.

Table 3-7 shows the converged SINRAP results for the stagnation point at times and altitudes of trajectory points 1 through 6. All of the converged temperatures are within the imposed temperature range, except for the temperature at 2.0 seconds which is only slightly below the lowest imposed temperature. Trajectory point 7 does not appear since burn-through occurred prior to that time. The recession and temperature output files from SINRAP were made available for structural analysis.

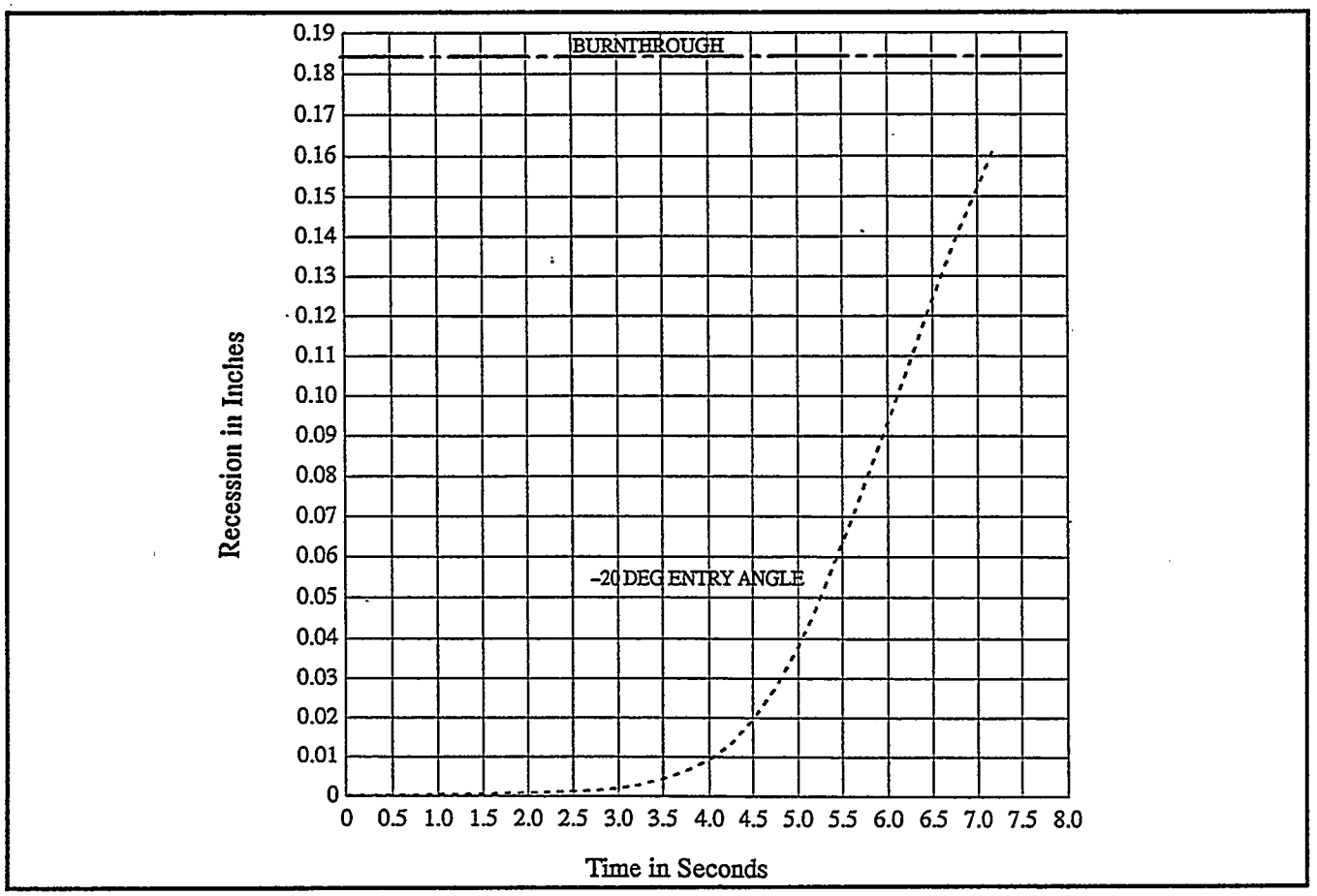

Figure 3-16. Front Face Average Recession – Face-On-Stable

Table 3-7. Summary of Converged SINRAP Results for Stagnation Point – Intermediate Trajectory

Trajectory Point #	Time (Sec)	Altitude (Ft)	Surface Temperature (°F)	$Q_{RAD}\left(\frac{Btu}{Ft^2 \cdot S}\right)$	$Q_{CONV}\left(\frac{Btu}{Ft^2 \cdot S}\right)$	$\dot{m}\left(\frac{lbm}{Ft^2 \cdot S}\right)$	$\sum_{i=1}^{3} m_{i\omega} h_{i\omega}\left(\frac{Btu}{Ft^2 \cdot S}\right)$
1	1.0	259257	4444	138	635	.00234	0
2	2.0	237710	4963	336	1162	.00478	0
3	3.0	216454	6318	1119	1399	.0214	363
4	4.1	193643	6945	3298	1574	.1969	3374
5	5.2	171922	7208	6264	2247	.4648	7962
6	6.4	150462	7437	9763	1779	.6858	11807

GIS Response Thermal Analysis Approach

Failure of an aeroshell during reentry can result in release of one or both GIS assemblies at altitude. There is also the possibility that one or both GIS assemblies will remain in the aeroshell until impact with the Earth's surface. A GIS released from a failed aeroshell can assume a number of possible orientations including tumbling, side-on spinning, side-on stable or end-on-stable, as illustrated in Figure 3-17.

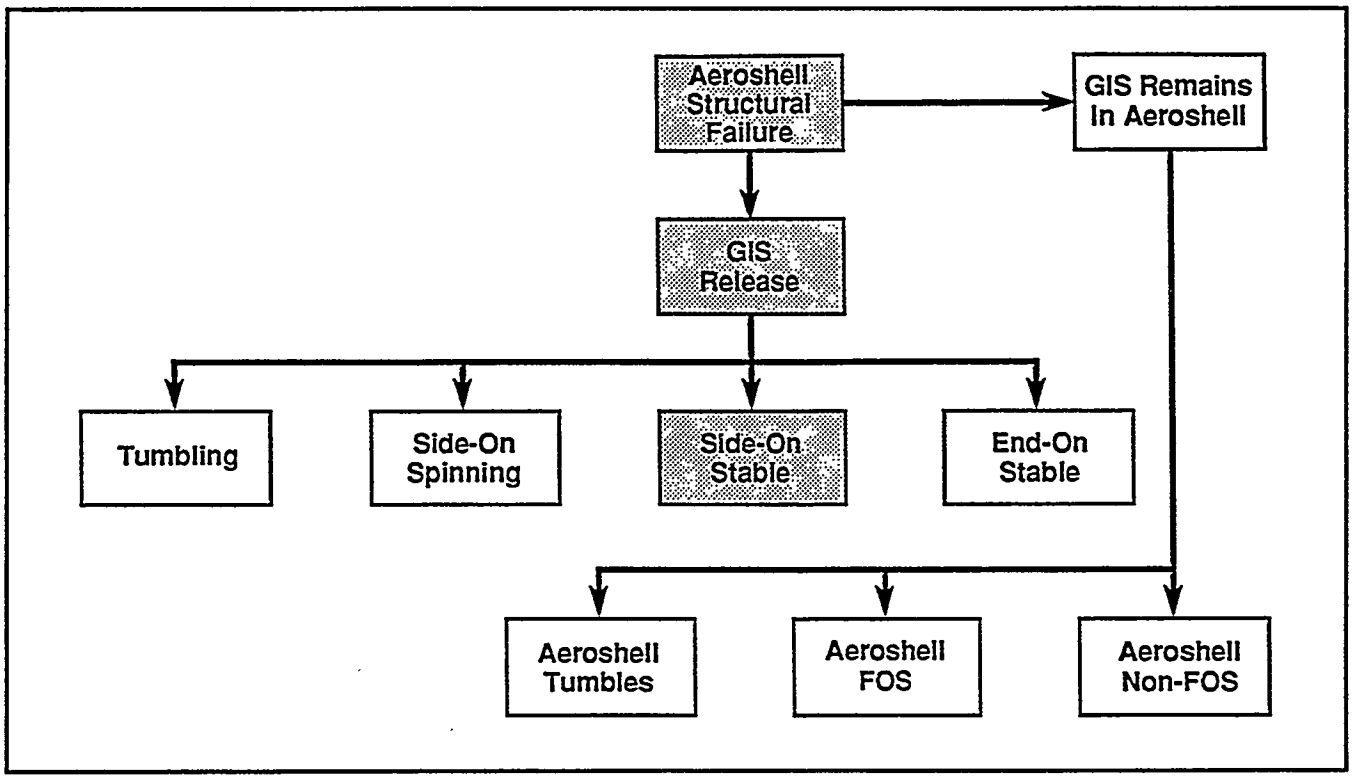

Figure 3-17. Event Diagram for GIS Release

Analysis of GIS assembly thermal and structural response following release from a failed aeroshell has been performed for a side-on stable condition. In this orientation, a GIS is exposed to the most severe thermal environment of any other than end-on stable. (GIS assemblies which maintain an end-on stable condition following release from a failed aeroshell would be expected to experience burn-through at the forward blind crush holes.) As shown by aeroshell analyses, a surface in a tumbling or spinning mode will maintain lower temperatures and so experience less ablation than the corresponding surface in the face-on stable orientation. Therefore, the side-on stable condition provides a worst case orientation for assessing GIS survivability.

The approach for GIS reentry analysis for the side-on stable orientation is shown in Figure 3-18. GIS trajectory information is obtained from the trajectory simulation code, 3DMP, based on the cylindrical GIS geometry, with initial conditions based on aeroshell trajectory values at the time of aeroshell failure. The GIS was assumed to be released at the time of aeroshell failure predicted for the -90° steep and -20° intermediate trajectories.

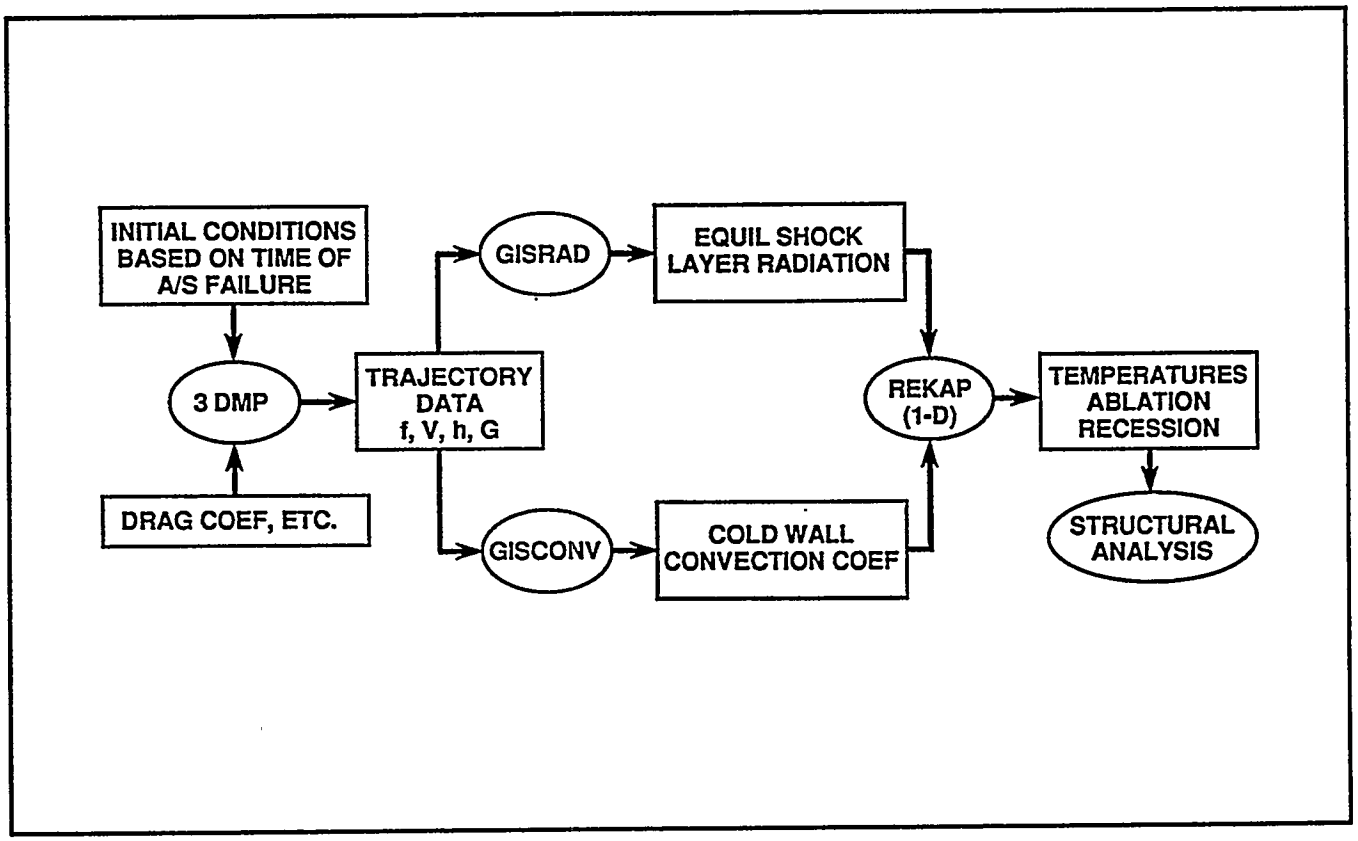

Figure 3-18. GIS Reentry Analysis Flow Chart for Side-on Stable Orientation

For continuity with aeroshell response predictions, the off-line radiation and convection codes used for aeroshell analysis prior to CFD were also employed for GIS thermal analysis, modified to account for the shape of the GIS. The shock layer radiation code, GISRAD, was also employed for GIS thermal analysis, modified based on correlated relationships which give shock detachment distance, Δ/R, for a sphere and cylinder. Since the radiation is calculated based on spherical data, the correlated relationships were used to determine the spherical radius which yielded the same detachment distance as the GIS cylinder. The cold wall convection code, GISCONV, employs convection relationships based on a 12" radius sphere. The relationships were corrected to a sphere having the same radius as the GIS (0.775 inches). Then the convection coefficient was multiplied by 0.69 to correct from a sphere to a cylinder of the same radius. The shock layer radiation

and cold wall convection coefficients were determined at selected times along the GIS trajectory and input into REKAP, the same model as utilized for the aeroshell thermal analysis for out-of-orbit reentry.

REKAP solves the multi-layer heat conduction problem using the previously described heating distributions and accounts for material properties as a function of temperature. Energy is re-radiated from the surface using the appropriate temperature-dependent hemispherical emittance. REKAP uses β' curves to obtain ablation rates as a function of surface temperature and pressure. The effect of ablation on radiation and convection is included in REKAP. The resultant GIS surface temperature, gradients through the thickness, and recession as a function of time were used in the GIS structural analysis.

The thermal model used for the GIS assembly in the side-on stable orientation is shown in Figure 3-19. The REKAP model uses cylindrical coordinates so that the internal conduction model is one-dimensional in the radial direction. In this manner, the GIS, clad and fuel nodes will have the correct proportional mass for the transient analysis. The GIS has five nodes through the thickness to model internal conduction and to provide gradients for the structural analysis. This approach will over-predict the stagnation region temperature as there will be some heat conducted in the circumferential direction to the cooler regions away from the stagnation point.

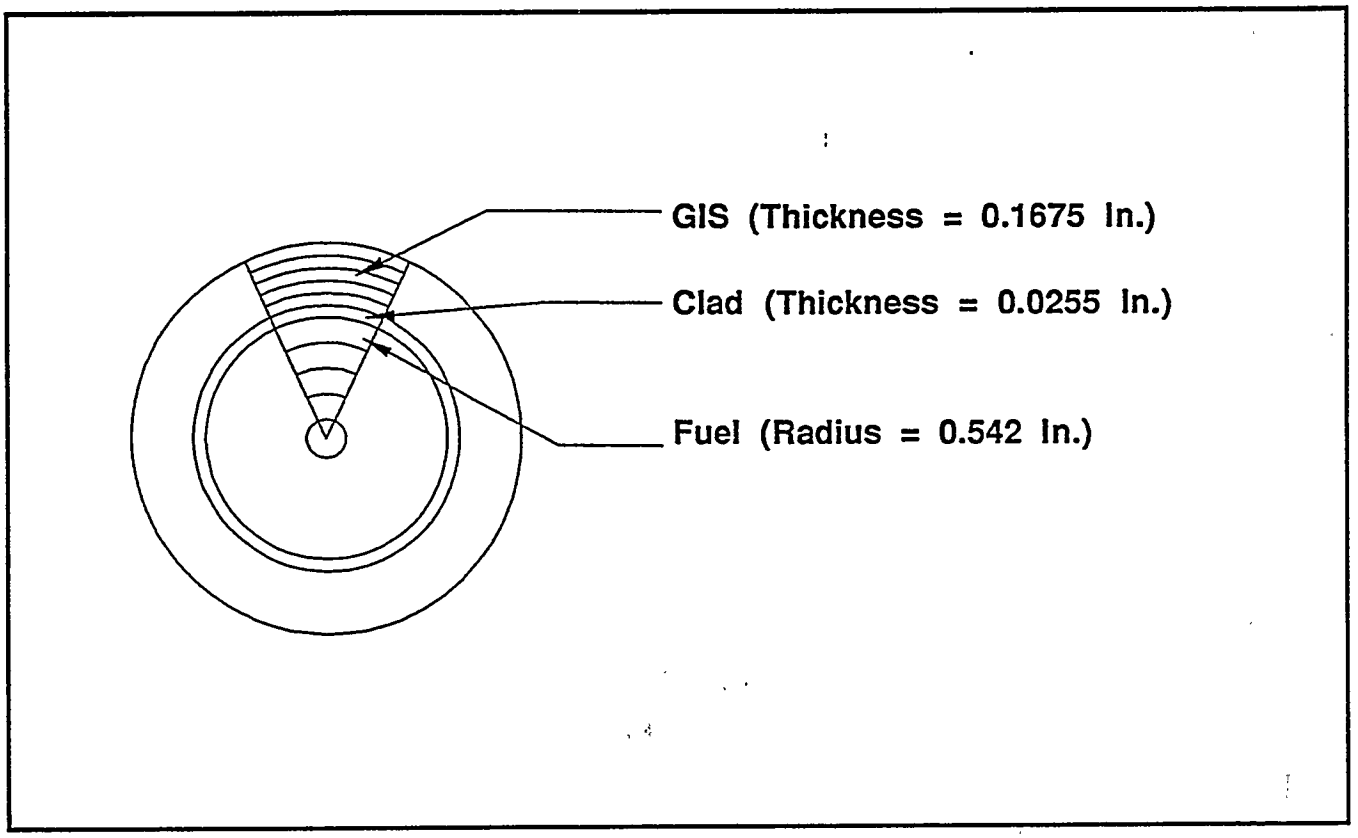

Figure 3-19. GIS Thermal Model

GIS Thermal Analysis Results

Thermal analyses have been completed for the GIS in the non spinning, side-on stable orientation for the steep (-90°) and intermediate (-20°) trajectories.

The initial conditions for these two cases are based on the SINRAP aeroshell run and the predicted time of GIS release from the aeroshell determined by the structural analysis. The key parameters at the time of GIS release are as follows:

Parameter	Initial Conditions	
Initial Aeroshell Reentry Angle	-90°	-20°
Time of GIS Release (sec)	1.9	5.85
Altitude (ft)	139,705	159,925
Velocity (ft/sec)	56,820	55,192
Path Angle (deg)	-88.624	-18.854
Component Nodal Temperatures (°R)		
GIS	2649	2752
Iridium Clad	2834	2834
Fuel	3022-3327	3022 - 3327

For both cases the time between the original aeroshell release and subsequent GIS release is short enough that the GIS temperature in the steep case is unchanged and is just starting to increase in the intermediate case. The clad and fuel temperature is unchanged.

Steep Trajectory: Shock layer radiation for the GIS steep trajectory peaks at 2.4 seconds with the major portion of the heat pulse over by 4.0 seconds. In Figure 3-20, the surface temperature history is shown for the first 10 seconds. The GIS, when assumed released from an aeroshell 1.9 seconds into the steep reentry (at 139.7 kft), is subjected to near peak heating conditions and, therefore, the surface temperature rises extremely fast. The temperature also starts to decrease at a few tenths of a second following the time of peak heating. The GIS surface temperature, from time of release to Earth impact at 172.6 seconds, is shown in Figure 3-21. In about 10 seconds, the GIS temperature has risen rapidly and then cooled down to release temperature and from there, continues to cool until impact with the Earth's surface.

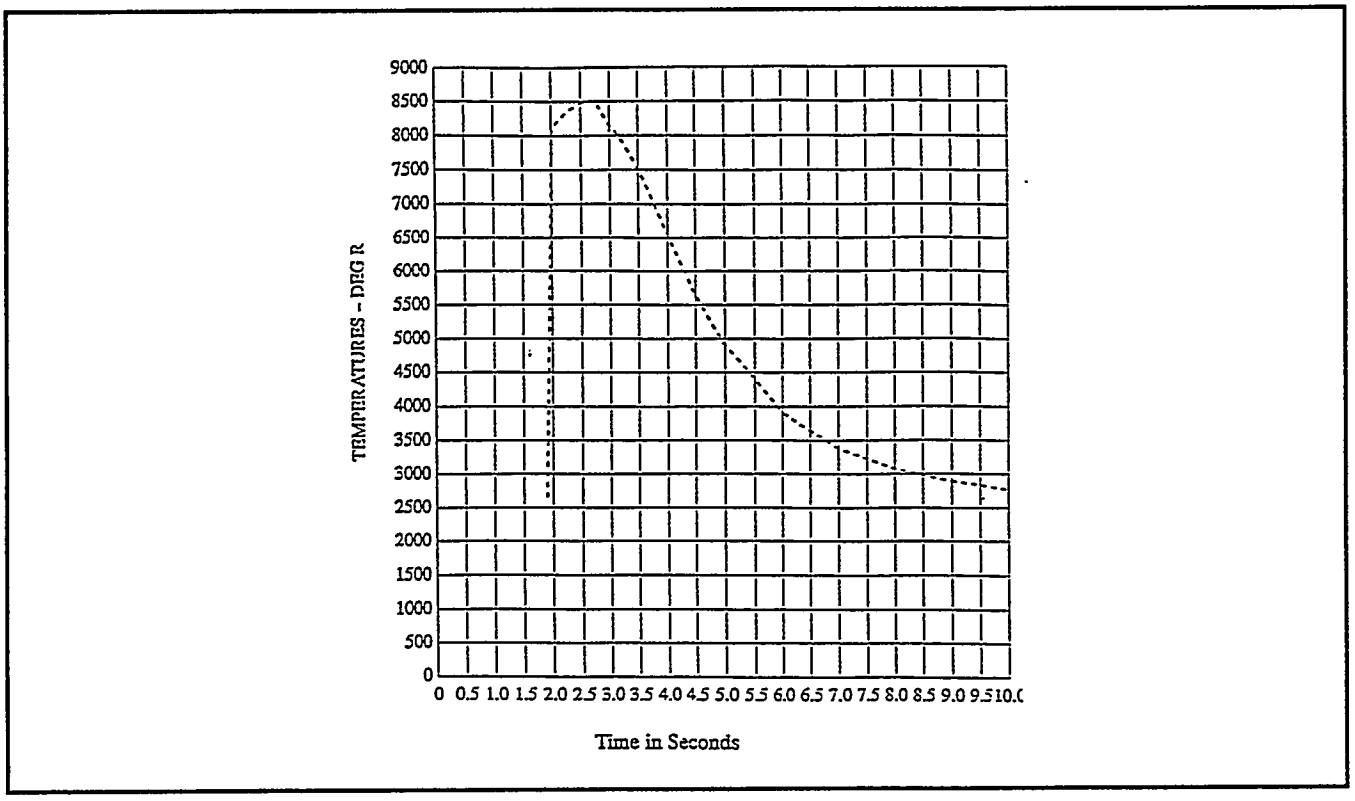

Figure 3-20. GIS Surface Temperature at Stagnation Point for Steep Trajectory Release at 139.7 kft (Initial 10 Seconds)

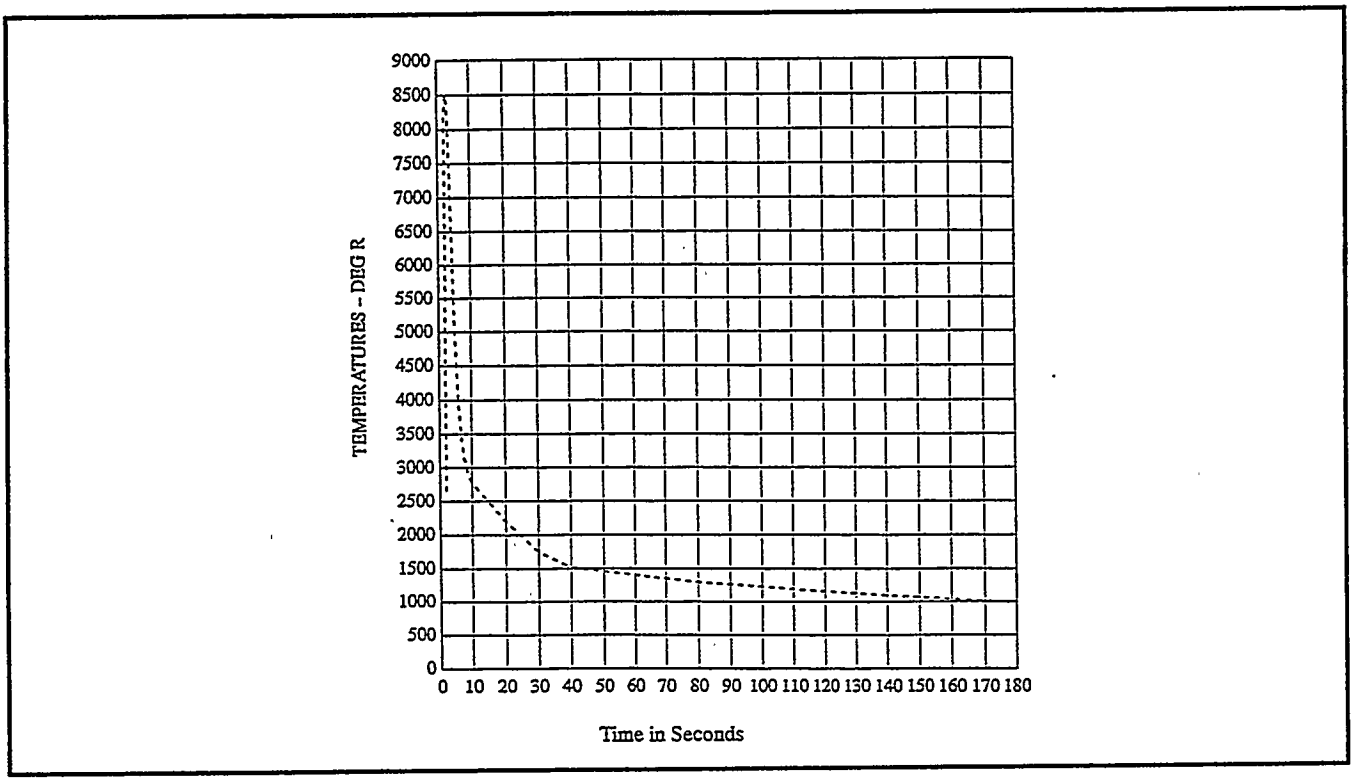

Figure 3-21. GIS Surface Temperature at Stagnation Point for Steep Trajectory Release at 139.7 kft (To Impact at 172.6 Seconds)

The GIS recession versus time is shown in Figures 3-22 and 3-23. Most of the recession takes place during the heat pulse, with the recession reaching 0.136 inches at 4.0 seconds. Ablation, however, is a function of surface temperature and continues until 30 seconds when the recession is 0.152 inches.

The iridium clad temperature and fuel temperature at the node nearest the clad are shown in Figure 3-24. Temperatures shown in Figure 3-24 were calculated without adjusting for heat absorbed during the iridium melting. This effect would tend to produce slightly lower temperatures than those shown here. The clad temperature rises above the iridium melt temperature. It then cools down rapidly, falling well below the melt temperature. The fuel node temperature, due to fuel mass and shortness of the heat pulse, stops well below the melt temperature. There would be, however, melting of a thin fuel layer which is in contact with the melted clad.

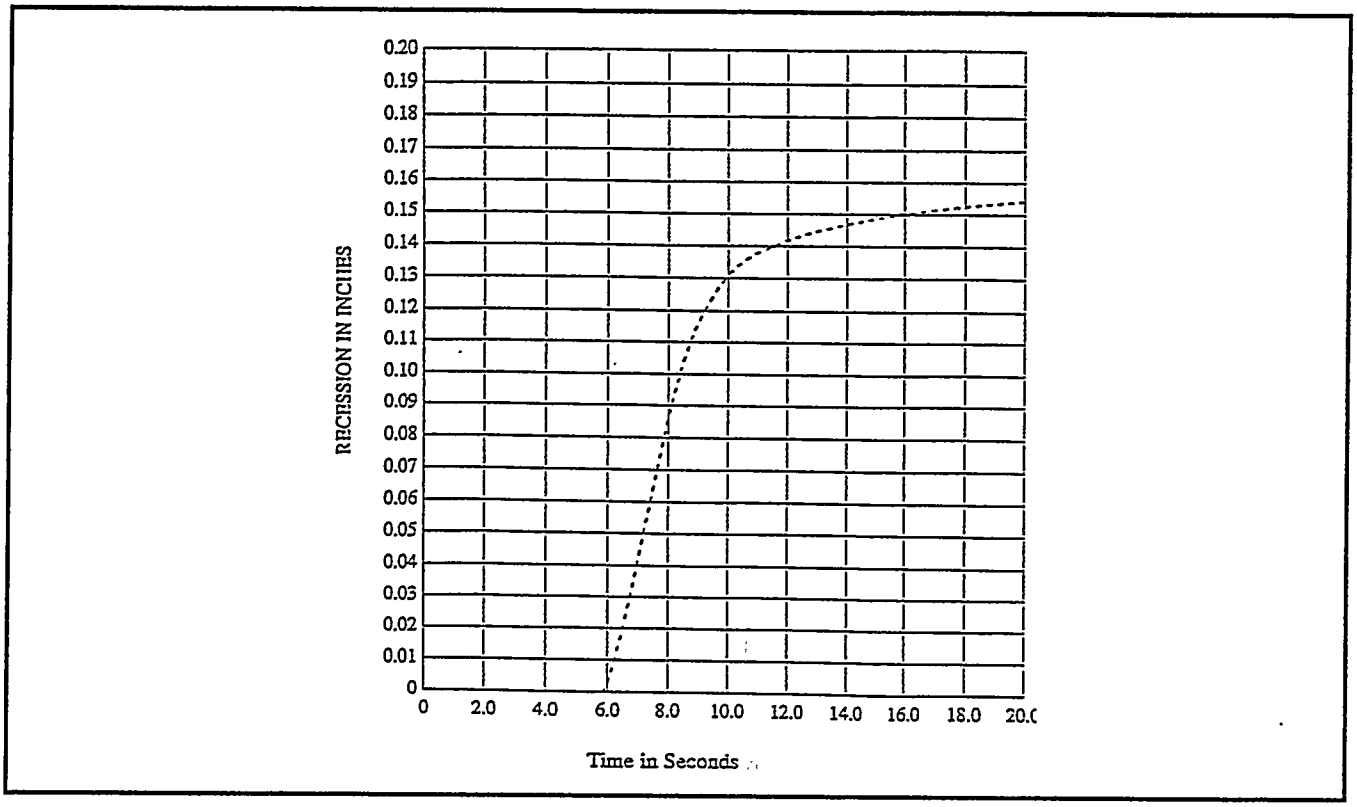

Figure 3-22. GIS Recession at Stagnation Point for Steep Trajectory Release 139.7 kft (Initial 10 Seconds)

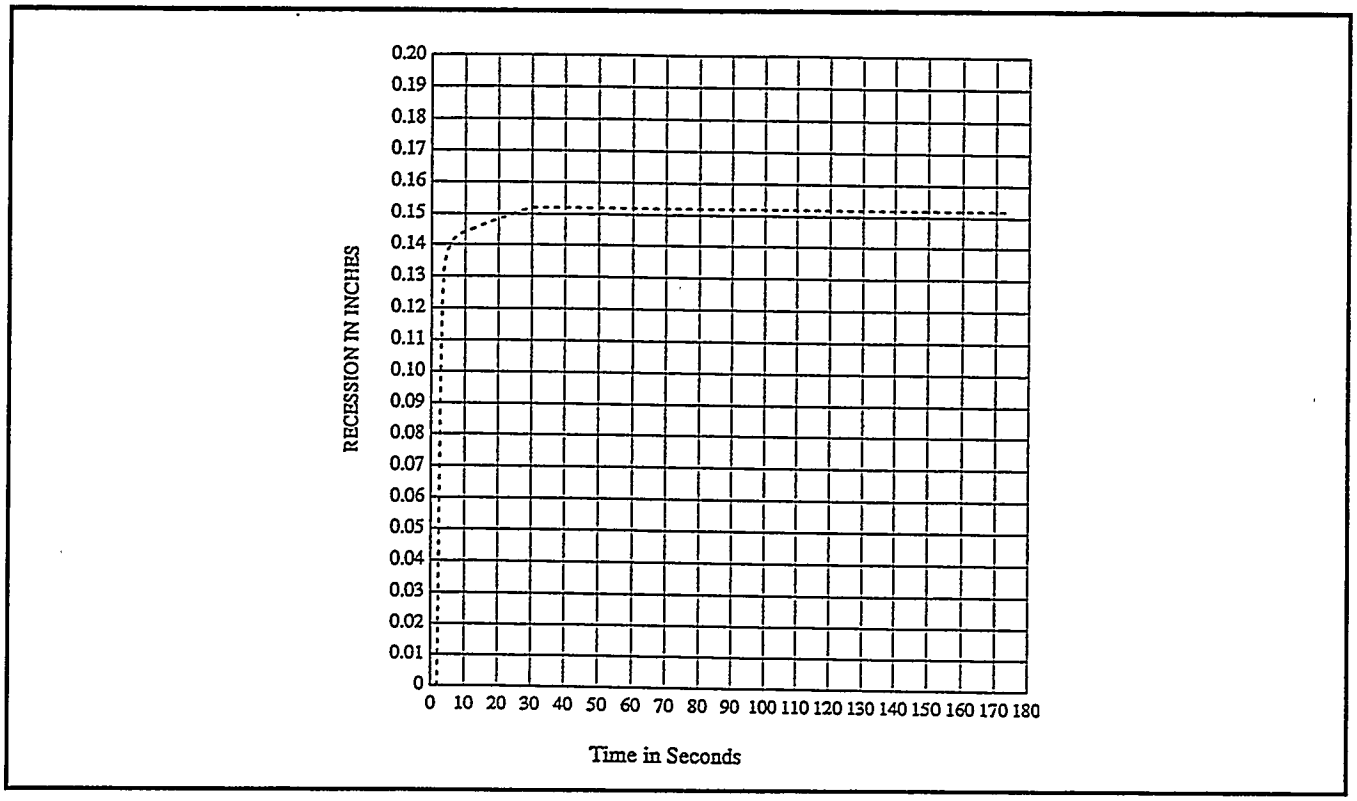

Figure 3-23. GIS Recession at Stagnation Point for Steep Trajectory Release at 139.7 kft (Earth to Impact)

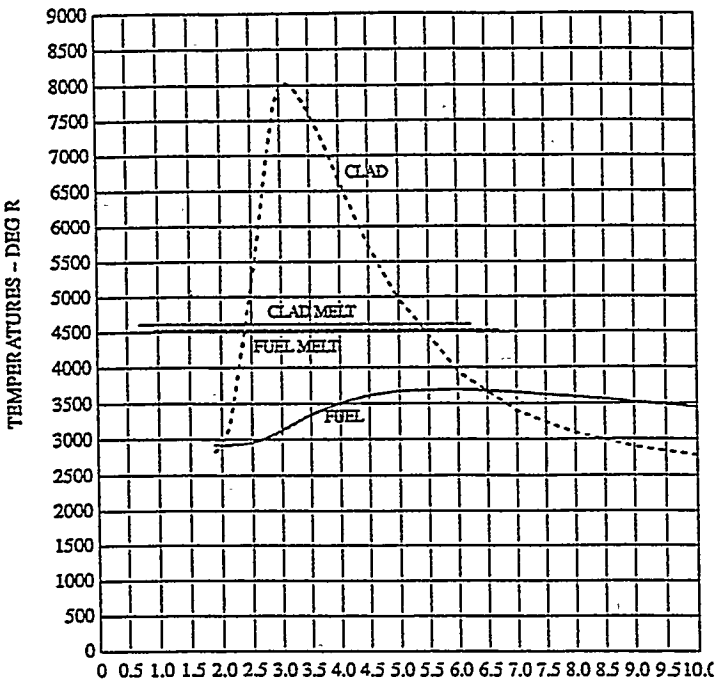

Figure 3-24. Clad and Fuel Temperatures for GIS Release at 139.7 kft, 1.9 Seconds into a Steep Trajectory Reentry

Intermediate Trajectory: For the intermediate trajectory, shock layer radiation peaks at 6.6 seconds with the major portion of the heat pulse over by 11 seconds. The GIS surface temperature during the heat pulse and just beyond is shown in Figure 3-25. As was the case for the steep trajectory, the GIS upon release is subjected to near peak heating conditions and experiences an extremely fast rise in temperature. The peak temperature reaches 7882°R compared to 8500°R reached for the steep case. The GIS surface temperature, from time of release throughout most of the trajectory, is shown in Figure 3-26 (Earth impact time would occur at 234 seconds). The GIS recession versus time is shown in Figures 3-27 and 3-28. Approximately 85% of the recession takes place during the heat pulse. Ablation continues until about 50 seconds when the recession has reached 0.164 inches.

As was the case for the steep case the clad will melt during the heat pulse, followed by a rapid cool-down below the melt temperature. The fuel will not melt except for a thin layer in contact with the clad.

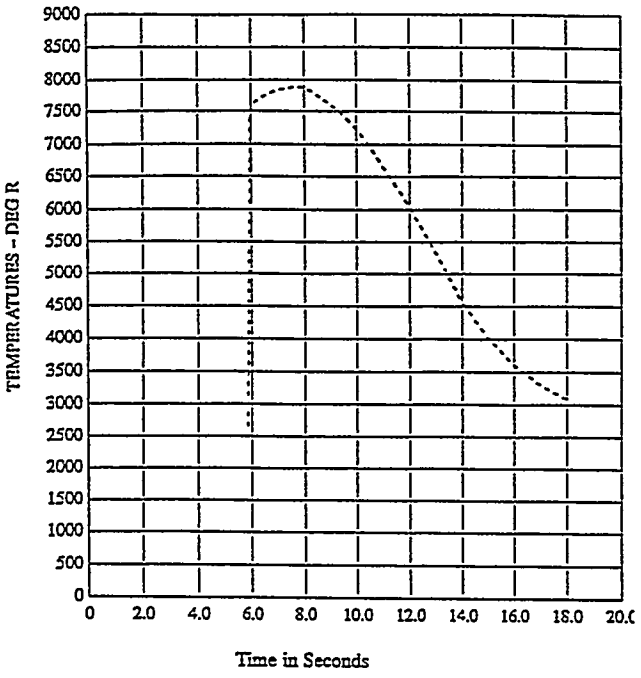

Figure 3-25. GIS Surface Temperature at Stagnation Point for Intermediate Trajectory Release at 159.9 kft (Initial 20 Seconds)

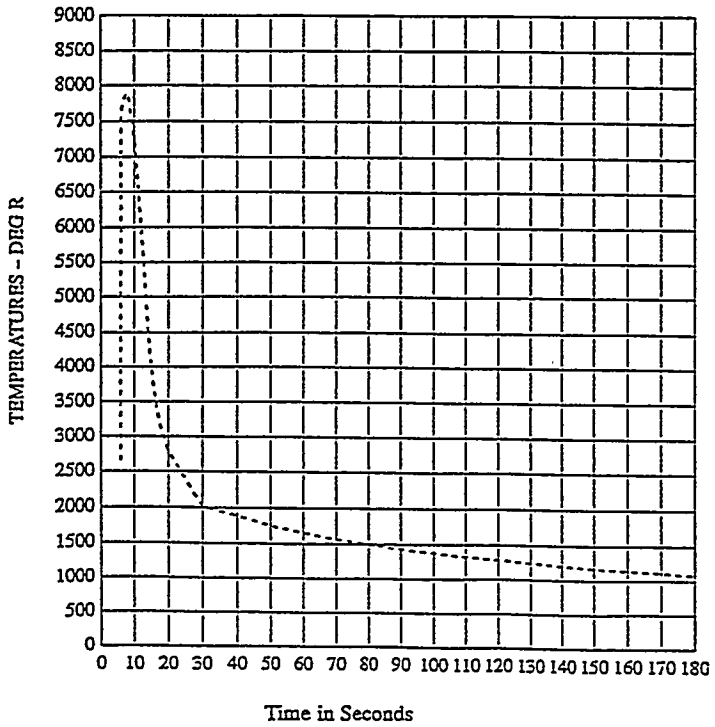

Figure 3-26. GIS Surface Temperature at Stagnation Point for Intermediate Trajectory Release at 159.9 kft

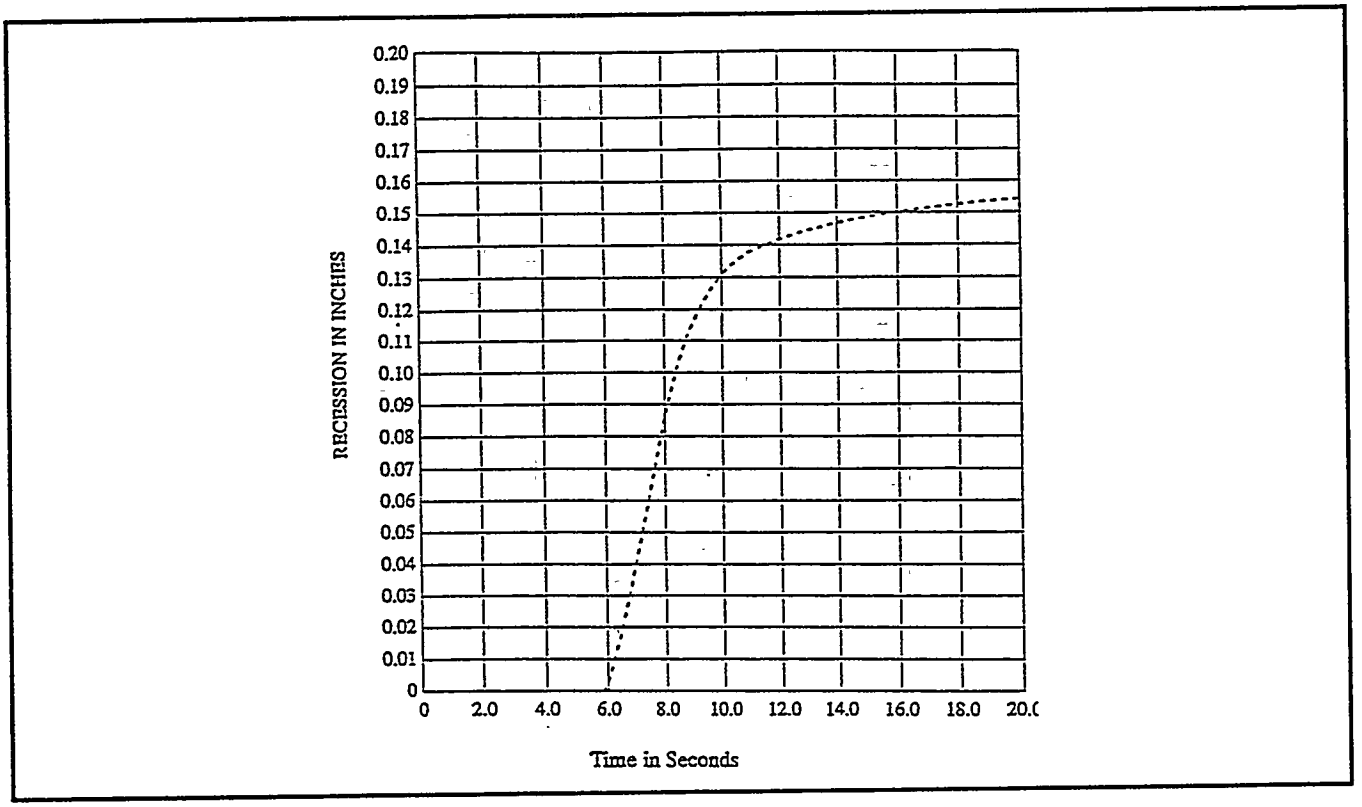

Figure 3-27. GIS Recession at Stagnation Point for Intermediate Trajectory Release at 159.9 kft (Initial 10 Seconds)

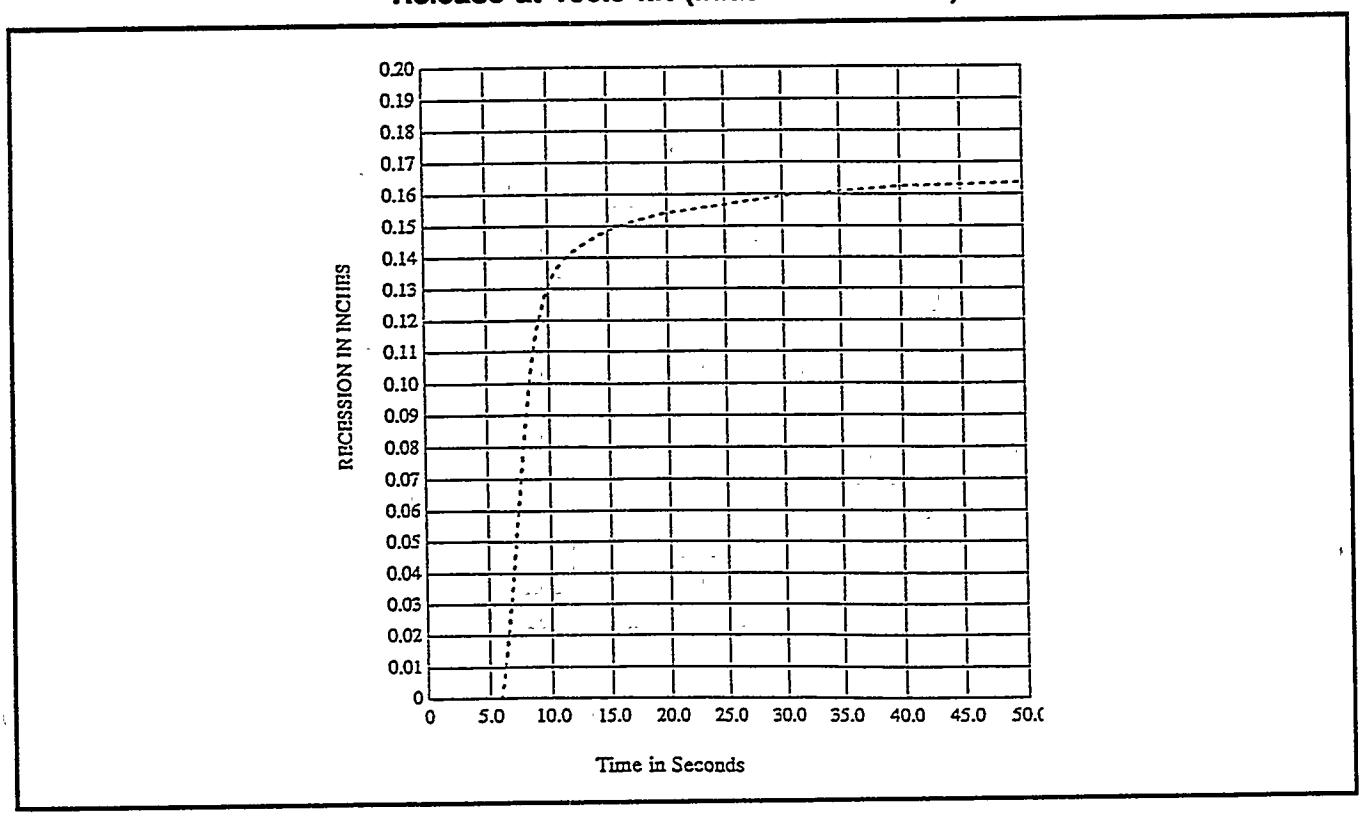

Figure 3-28. GIS Recession at Stagnation Point for Intermediate Trajectory Release at 159.9 kft

Future plans for GIS reentry analysis are to use the results from the steep and intermediate runs to select imposed temperature for the CFD cases. The GIS CFD solutions will be input into REKAP/CFD to obtain new temperature and recession results.

SINRAP Modification and Documentation: The codes used to incorporate CFD results into SINRAP have been documented and verified. Documentation of SINRAP, Rev. C is contained in Reference 1. The primary purpose of Rev. C is to include the changes required to incorporate CFD results. Also included are the changes made to make the innermost node ablatable and to incorporate the new CBCF air conductivity model developed by ORNL. Verification of the Rev. C changes is documented in Reference 2.

The CONVERT and CORRECT programs, which post-process CFD output results into tables for SINRAP input, are documented in Reference 3. The CONVERT program converts the CFD data at different radial locations into SINRAP model data. It also organizes the data into sets of three altitudes (e.g., ALT1–ALT3, and ALT3–ALT5) with three front face temperatures for each altitude for interpolation within SINRAP. CONVERT was set up so that for each of the three altitudes in a given set, the ratio of $\Delta_{T3-T2}/\Delta_{T2-T1}$ would be the same. The difficulty in obtaining CFD data at the higher surface temperatures led to results in which the CFD surface temperature did not fit the prescribed pattern. Rather than running a fourth surface temperature, program CORRECT was written to interpolate the middle CFD output data to a different temperature for input into CONVERT. For example, CFD output for the sixth trajectory point of the steep case was obtained at 7500°F, 7800°F and 7900°F. The CORRECT program was used to interpolate the output as a function of temperature to obtain CFD data at 7700°F.

EGA Reentry Structural Analysis

Steep Trajectory (-90°): Thermostructural analysis was completed for the steep (90 degree) reentry condition with a face-on-stable attitude. The SINRAP transient thermal analysis had progressed through t = 2.0 seconds, which corresponds to an altitude of approximately 134 kft. Data from this analysis was reviewed and cross-plotted with deceleration loads resulting from the 3 DOF runs (see Figure 3-29). Four timepoints were analyzed along this trajectory, including the point representing the maximum stagnation point thermal gradient (t = 1.1 seconds). The remaining three analysis points represented intermediate times in the trajectory up to and including the point at which structural failure of the aeroshell was predicted. Load conditions at the various timepoints are summarized in Table 3-8. Since temperatures approaching 8000°K were predicted, the ABAQUS material model was extended to these temperature limits using estimated material properties.

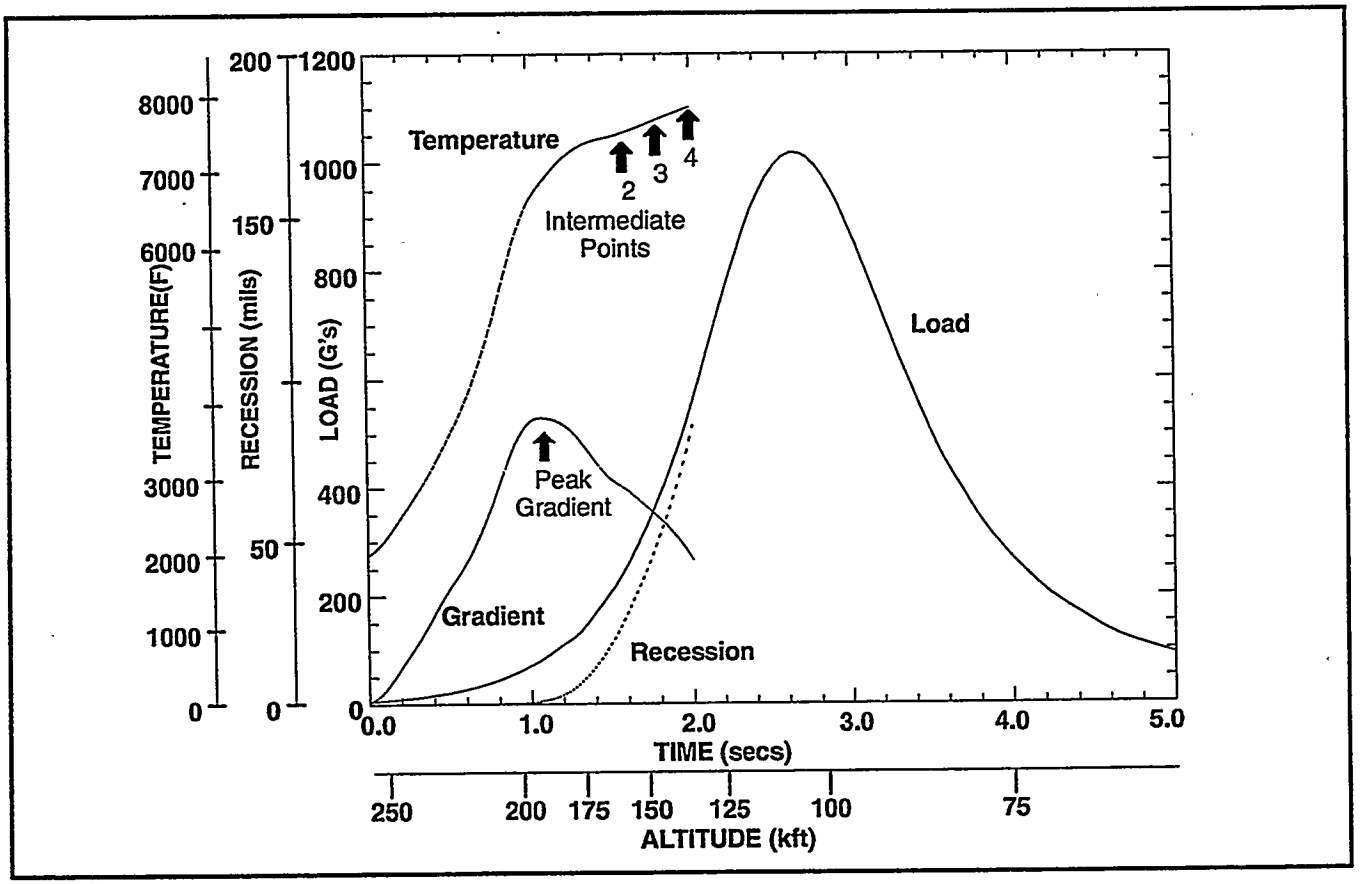

Figure 3-29. Critical Flight Data at Stagnation Point vs. Time - GPHS Aeroshell Cassini Face-On-Stable -90° Trajectory

Table 3-8. Summary of Load Cases for Cassini GPHS Aeroshell, -90° Trajectory

	Analysis Time (secs)			
	1.1	1.6	1.8	2.0
Altitude (kft)	188.1	157.3	145.5	134.1
Flight Condition	Maximum Gradient	Intermediate Point 2	Intermediate Point 3	Intermediate Point 4
GPHS Weight (lbs)	3.16	3.13	3.11	3.08
Accel. Load (G's)	88.8	256.4	384.8	558.9
Stagnation Pt. Data				
Temperature (°F)	6867	7473	7635	7798
Gradient (°F)	3749	2803	2423	1881
Ablation (in)	0.0012	0.0284	0.0518	0.0858

A summary of analysis results for the four baseline cases is presented in Table 3-9. The minimum factors of safety in the X and Y directions are similar and are primarily a result of bending in the aeroshell ablating surface induced by the aeropressure loads. At the 1.1 and 1.6 second timepoints, the stress factors of safety are close to 1.0; however, the strain factors of safety are still greater than 2.0. This indicates that the material has yielded, but still retains strain capability and has not failed. Slightly lower factors of safety occur in the area of the lock member, and some local failure is indicated in this region for the 1.6 second timepoint, principally due to the sharp thermal gradient at the edges of the cutout. To evaluate the impact of this local failure, the analysis was rerun at t = 1.6 seconds with the modulus of the failed elements reduced to 100 psi so these elements would carry no load. The results of this analysis indicated no further propagation of the local failure at the 1.6 second timepoint. At the t = 1.8 second timepoint, the minimum stress factor of safety of 1.03 is barely above the failure limit, and the strain factor of safety is dropping rapidly (down to 1.65 in the X direction). The aeroshell design is marginal at this altitude and cannot sustain much additional loading. Again, local failure occurs in the region of the lock member but does not propagate throughout the aeroshell. Though the bending load on the front face of the aeroshell is significantly higher for this case than for the shallow trajectory runs, the steeper thermal gradient indicates the presence of relatively cooler (5000-5500°F) material on the inside surface of the wall which can sustain the majority of the applied loading.

Table 3-9. Summary of Stresses and Strains for the Cassini GPHS Aeroshell -90° Face-On-Stable Trajectory, No Roll

	Analysis Time (secs)			
	1.1	1.6	1.8	2.0
Flight Condition	Maximum Gradient	Intermediate Point 2	Intermediate Point 3	Intermediate Point 4
X DIRECTION				
Stress (ksi)	–2.55	–1.64	–1.22	–1.28
Temperature (°F)	6528	7209	7414	7619
Allowable (ksi)	–3.44	–1.87	–1.26	–0.88
Factor of Safety	**1.351**	**1.146**	**1.034**	**0.687**
Strain (%)	–0.61	–0.73	–1.55	–6.89
Temperature (°F)	5542	6011	6752	7619
Allowable (%)	–1.28	–1.48	–2.55	–4.01
Factor of Safety	**2.084**	**2.027**	**1.648**	**0.582**
Y DIRECTION				
Stress (ksi)	–2.61	–1.61	–1.21	–1.26
Temperature (°F)	6517	7210	7414	7619
Allowable (ksi)	–3.47	–1.87	–1.26	–0.88
Factor of Safety	**1.329**	**1.159**	**1.040**	**0.700**
Strain (%)	–0.59	–0.75	–1.15	4.28
Temperature (°F)	5550	6245	6752	6920
Allowable (%)	–1.28	–1.81	–2.55	2.80
Factor of Safety	**2.160**	**2.406**	**2.219**	**0.654**
Z DIRECTION				
Stress (ksi)	–14.49	–17.09	20.63	19.99
Temperature (°F)	2878	3318	2372	2500
Allowable (ksi)	–19.63	–20.69	24.49	24.55
Factor of Safety	**1.355**	**1.211**	**1.187**	**1.228**
Strain (%)	–0.21	–0.29	0.16	0.17
Temperature (°F)	2985	3318	2372	2500
Allowable (%)	–0.35	–0.45	0.29	0.31
Factor of Safety	**1.699**	**1.577**	**1.756**	**1.800**
SHEAR				
Stress				
Peak τ_{XY} (ksi)	2570	3389	3747	3400
Peak τ_{XZ} (ksi)	3198	3419	3603	3350
Strain				
Peak γ_{XY} (%)	0.85	0.90	1.00	1.01
Peak γ_{XZ} (%)	1.12	0.93	0.90	0.84

Note: Factor of Safety = (Allowable Value)/(Predicted value)

The minimum factors of safety for both stress and strain are well below 1.0 at t = 2.0 seconds, indicating that failure of some portion of the aeroshell has occurred. A closer examination of the factors of safety throughout the aeroshell indicated failure for over 140 elements on the front face of the aeroshell, concentrated in the thin central region of this wall. Once again, the analysis was rerun with a reduced modulus of 100 psi for these failed elements. This modified analysis could not be completed due to numerical divergence and massive distortion of the elements, indicating that the aeroshell did not have sufficient structural capability to sustain the applied loading at t = 2.0 seconds. As a result, it was concluded that the aeroshell has failed at this altitude.

Minimum factor of safety for stress in the X direction is plotted as a function of time and altitude in Figure 3-30. This plot also includes the X stress factor of safety for the center point of the ablating surface through the trajectory. A similar plot for strain factor of safety is presented in Figure 3-31. As can be seen from both plots, the aeroshell fails in the region around t = 1.9 seconds, which corresponds to an altitude of approximately 140 kft. It should be noted that failure of the aeroshell in this context indicates the inability of the ablating surface to withstand further aero loading. It is possible that the aeroshell will maintain some structural integrity following the failure of this surface and that the GIS could be retained in the chamfers for some amount of time after the initial failure. However, the inner cavity of the aeroshell (including the GIS) will now be exposed to the flow and its associated aero and thermal loading. Due to the complex nature of the flow in and around the GIS, the shock-interaction heating amplification and internal pressurization that will occur in the aeroshell interior, and the extreme difficulty in effectively analyzing these phenomena, it was assumed that failure of the ablating surface of the aeroshell would result in immediate release of the GIS.

Stresses and strains in the Z direction of the aeroshell are caused principally by the extreme thermal gradients resulting from the rapid reentry heating of the body. Though the minimum factors of safety in stress are fairly low in the Z direction (reaching a minimum of 1.19 at t = 1.8 seconds), the minimum factors of safety in strain are somewhat higher (1.58 at t = 1.6 seconds). This is not considered a critical stress condition because these minima are localized, stresses in the Z direction caused by aero loading are not significant, and aeroshell failure cannot be caused by thermal stresses alone due to the nonlinear plastic behavior of the FWPF material.

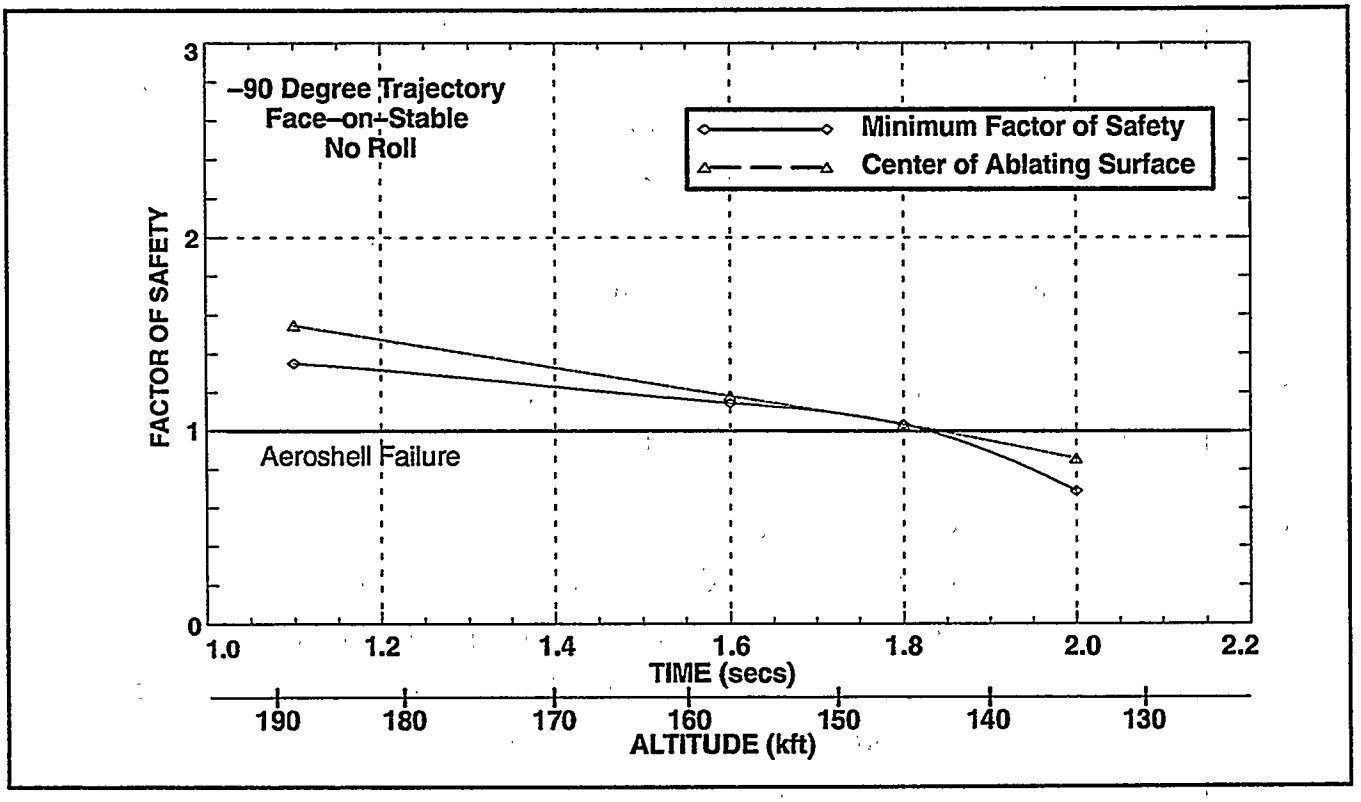

Figure 3-30. Factor of Safety vs. Time - X Direction Stress - GPHS Aeroshell

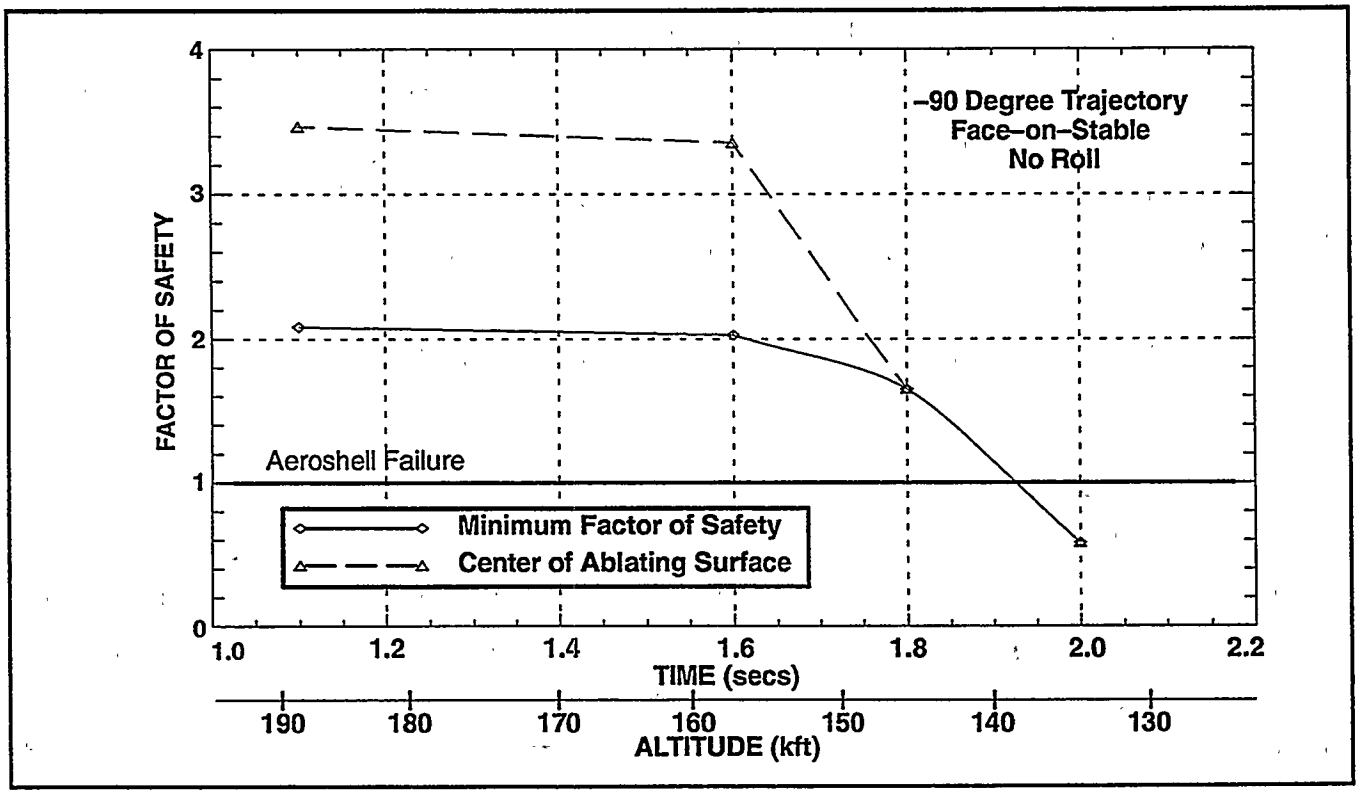

Figure 3-31. Factor of Safety vs. Time - X Direction Strain - GPHS Aeroshell

A contour plot of X stress factor of safety at t = 2.0 seconds is shown in Figure 3-32, indicating regions where initial structural failure of the aeroshell is predicted. As discussed above, these initial failures were calculated to propagate across the thin area of the ablating face, resulting in an inability to withstand the reentry aeropressure loading. A deflected shape of the GPHS aeroshell under loading at the 2.0 second timepoint is illustrated in Figure 3-33. The analysis results also indicated that the maximum gap closure between the GIS and the aeroshell at the point of GIS tangency is approximately 0.047 inches at t = 2.0 seconds, at which point failure has already been predicted for the ablating wall of the aeroshell. Therefore, the GIS will not contact the aeroshell (except at the chamfers where it is supported) or provide any bending support to the aeroshell wall prior to the predicted structural failure of the ablating aeroshell surface, though some compression of the CBCF insulator will occur.

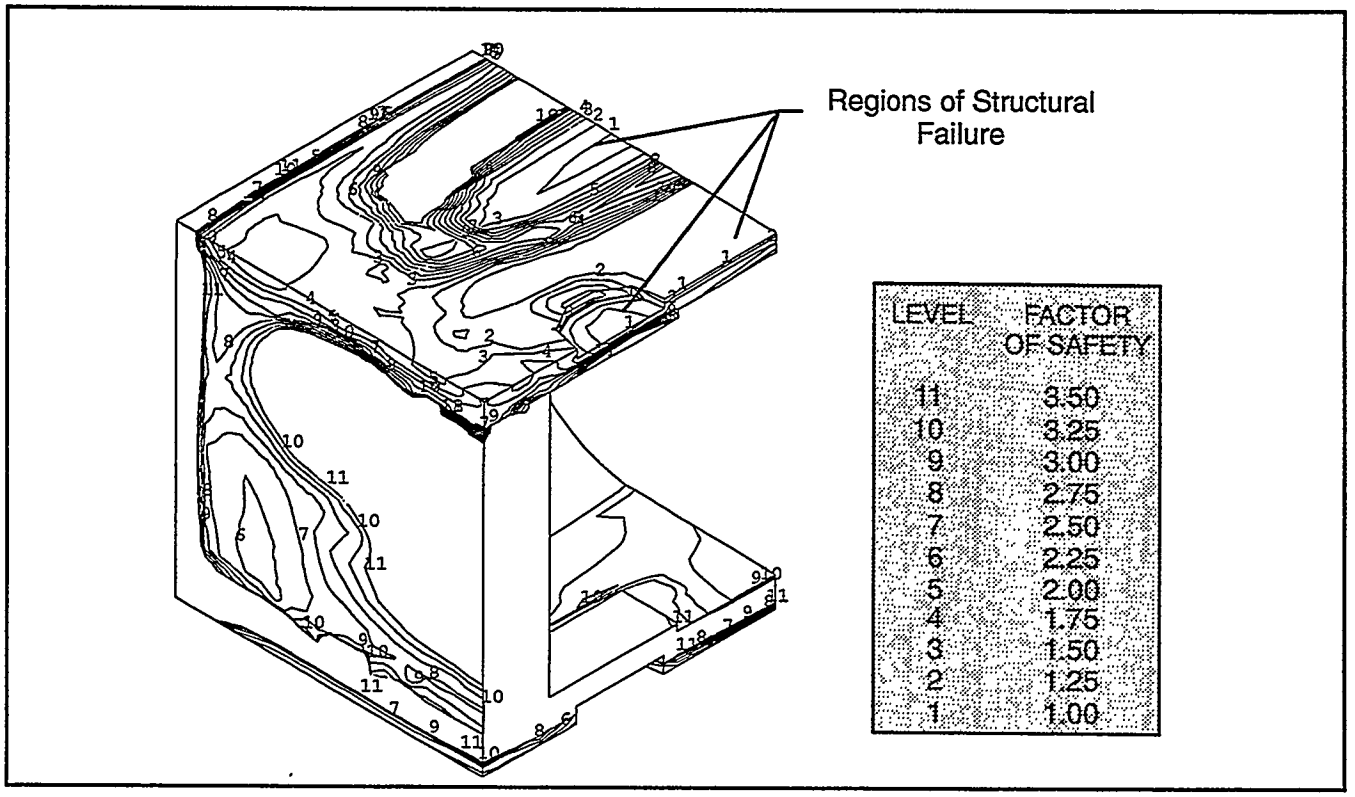

Figure 3-32. X Stress Factor of Safety Contours, T = 2.0 Secs, Alt = 134 kft Cassini GPHS Aeroshell, 90° Face-On-Stable Trajectory, No Roll

The aeroshell steep trajectory thermostructural analysis and results are documented in Reference 3-3.

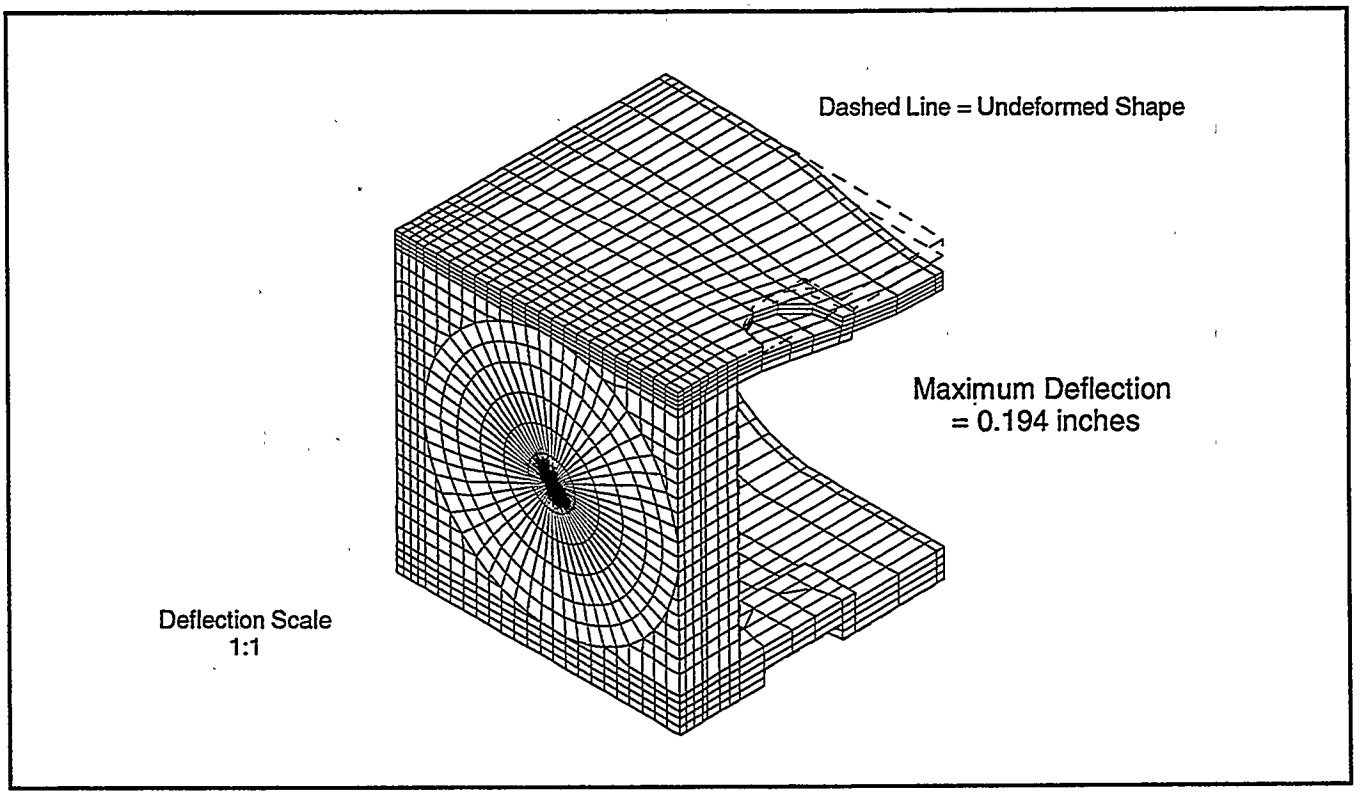

**Figure 3-33. Deflected Shape, Time = 2.0 Secs, Alt = 134 kft
Cassini GPHS Aeroshell, -90° Face-On-Stable Trajectory, No Roll**

Intermediate Trajectory (-20°): In order to assist in the selection of the intermediate path angle, thermal loads and ablations from the critical timepoint for the shallow trajectory (t = 26 seconds) were combined with incrementally increasing aero loads until aeroshell failure occurred. This failure was predicted for a loading of approximately 230 to 250 Gs (roughly 3.5 times the actual loading for the shallow trajectory). It was assumed that temperature and ablation profiles for the intermediate trajectory will be similar to those for the shallow trajectory. Based on this predicted deceleration loading, combined with data correlating peak reentry loading to path angle, it was estimated that failure of the aeroshell would occur for path angles exceeding -18°. A path angle of -20° was chosen for the intermediate trajectory analysis, such that aeroshell failure and GIS release would be predicted and further analysis of the GIS reentry could be accomplished.

Thermostructural analysis was completed for the intermediate (-20°) reentry condition with a face-on-stable attitude, which is the most critical orientation for thermostructural evaluation. The SINRAP transient thermal analysis had progressed through t = 7.2 seconds, which corresponds to an altitude of approximately 138 kft, at which point burnthrough of the aeroshell was predicted. However, based on the temperature, ablation,

and deceleration load histories, it was estimated that thermostructural failure of the aeroshell would occur prior to burnthrough for this trajectory. Data from the SINRAP analysis was reviewed and cross-plotted with deceleration loads resulting from the 3DOF runs (see Figure 3-34). A total of four timepoints along this trajectory were analyzed in detail, including the point representing the maximum temperature gradient at the stagnation point (t = 2.5 seconds). The remaining analysis points were intermediate times in the trajectory up to the point at which structural failure of the aeroshell was predicted.

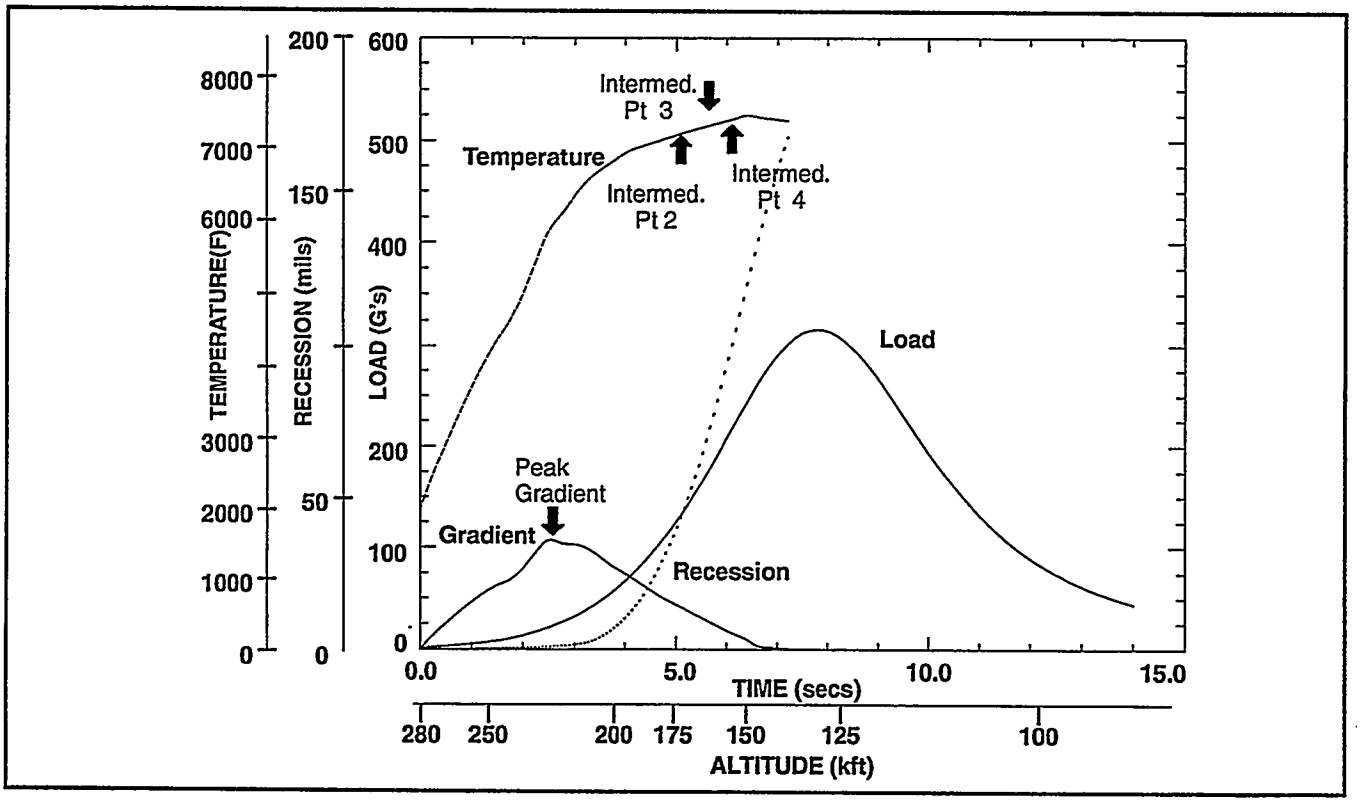

Figure 3-34. Critical Flight Data at Stagnation Point vs. Time - GPHS Aeroshell Cassini -20° Trajectory, Face-On-Stable Attitude

Load conditions at the various timepoints are summarized in Table 3-10. The peak aeroshell temperature at the t = 6.0 second analysis point is approximately 500°K higher than the maximum predicted temperature for the shallow trajectory. In addition, the aeroshell experiences significantly more severe reentry decelerations (approximately five times higher) and ablation compared to the shallow reentry conditions.

Table 3-10. Summary of Load Cases for Cassini GPHS Aeroshell, -20° Trajectory

	Analysis Time (secs)			
	2.5	5.2	5.8	6.0
Altitude (kft)	227.0	171.9	160.8	157.3
Flight Condition	Maximum Gradient	Intermediate Point 2	Intermediate Point 3	Intermediate Point 4
GPHS Weight (lbs)	3.16	3.11	3.08	3.07
Accel. Load (G's)	21.1	140.1	189.9	208.0
Stagnation Pt. Data				
Temperature (°F)	5818	7208	7321	7358
Gradient (°F)	1516	544	331	261
Ablation (in)	0.0009	0.0480	0.0807	0.0935

A summary of analysis results for the four baseline cases is presented in Table 3-11. The minimum factors of safety in the X and Y directions are similar and are primarily a result of bending in the aeroshell ablating surface induced by the aeropressure loads. At the 2.5 and 5.2 second timepoints, the stress factors of safety are approaching 1.0; however, the strain factors of safety are still greater than 1.5. This indicates that the material has yielded, but still retains strain capability and has not failed. Slightly lower factors of safety occur in the area of the lock member, principally due to the sharp thermal gradient at the edges of the cutout. At the t = 5.8 second timepoint (altitude = 161 kft), the minimum stress factor of safety of 1.02 is barely above the failure limit, and the strain factor of safety has dropped considerably (down to 1.05 in the X direction). The aeroshell design is marginal at this altitude and cannot sustain additional loading of any significance. Local failures were also predicted in the region of the lock member at this timepoint. To evaluate the impact of these local failures, the analysis was rerun at t = 5.8 seconds with the modulus of the failed elements reduced to 100 psi so these elements would carry no load. The analysis results indicated no significant propagation of these local failures.

Table 3-11. Summary of Stresses and Strains for the Cassini GPHS Aeroshell, -20° Face-On-Stable Trajectory, No Roll

	Analysis Time (secs)			
	2.5	5.2	5.8	6.0
Flight Condition	Maximum Gradient	Intermediate Point 2	Intermediate Point 3	Intermediate Point 4
X DIRECTION				
Stress (ksi)	–5.00	–3.09	–2.70	–2.93
Temperature (°F)	5769	6491	6866	6916
Allowable (ksi)	–8.87	–3.54	–2.77	–2.67
Factor of Safety	**1.775**	**1.148**	**1.024**	**0.911**
Strain (%)	0.12	–1.41	3.04	8.97
Temperature (°F)	3014	6480	7174	7237
Allowable (%)	0.38	–2.14	3.19	3.29
Factor of Safety	**3.306**	**1.515**	**1.050**	**0.367**
Y DIRECTION				
Stress (ksi)	–5.28	–1.68	2.27	–3.53
Temperature (°F)	5746	7169	6997	6516
Allowable (ksi)	–9.15	–1.99	2.51	–3.47
Factor of Safety	**1.733**	**1.190**	**1.105**	**0.984**
Strain (%)	0.12	–0.45	2.71	5.33
Temperature (°F)	2581	6013	7099	7147
Allowable (%)	0.35	–1.48	3.08	3.15
Factor of Safety	**2.880**	**3.280**	**1.136**	**0.591**
Z DIRECTION				
Stress (ksi)	–15.85	19.40	18.08	17.06
Temperature (°F)	2826	3289	3577	3673
Allowable (ksi)	–19.56	25.44	26.10	26.35
Factor of Safety	**1.234**	**1.311**	**1.444**	**1.545**
Strain (%)	–0.23	0.17	0.15	–0.38
Temperature (°F)	2826	3289	3577	5870
Allowable (%)	–0.33	0.44	0.56	–1.42
Factor of Safety	**1.426**	**2.575**	**3.631**	**3.784**
SHEAR				
Stress				
Peak τ_{XY} (ksi)	2222	2928	2482	2550
Peak τ_{XZ} (ksi)	2830	2146	2265	2277
Strain				
Peak γ_{XY} (%)	0.57	0.97	3.58	4.64
Peak γ_{XZ} (%)	0.67	0.86	5.52	8.09

Note: Factor of Safety = (Allowable Value)/(Predicted value)

The minimum factors of safety for both stress and strain are well below 1.0 at t = 6.0 seconds (altitude = 157 kft), indicating that failure of some portion of the aeroshell has occurred. A closer examination of the factors of safety throughout the aeroshell indicated failure for a large number of elements on the front face of the aeroshell, concentrated in the thin central region of this wall. Once again, the analysis was rerun with a reduced modulus of 100 psi for these failed elements. This modified analysis could not be completed due to numerical divergence and massive distortion of the elements, indicating that the aeroshell did not have sufficient structural capability to sustain the applied loading at t = 6.0 seconds. As a result, it was concluded that the aeroshell has failed at this altitude.

Minimum factor of safety for stress in the X direction is plotted as a function of time and altitude in Figure 3-35. This plot also includes the X stress factor of safety for the center point of the ablating surface through the trajectory. A similar plot for strain factor of safety is presented in Figure 3-36. As can be seen from both plots, the aeroshell fails at approximately 5.85 seconds, which corresponds to an altitude of 160 kft. As with the steep trajectory, it was assumed that failure of the ablating surface of the aeroshell would result in immediate release of the GIS.

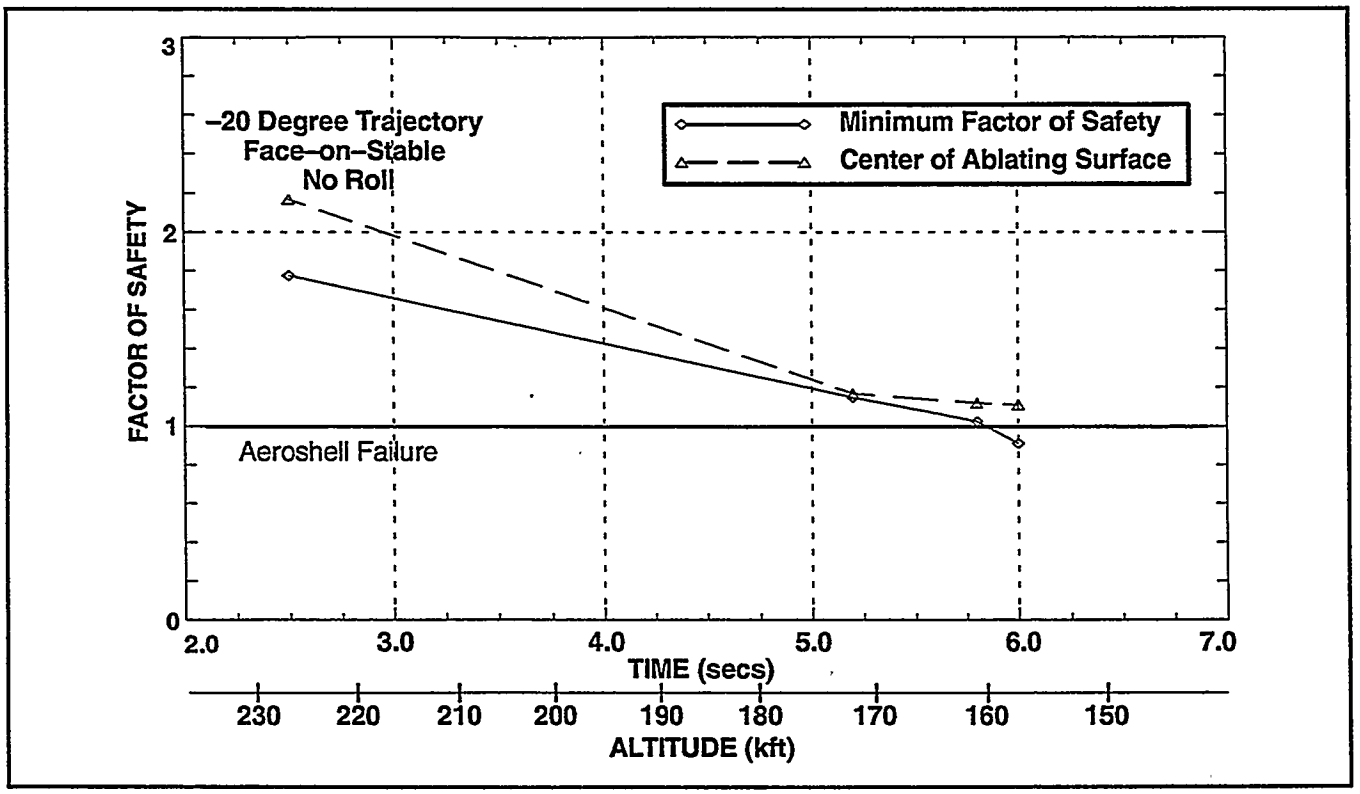

Figure 3-35. Factor of Safety vs. Time - X Direction Stress - GPHS Aeroshell

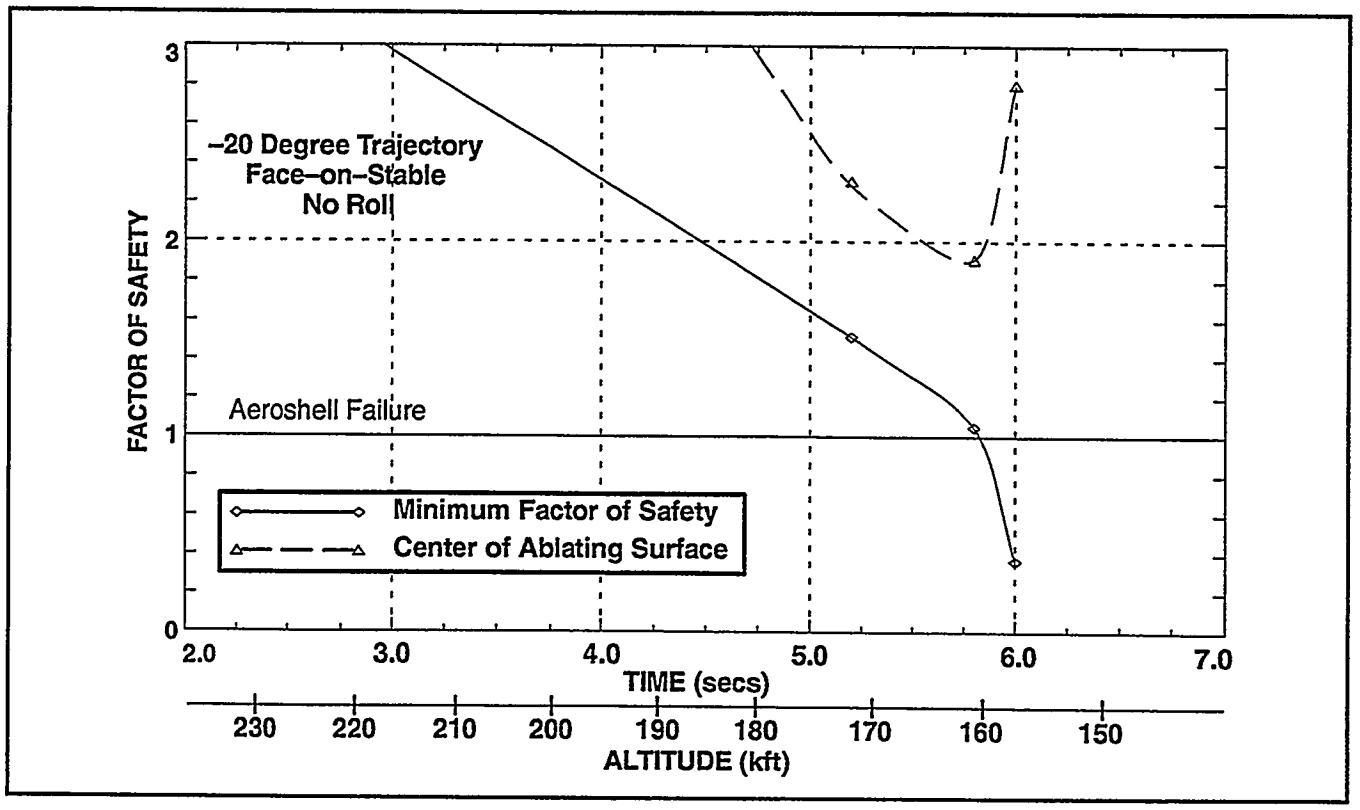

Figure 3-36. Factor of Safety vs. Time - X Direction Strain - GPHS Aeroshell

Stresses and strains in the Z direction of the aeroshell are caused principally by the extreme thermal gradients resulting from the rapid reentry heating of the body. Though the minimum factors of safety in stress are fairly low in the Z direction (reaching a minimum of 1.23 at t = 2.5 seconds), the corresponding factor of safety in strain of 1.43 is somewhat higher. This is not considered a critical stress condition because these minima are localized, stresses in the Z direction caused by aero loading are not significant, and aeroshell failure cannot be caused by thermal stresses alone due to the nonlinear plastic behavior of the FWPF material.

A contour plot of X stress factor of safety at t = 6.0 seconds is shown in Figure 3-37, indicating regions where initial structural failure of the aeroshell is predicted. As discussed above, these initial failures were calculated to propagate across the thin area of the ablating face, resulting in an inability to withstand the reentry aeropressure loading. A deflected shape of the GPHS aeroshell under loading at the 6.0 second timepoint is illustrated in Figure 3-38. The analysis results also indicated that the GIS will not contact the aeroshell (except at the chamfers where it is supported) or provide any bending support

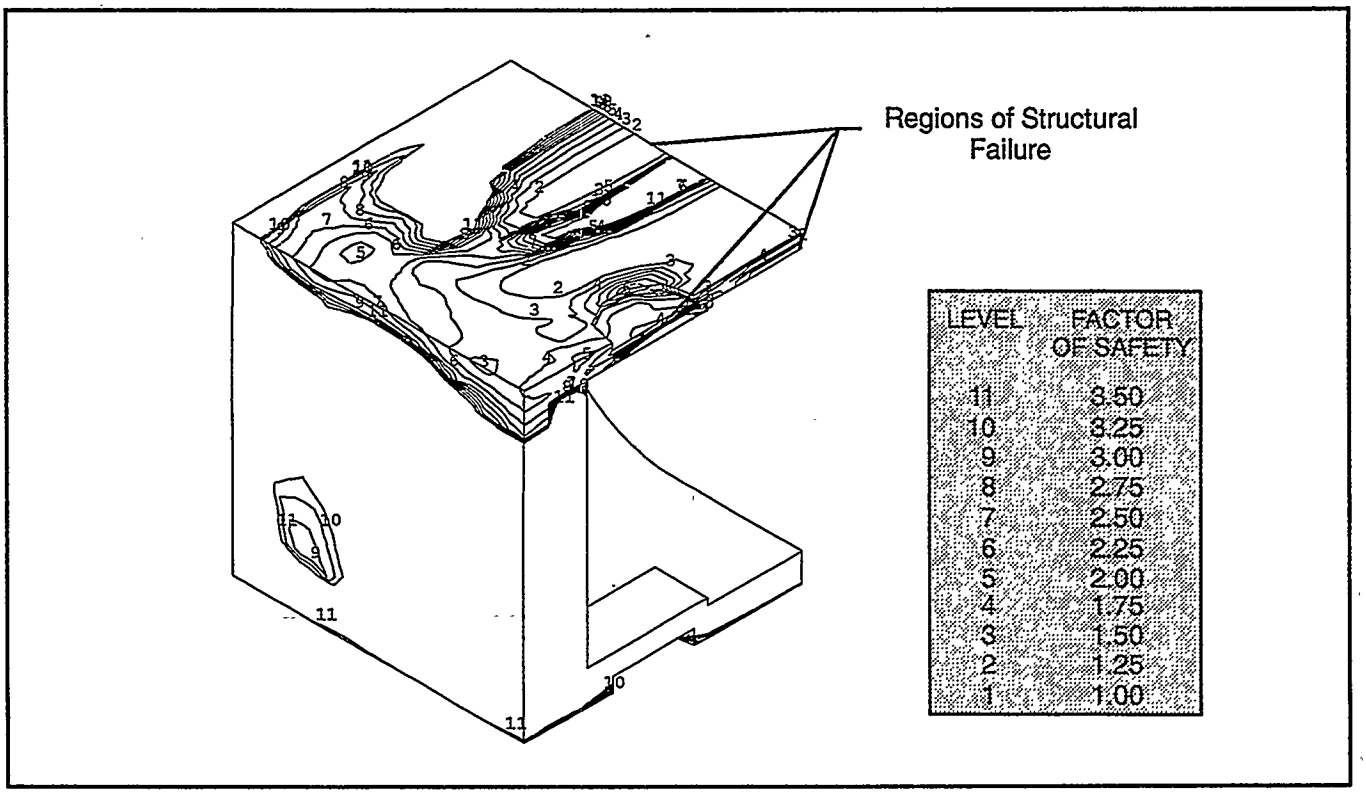

Figure 3-37. X Stress Factor of Safety Contours, T = 6.0 Secs., Alt = 157 kft Cassini GPHS Aeroshell, -20° Face-On-Stable Trajectory, No Roll

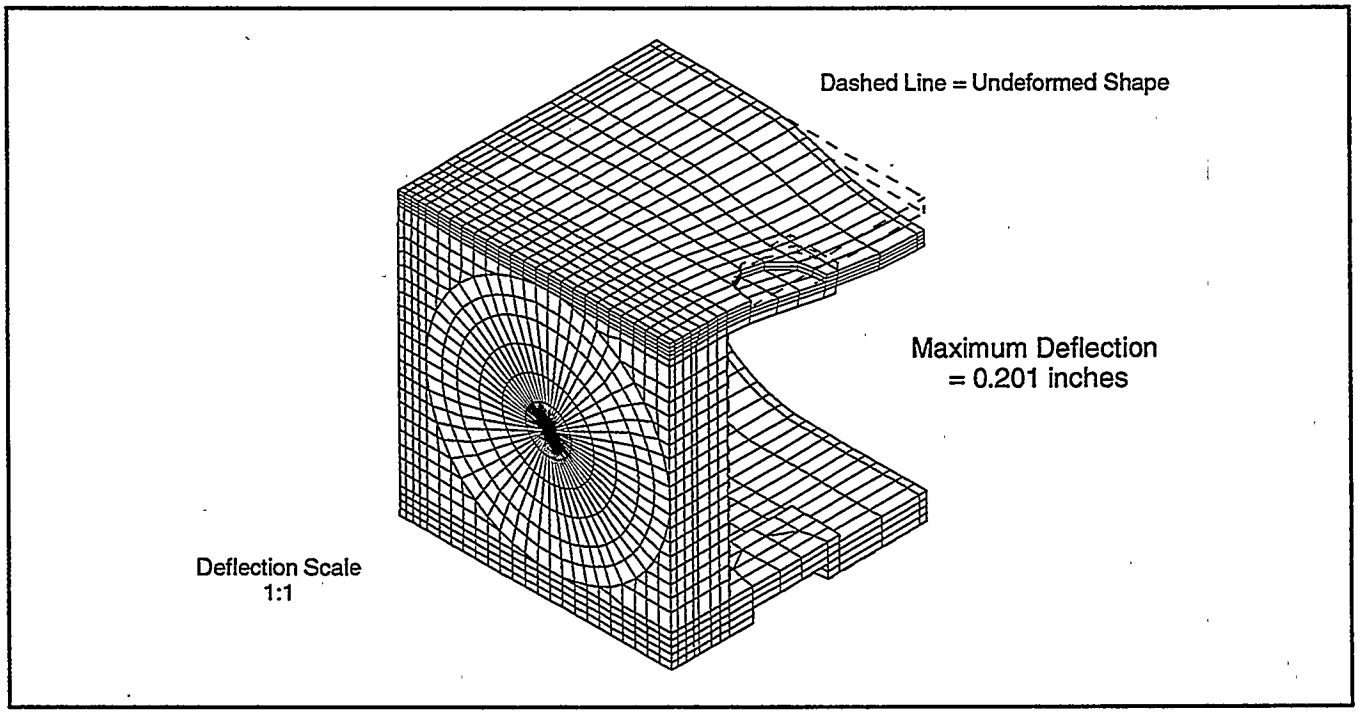

Figure 3-38. Deflected Shape, T = 6.0 Secs., Alt = 157 kft Cassini GPHS Aeroshell, -20° Face-On-Stable Trajectory, No Roll

to the aeroshell wall prior to the predicted structural failure of the ablating aeroshell surface, though some compression of the CBCF insulator will occur.

Based on the intermediate trajectory analysis results, a revised estimate was made of the reentry path angle above which aeroshell structural failure would nominally be predicted. The 160 kft failure altitude for the intermediate trajectory corresponds to a deceleration load of approximately 195 Gs. The original estimate of 230 - 250 Gs failure load was based upon a model utilizing the critical temperatures and ablations from the shallow trajectory, with an incremented deceleration loading. However, since the intermediate trajectory temperatures and ablations are higher than those for the shallow trajectory, the reduction in the predicted critical failure loading is understandable. Utilizing the plot of maximum deceleration load versus reentry path angle shown in Figure 3-39, and taking into account that the intermediate trajectory results slightly overpredict temperature and recession, a revised value of -16° was established for the critical reentry path angle for aeroshell failure.

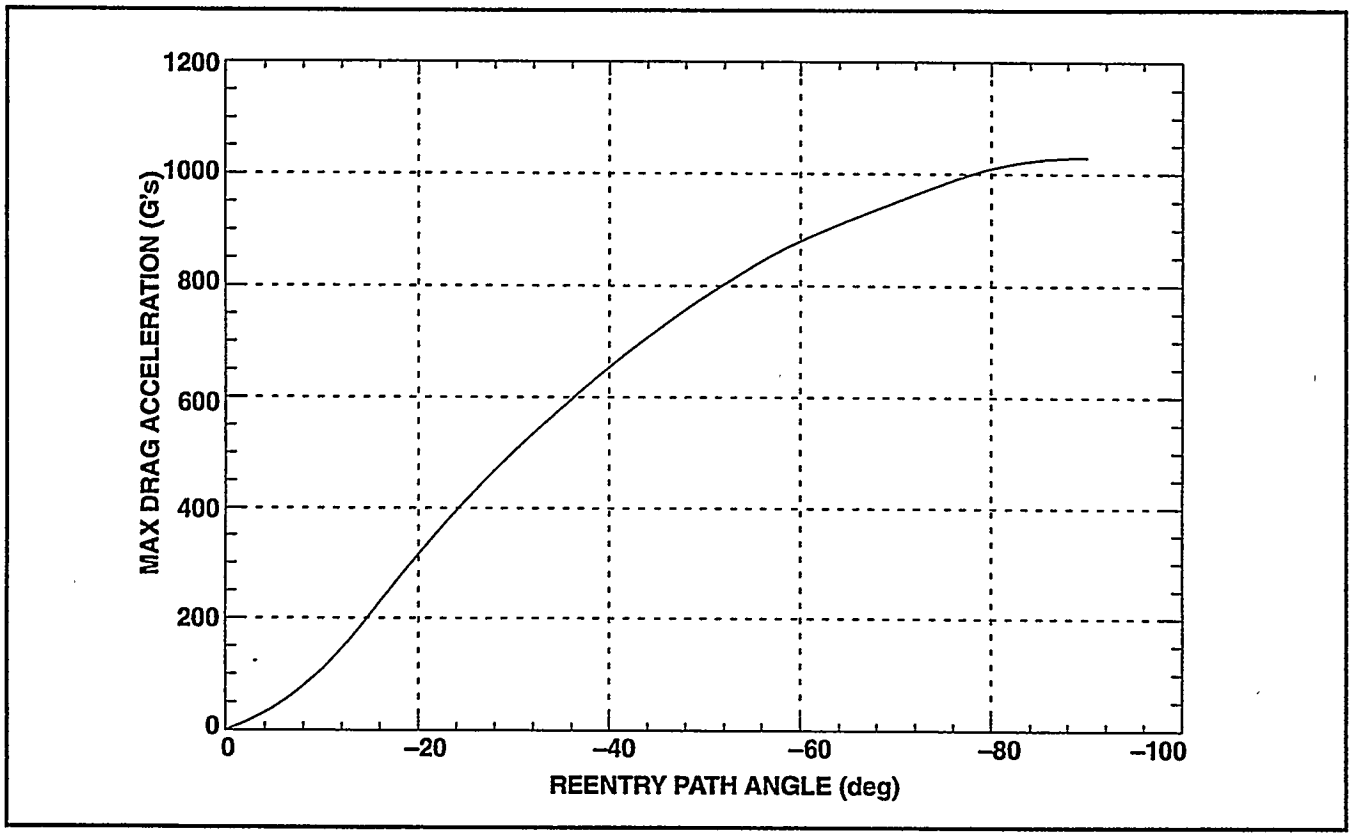

Figure 3-39. Maximum Drag Acceleration vs. Path Angle - Gravity Assist Reentry

The aeroshell intermediate trajectory thermostructural analysis and results are documented in Reference 3-4.

Random Tumbling Trajectories: The reentry analyses were performed primarily for the face-on-stable aeroshell attitude because this is the most critical condition for the body. The peak aeroshell temperatures and ablations for the aeroshell are lower for a random tumbling reentry because of the greater surface area exposed to the flow by the tumbling body. In addition, the more uniform temperature of the aeroshell body due to tumbling will reduce the severity of stresses induced by thermal gradients. The reentry decelerations are approximately the same for any aeroshell attitude; however, the centrifugal forces due to tumbling will oppose the aeropressures induced by deceleration and slightly reduce the critical bending stresses on the front face of the aeroshell body. As a result, the random tumbling reentry can generally be considered less severe than the face-on-stable attitude for the determination of aeroshell survivability.

Despite this mitigation of stresses and strains for the random tumbling reentry, an assessment of aeroshell survivability for these conditions is still important to the probabilistic determination of aeroshell survivability. Transient SINRAP thermal analyses of a random tumbling aeroshell were performed for both the steep (-90°) and intermediate (-20°) flight path angles. These SINRAP analyses did not incorporate CFD analytical techniques but were instead based on equilibrium heating values and extrapolated b' curves. This type of analysis has been shown to be somewhat conservative based on the results of the FOS reentry work with CFD incorporated. Analysis of the shallow trajectory for a random tumbling aeroshell was not necessary because the aeroshell has sufficient structural capability to survive the same reentry conditions in the more severe FOS attitude. This leads directly to the conclusion that the aeroshell will survive a random tumbling shallow reentry. Similarly, since the FOS aeroshell failed structurally for the steep trajectory well before the peak heating and peak load conditions were reached, it can be inferred that the random tumbling aeroshell will also fail for the steep reentry conditions. As a result, the focus of the random tumbling analysis was the intermediate trajectory where aeroshell survivability/failure is marginal.

Thermostructural analysis was completed for the intermediate trajectory (-20°) random tumbling reentry condition for the critical timepoint of t = 8.0 seconds where both maximum temperature and maximum load conditions are attained. The loads at this time point are

summarized in Table 3-12, with comparative data for the FOS reentry at t = 6.0 seconds where aeroshell failure was predicted. The peak reentry deceleration of 319.8 Gs is comparable to the peak loading for the FOS attitude of 315.0 Gs, while temperatures, ablations, and gradients are reduced from the FOS values as expected because of the random tumbling attitude. It should be noted that the maximum ablation predicted for the random tumbling reentry is approximately 0.067 inches, while burnthrough of the aeroshell was predicted for the FOS attitude. Aeroshell weight for the random tumbling reentry is noticeably lower than for the FOS reentry because ablation is occurring on all sides of the module, not just the front face. An additional centrifugal force due to aeroshell tumbling was also applied to the model. This force was based on a nominal tumbling rate of 500 deg/sec derived from motion studies and is relatively insignificant compared to the other forces on the aeroshell body.

Table 3-12. Comparison of Load Cases for Cassini GPHS Aeroshell - (-20°) Trajectory, FOS vs. Random Tumbling Attitude

	Aeroshell Attitude / Time (secs)	
	Random Tumbling t = 6.0 secs	Face-on-Stable t = 6.0 secs
Altitude (kft)	126.2	157.3
Flight Condition	Maximum Load and Temperature	Intermediate Point
GPHS Weight (lbs)	2.90	3.07
Accel. Load (G's)	319.8	208.0
Stagnation Pt. Data		
Temperature (°F)	6874	7358
Gradient (°F)	121	261
Ablation (in)	0.0674	0.0935

A summary of analysis results for the random tumbling case is presented in Table 3-13. The minimum factors of safety for X direction stress and strain are 1.093 and 1.189, respectively, indicating that the aeroshell has sufficient structural capability to withstand the reentry load conditions but cannot sustain much additional loading. In addition, some non-propagating local failures around the lock member are predicted for this load case. The Z

Table 3-13. Summary of Stresses and Strains for the Cassini GPHS Aeroshell -20° Random Tumbling Trajectory, T = 8.0 Secs, Alt = 126 kft

	Stress (ksi)	Temp (°F)	Allow. (ksi)	Factor of Safety	Strain (%)	Temp (°F)	Allow. (%)	Factor of Safety
X Direction	–2.53	6867	–2.77	**1.093**	2.15	6759	2.56	**1.189**
Y Direction	2.63	6755	2.99	**1.136**	2.01	6774	2.59	**1.287**
Z Direction	–9.76	5404	–14.41	**1.477**	–0.37	4931	–1.28	**3.486**

direction minimum strain factor of safety of 3.486 indicates no critical loading in this direction, which is understandable since temperature gradients are relatively minor for the random tumbling reentry. Deflection results indicate gap closures of 0.047 inches between the CBCF insulator and the aeroshell wall. This is very similar to the predicted relative deflection for the FOS attitude and indicates that the GIS will provide no support to the bending aeroshell walls. In summation, the analysis results indicate that the aeroshell has adequate structural capability to survive the intermediate reentry conditions for a random tumbling attitude.

The results of this random tumbling analysis, as well as the general trend of factor of safety versus deceleration load derived from the FOS analysis for the intermediate trajectory, were used to assess the critical angle for random tumbling aeroshell failure. The random tumbling aeroshell was estimated to fail at a deceleration load of 350 Gs, which corresponds to a path angle of approximately -21°. As expected, this aeroshell failure threshold occurs at a higher angle than the -16° predicted for the FOS attitude.

GIS Analysis

GIS Analysis Approach: The analytical methodology for the analysis of the GIS is very similar to the approach utilized for the Cassini aeroshell and documented in prior reports. The GIS assembly consists of the FWPF graphite impact shell, end cap, and floating membrane, as well as the iridium clad and the plutonium dioxide fuel pellets. An ABAQUS finite element model of the GIS assembly is utilized in conjunction with the detailed

The GIS assembly consists of the FWPF graphite impact shell, end cap, and floating membrane, as well as the iridium clad and the plutonium dioxide fuel pellets. An ABAQUS finite element model of the GIS assembly is utilized in conjunction with the detailed nonlinear model of the FWPF material that was developed for the aeroshell. Aeropressures are applied to the model and balanced by deceleration loads. Thermal loads in the form of nodal temperatures are applied concurrently with the reentry load conditions, and static analyses are run at selected timepoints in the trajectory that represent key conditions that could potentially produce the worst-case stress conditions in the FWPF shell. Stress and strain results are evaluated against temperature dependent material allowables for every element in the GIS in order to determine the structural adequacy of the shell for the given reentry conditions.

ABAQUS Model of GIS Assembly: The nonlinear ABAQUS finite element model of the GIS assembly is illustrated in Figure 3-40, representing a quarter section of the actual component assembly with plane-of-symmetry boundary conditions in both the axial and circumferential directions. The model, composed entirely of solid elements, includes the GIS, end cap, and floating membrane (all FWPF), as well as the iridium clad and PuO_2 fuel pellets (because of symmetry, the model includes only one of the two fuel pellets). The total weight of the unablated GIS assembly is 1.127 lbs. The nonlinear, temperature-dependent material model utilized for the FWPF components is identical to the one utilized for the Cassini aeroshell. Temperature-dependent, linear isotropic material properties were developed for the clad and fuel pellet based on the existing material property database. A critical feature of the ABAQUS model of the GIS assembly is the utilization of nonlinear contact elements at the GIS/clad and clad/fuel pellet interfaces (see Figure 3-40). These elements carry load in compression only (not tension), and thus are ideally suited for applications where two unattached components may come into contact with each other when loaded. In this case, there exists a diametral gap between the fuel pellet and clad body of approximately 0.036 inches. In addition, the fueled clad rests on internal rings in the GIS which are approximately 0.016 inches larger in diameter than the outer surface of the clad. To properly model the load paths between these components during reentry, nonlinear contact elements are a necessity.

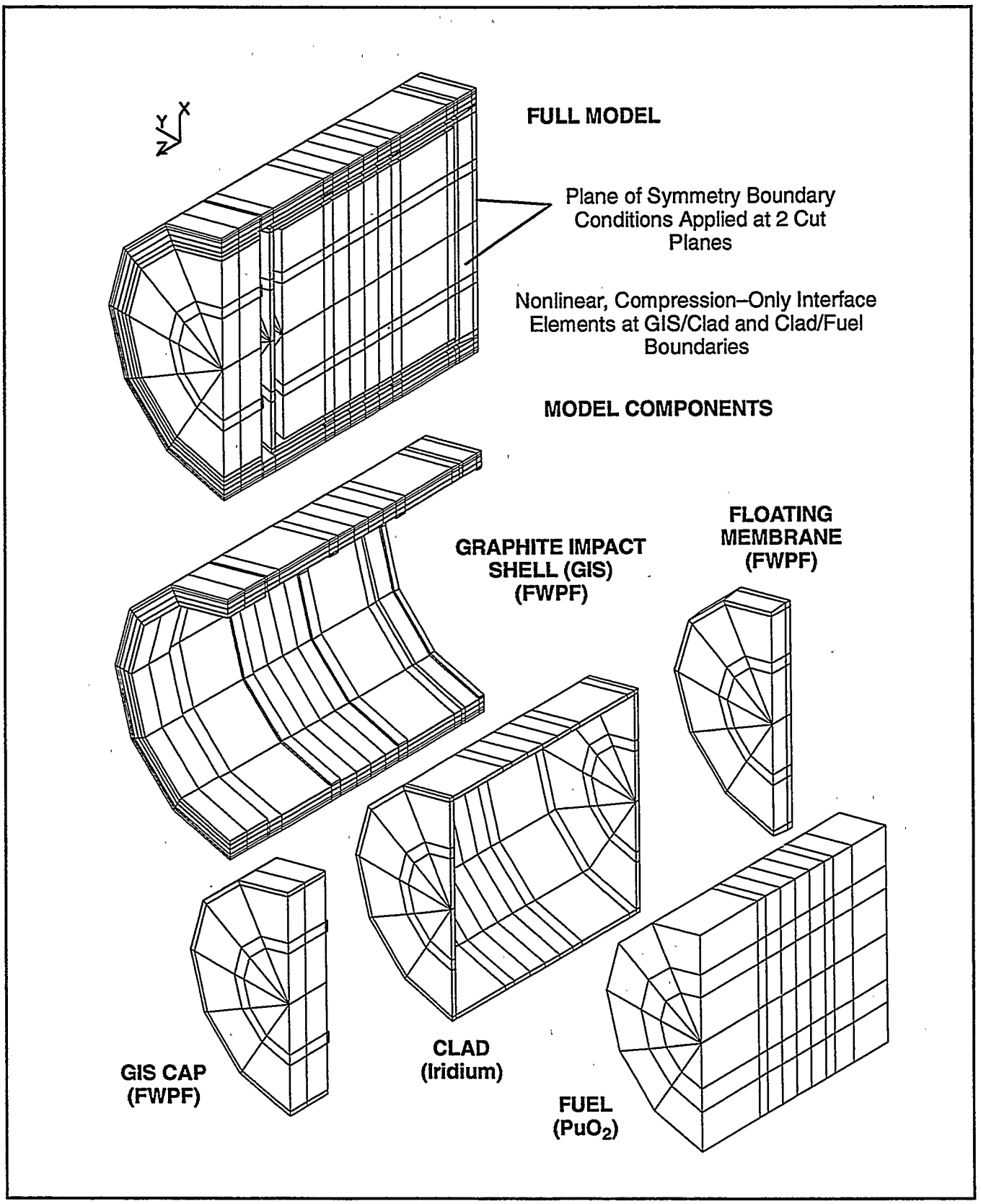

Figure 3-40. ABAQUS Finite Element Model - Graphite Impact Shell Assembly

Reentry deceleration load conditions for the ABAQUS GIS model were obtained from the 3DOF motion analyses performed for the GIS following release from the aeroshell at a specified time and altitude. The deceleration loading was balanced by an applied pressure distribution on the outer surface of the GIS model. This pressure was assumed to have a cosine distribution, with the peak occurring at the model cut plane and dropping off to zero 90 degrees around the model. Temperatures and ablations for the model were obtained from the results of one-dimensional REKAP thermal analyses performed along the stagnation line (note that no CFD techniques were incorporated in this analysis). The model shape was adjusted to match the predicted ablated shape at a given altitude. The entire outer surface of the model was conservatively assumed to ablate the same amount, in this case the maximum amount at the stagnation point. In-depth temperatures were applied to all components in the model, including the clad and fuel pellet. Temperatures varied radially but were assumed to be constant in both the axial and circumferential directions. A single point on the axis of the model was constrained to eliminate any residual free-body motion.

GIS Results - Steep Trajectory: Thermostructural reentry analysis of the Graphite Impact Shell (GIS) assembly was completed for the steep (-90 degree) reentry condition. This analysis follows the steep trajectory thermostructural prediction for the Cassini aeroshell, which nominally indicated aeroshell failure at 1.9 seconds (altitude = 140 kft). Instantaneous release of the GIS at aeroshell failure is assumed. Data from the REKAP analysis was reviewed and cross-plotted with deceleration loads resulting from the 3DOF runs (see Figure 3-41). A total of three timepoints along this trajectory were analyzed in detail. These points represented critical times in the trajectory, specifically the maximum gradient condition (t = 2.01 secs.), the combined maximum temperature and deceleration load condition (t = 2.67 secs.), and a critical ablation condition (t = 4.00 secs.).

Load conditions at the various timepoints are summarized in Table 3-14. The peak GIS temperatures and decelerations are comparable to those predicted for the aeroshell for the steep trajectory. As can be seen in Figure 3-41, the GIS decelerates rapidly following release, attaining maximum temperature and load conditions within the first second after being exposed to the flow. Thermal gradients are extremely high because of the sudden exposure to the reentry environments. Ablation rises rapidly before leveling off around t = 4.0 seconds as the loads and temperatures drop rapidly.

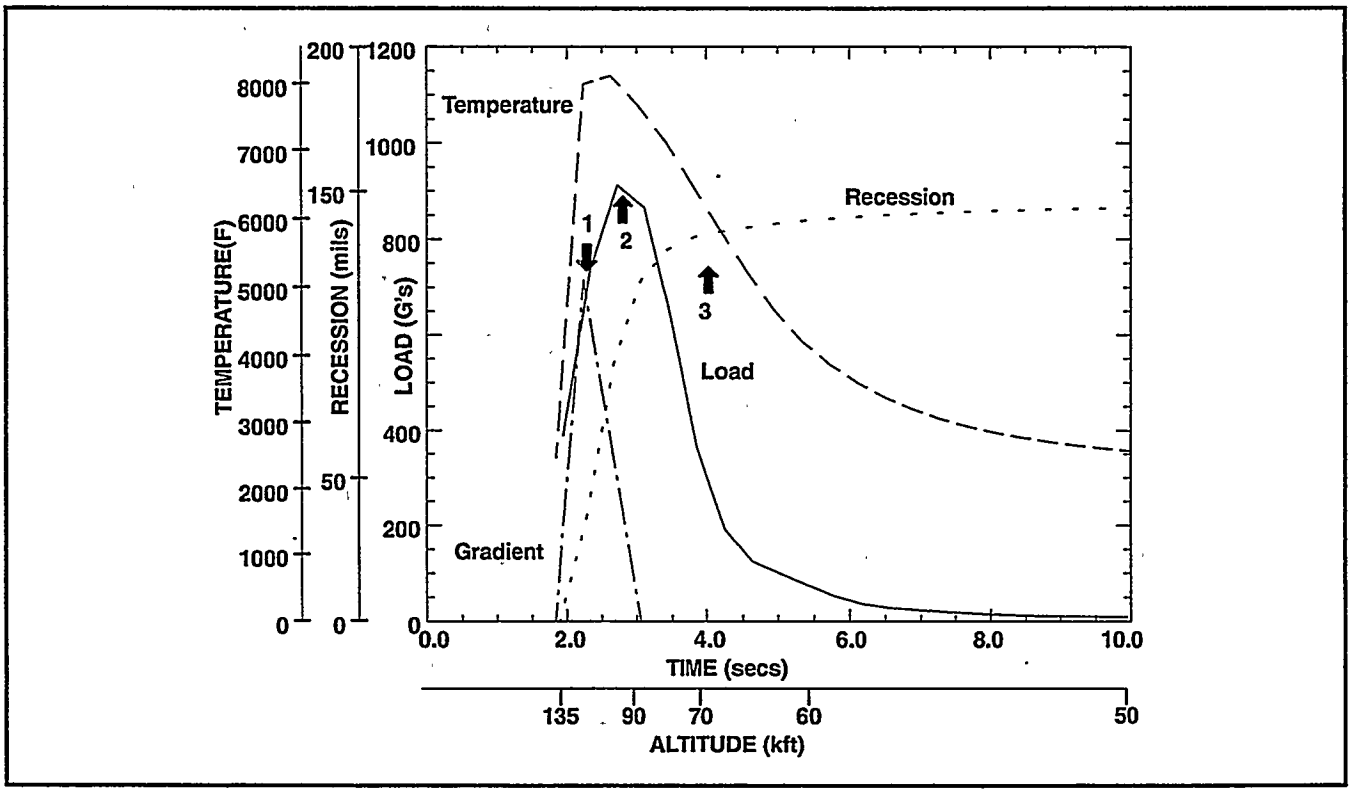

Figure 3-41. Critical Flight Data at Stagnation Point vs. Time - GIS Assembly Cassini Steep (-90°) Trajectory, Face-On-Stable Attitude, 1.9 Sec. Release

Table 3-14. Summary of Load Cases for Cassini GIS Assembly - Steep (-90°) Trajectory, 1.9 Sec. Release

	Analysis Time (secs)		
	2.01	2.57	4.00
Altitude (kft)	134.1	104.0	70.5
Flight Condition	Maximum Gradient	Maximum Temperature & Load	Critical Recession
GIS Weight (lbs)	1.11	1.03	0.99
Accel. Load (G's)	388.3	960.0	314.6
Stagnation Pt. Data			
Temperature (°F)	7642	8050	6109
Gradient (°F)	5146	2196	–104
Ablation (in)	0.0063	0.0902	0.1351

A summary of analysis results for the three baseline cases is presented in Table 3-15. In addition, for the most critical load case (t = 2.67 seconds), structural and thermal loads were applied separately to independently assess the effects of each condition. Stresses in the X and Y directions are similar and result from the combined effects of thermal gradients and pressure loads. Stresses in the X direction are higher than those in the Y direction because of the asymmetrical loading of the inside of the GIS by the fueled clad as it shifts forward during reentry. The minimum predicted stress and strain factors of safety in the X direction of 1.42 and 2.40 occur at t = 2.67 seconds and indicate sufficient structural capability to withstand reentry load conditions. A plot of X factors of safety for both stress and strain is presented in Figure 3-42.

Stresses and strains in the Z direction of the GIS are caused principally by the extreme thermal gradients resulting from the rapid reentry heating of the body, which causes much higher thermally-induced expansion on the outer surface of the GIS than on the inside. As can be seen from the data in Table 3-15 and the plot of Z stress and strain factors of safety in Figure 3-43, the factor of safety in stress reaches a minimum of approximately 1.0 at t = 2.67 seconds, which would seem to indicate potential GIS failure based on stress evaluation criteria. However, the minimum Z factor of safety is 2.46, which demonstrates that the GIS does indeed retain structural capability. The critical area of the GIS at this timepoint is the outer surface near the cap, which is at a temperature approaching 8000 degrees F. The material at this temperature is exhibiting perfectly-plastic behavior, in which the stress has reached its maximum value but strain capability still remains. This is the reason why strain factors of safety are the critical item in determining structural capability. A contour plot of the X stress factors of safety in the GIS is presented in Figure 3-44, indicating the highly localized stress minima of 1.0 on the outer surface. It is also important to note that the critical minimum contours do not extend very deeply into the thickness of the GIS. This indicates that only the outer surface of the GIS cannot sustain additional loading, while the majority of the shell has significant structural capability remaining.

Based on the results of the GIS reentry analysis, it can be concluded that the GIS assembly can sustain the specified reentry load conditions for a nominal release from the aeroshell at 1.9 seconds and 140 kft.

Table 3-15. Summary of Stresses and Strains for the Cassini Graphite Impact Shell -90° Face-On Stable Trajectory, 1.9 Sec. Release

	Analysis Time (secs)				
	2.01	2.67			4.00
Flight Condition	Maximum Gradient	Maximum Temperature and Load			Critical Recession
		Combined	Structural	Thermal	
X DIRECTION					
Stress (ksi)	–2.09	–0.50	–5.67	–0.39	–2.05
Temperature (°F)	6513	7785	5854	7785	6213
Allowable (ksi)	–3.48	–0.72	–7.81	–0.72	–4.93
Factor of Safety	**1.666**	**1.421**	**1.379**	**1.846**	**2.408**
Strain (%)	0.10	–0.59	–0.65	–0.19	–0.25
Temperature (°F)	2496	5854	5854	5854	6213
Allowable (%)	0.35	–1.40	–1.40	–1.40	–0.18
Factor of Safety	**3.467**	**2.397**	**2.160**	**7.420**	**6.974**
Y DIRECTION					
Stress (ksi)	–2.09	–0.41	–3.01	–0.39	–1.77
Temperature (°F)	6513	7785	5854	7785	6213
Allowable (ksi)	–3.48	–0.72	–7.81	–0.72	–4.93
Factor of Safety	**1.663**	**1.755**	**2.595**	**1.846**	**2.783**
Strain (%)	0.09	–0.18	–0.20	–0.19	–0.22
Temperature (°F)	2496	5854	5854	5854	6213
Allowable (%)	0.35	–1.40	–1.40	–1.40	–0.18
Factor of Safety	**3.935**	**7.897**	**7.145**	**7.420**	**7.997**
Z DIRECTION					
Stress (ksi)	–2.61	–0.72	0.40	–0.72	1.67
Temperature (°F)	6513	7785	7785	7785	6122
Allowable (ksi)	–3.48	–0.72	0.72	–0.72	5.39
Factor of Safety	**1.333**	**0.991**	**1.812**	**1.000**	**3.233**
Strain (%)	–0.96	–1.81	0.58	–0.96	0.19
Temperature (°F)	6513	7785	7785	7785	6122
Allowable (%)	–2.19	–4.44	4.44	–4.44	1.63
Factor of Safety	**2.278**	**2.456**	**7.692**	**4.625**	**8.464**
SHEAR					
Cap Stress					
Peak X (ksi)	3.45	5.77	–1.29	5.54	6.36
Peak Z (ksi)	–0.45	3.09	0.20	3.08	4.68
Float. Membr. Stress					
Peak X (ksi)	21.63	19.14	–1.01	19.18	17.71
Peak Y (ksi)	–23.76	11.71	–0.31	11.62	4.24

Note: Factor of Safety = (Allowable Value)/(Predicted value)

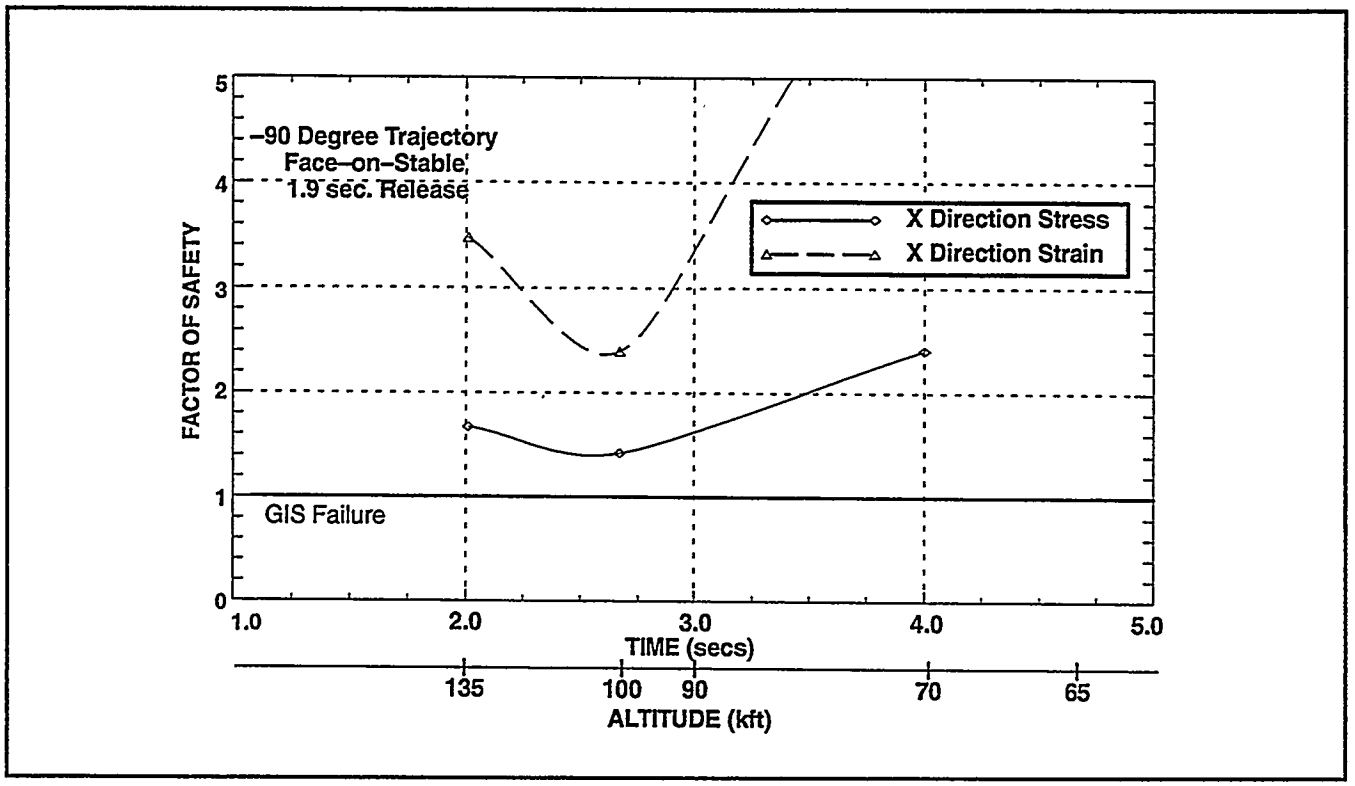

Figure 3-42. Factor of Safety vs. Time - X Direction - Graphite Impact Shell

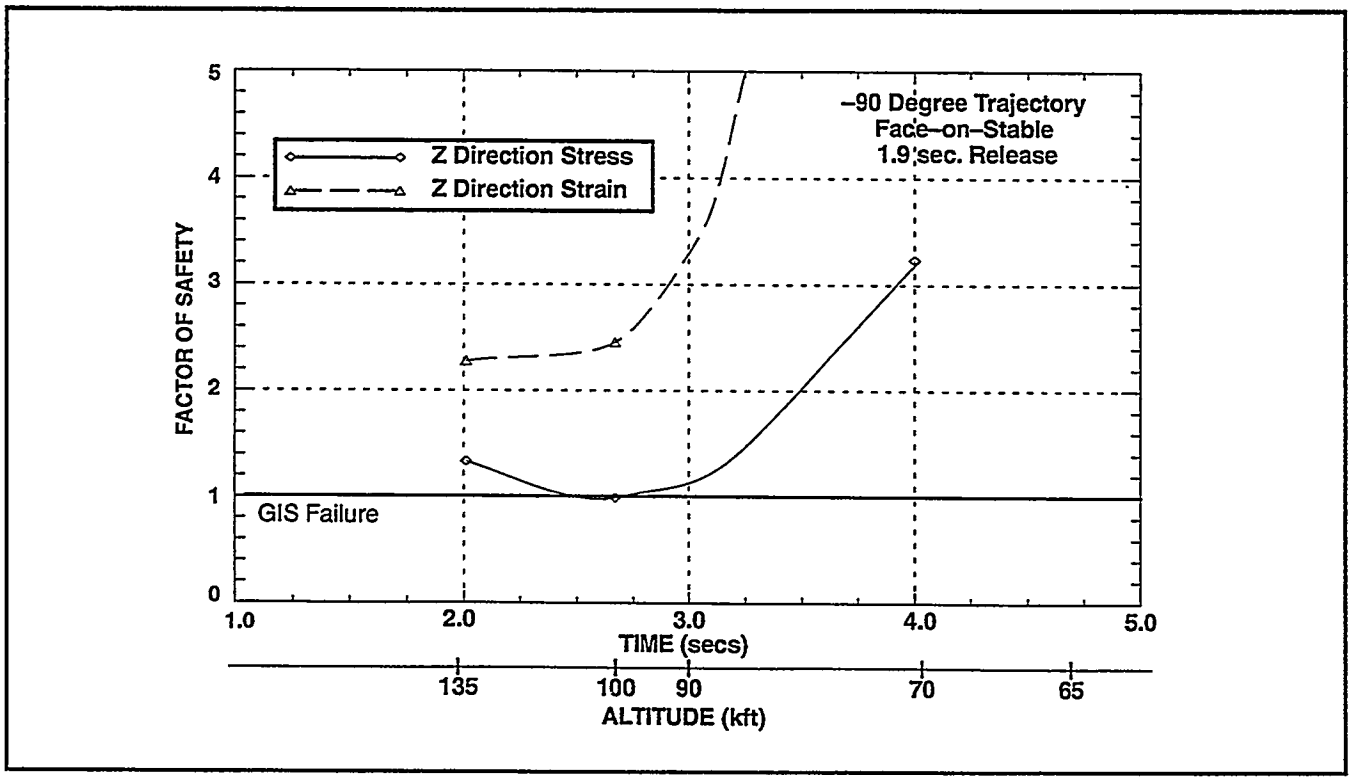

Figure 3-43. Factor of Safety vs. Time - Z Direction - Graphite Impact Shell

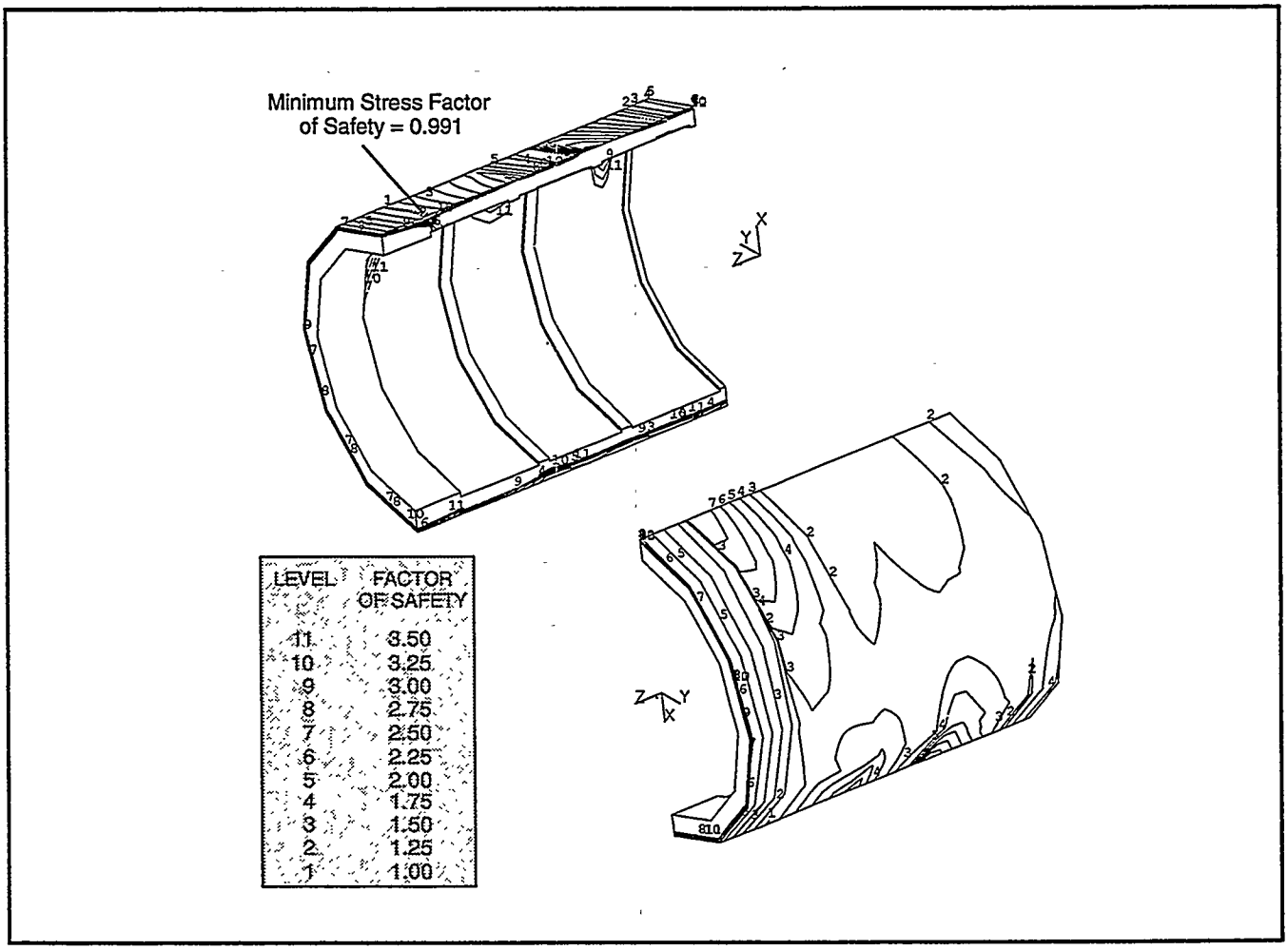

Figure 3-44. Z Stress Factor of Safety Contours, T = 2.67 Secs, Alt = 104 kft Cassini Graphite Impact Shell, -90° Trajectory, 1.9 Secs. Release

GIS Results - Intermediate Trajectory: Thermostructural analysis of the GIS was also conducted for the intermediate (-20°) reentry condition based on a nominal release time from the aeroshell of 5.85 seconds at an altitude of approximately 160 kft. A cross-plot of ablation and temperature data from the REKAP analysis, as well as deceleration load information from the 3DOF trajectory analysis, is presented in Figure 3-45. A total of four timepoints along this trajectory were analyzed in detail, representing critical times in the trajectory for the maximum gradient condition (t = 6.05 secs.), the maximum temperature condition (t = 7.85 secs.), the peak deceleration load condition (t = 8.45 secs.), and a critical ablation condition (t = 10.95 secs.).

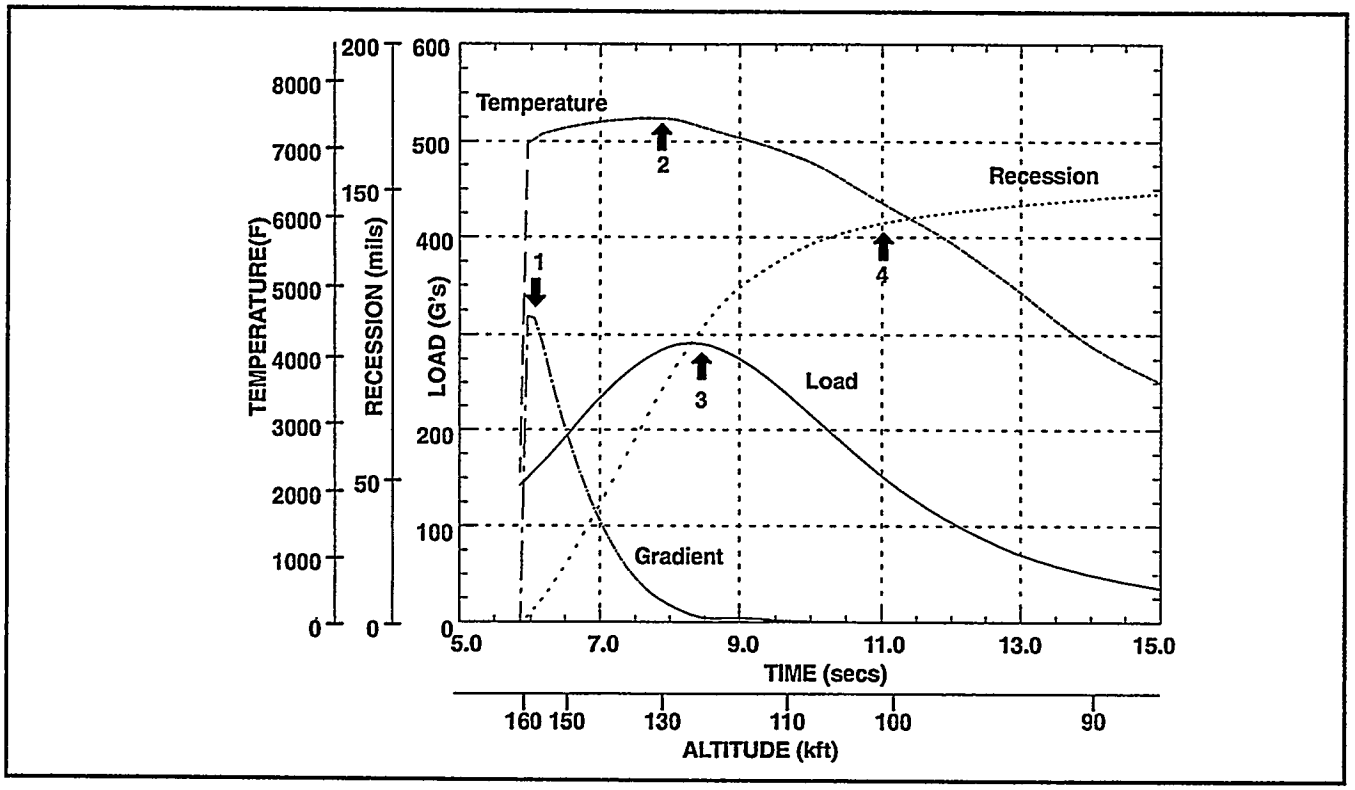

Figure 3-45. Critical Flight Data at Stagnation Point vs. Time - GIS Assembly Intermediate (-20°) Trajectory, Face-On Stable Attitude, 5.85 Sec. Release

Load conditions at the various timepoints are summarized in Table 3-16. The peak GIS temperatures and decelerations are comparable to those predicted for the aeroshell for the intermediate trajectory but are much lower than the maximum values obtained for the GIS from the steep trajectory analysis. Also, due to the longer-duration reentry heating environment, thermal penetration into the GIS is increased such that the gradients for the intermediate trajectory are much lower than those for the steep trajectory at the comparable times of peak deceleration loading. This implies that the entire GIS is at an elevated temperature during the critical loading phase of the intermediate trajectory.

A summary of analysis results for the four baseline cases is presented in Table 3-17. Plots of X factors of safety for both stress and strain are presented in Figure 3-46, while Figure 3-47 illustrates the predicted Z stress and strain factors of safety. Stresses in the X direction produce the minimum factor of safety of 1.26 due to the peak loading condition at t = 8.45 seconds. The comparable strain factor of safety for this condition is 5.04, indicating adequate structural capability in the GIS. The Z stresses and strains result primarily from thermal gradients in the GIS, and minimum factors of safety are obtained for the peak gradient condition at t = 6.05 seconds. As with the steep trajectory analysis, the minimum

Table 3-16. Summary of Load Cases for Cassini GIS Assembly - Intermediate (-20°) Trajectory, 5.85 Sec. Release

	Analysis Time (secs)			
	6.05	7.85	8.45	10.95
Altitude (kft)	156.4	128.5	121.1	101.2
Flight Condition	Maximum Gradient	Maximum Temperature	Maximum Load	Critical Recession
GIS Weight (lbs)	1.12	1.05	1.03	1.00
Accel. Load (G's)	159.6	286.0	293.3	157.6
Stagnation Pt. Data				
Temperature (°F)	7130	7422	7298	6204
Gradient (°F)	4522	330	64	–22
Ablation (in)	0.0044	0.0793	0.1023	0.1378

factors of safety are localized to the exterior surface of the GIS, with much larger factors of safety indicated through the majority of the shell. The minimum factors of safety in stress and strain are 1.33 and 2.33, respectively, again indicating adequate structural capability in the GIS to withstand the reentry loading environment for the nominal intermediate release condition at 160 kft..

Table 3-17. Summary of Stresses and Strains for the Cassini Graphite Impact Shell - (-20°) Face-On-Stable Trajectory, 5.85 Sec. Release

	Analysis Time (secs)			
	6.05	7.85	8.45	10.95
Flight Condition	Maximum Gradient	Maximum Temperature	Maximum Load	Critical Recession
X DIRECTION				
Stress (ksi)	–2.29	–1.47	–1.43	–1.91
Temperature (°F)	6410	7092	7234	6226
Allowable (ksi)	–3.95	–2.22	–1.80	–4.87
Factor of Safety	**1.7292**	**1.511**	**1.256**	**2.553**
Strain (%)	0.11	–0.53	–0.65	–0.24
Temperature (°F)	2608	7092	7234	6226
Allowable (%)	0.35	–3.06	–3.28	–1.78
Factor of Safety	**3.340**	**5.743**	**5.043**	**7.425**
Y DIRECTION				
Stress (ksi)	–2.29	–0.82	–0.75	–1.76
Temperature (°F)	6410	7092	7234	6226
Allowable (ksi)	–3.95	–2.22	–1.80	–4.87
Factor of Safety	**1.728**	**2.729**	**2.400**	**2.764**
Strain (%)	0.10	–0.31	–0.32	–0.22
Temperature (°F)	2608	7092	7234	6226
Allowable (%)	0.35	–3.06	–3.28	–1.78
Factor of Safety	**3.524**	**9.904**	**10.259**	**8.004**
Z DIRECTION				
Stress (ksi)	–2.97	–0.54	–0.55	1.00
Temperature (°F)	6410	7390	7295	6225
Allowable (ksi)	–3.95	–1.33	–1.61	4.88
Factor of Safety	**1.331**	**2.469**	**2.951**	**4.861**
Strain (%)	–0.88	–0.34	0.26	0.14
Temperature (°F)	6410	7390	7248	6225
Allowable (%)	–2.04	–3.53	3.31	1.77
Factor of Safety	**2.334**	**10.511**	**12.543**	**12.768**
SHEAR				
Cap Stress				
Peak X (ksi)	4.39	6.74	6.61	6.19
Peak Z (ksi)	–0.58	7.43	7.94	4.69
Float. Membr. Stress				
Peak X (ksi)	21.60	17.14	19.09	18.55
Peak Z (ksi)	–22.83	5.30	6.32	4.22

Note: Factor of Safety = (Allowable Value)/(Predicted value)

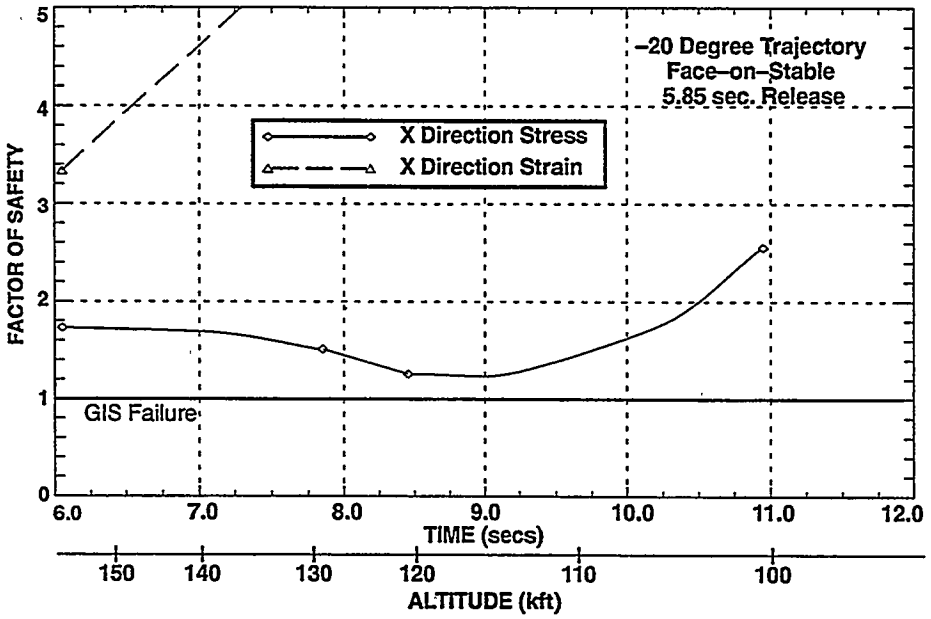

Figure 3-46. Factor of Safety vs. Time - X Direction - Graphite Impact Shell

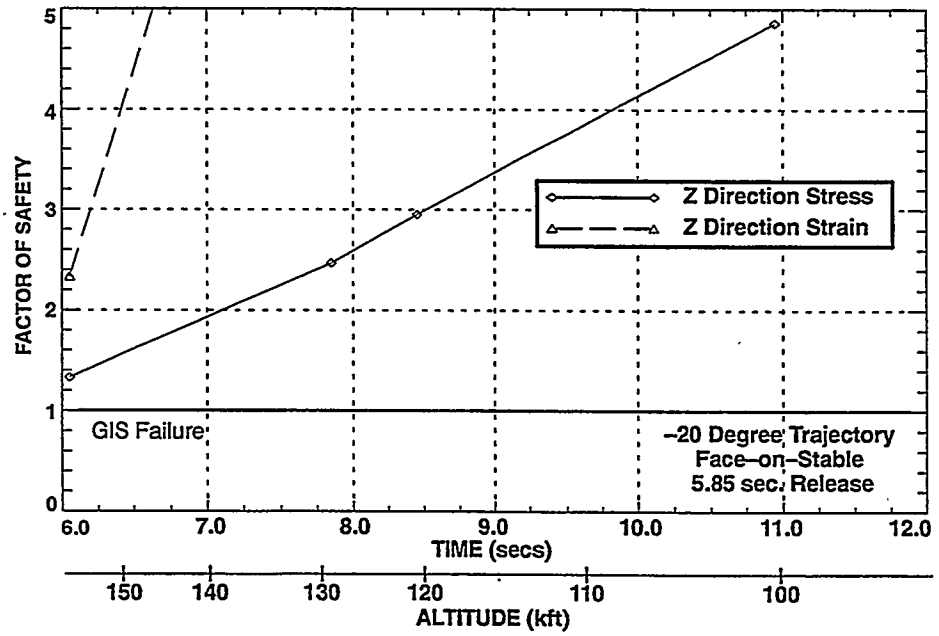

Figure 3-47. Factor of Safety vs. Time - Z Direction - Graphite Impact Shell

Out-of-Orbit Aeroshell Survivability

It has been demonstrated in previous reports that the aeroshell will survive all out-of-orbit accident conditions. For sub-orbital accidents that the recession will vary from 11 mils to 54 mils (6% to 29% of the minimum thickness), while reentries associated with orbital decay accidents will experience a recession of 54 mils. The most severe recession environment is expected to occur for off-nominal accidents that may lead to super-orbital reentry velocities as high as 11 km/s. For these cases the recession may be as great as 68 mils to 130 mils (37% to 71% of the minimum thickness), for super-orbital reentry just above the skip-out bound and multiple reentry skips, respectively. However, it should be pointed out that the accidents that lead to these environments have a low probability of approximately 10^{-8}.

Out-of-Orbit Source Terms

Since the GPHS module will survive the aerothermal environment of reentry only hard surface impacts can produce a fuel release (source term). Predicted source terms have been computed, utilizing the MIM Monte Carlo code, for all out-of-orbit accident cases. In addition a set of 5000 release records from simulated module impacts on hard surfaces has been created for sampling in the SPARRC consequence analysis codes.

EGA Air Release Source Terms

Fuel release particle size and mass distribution data has been computed for postulated Earth gravity assist reentries. If the GIS fails and the fuel elements or fragments are released, they will melt, shedding microsphere droplets through the mechanism of liquid layer stripping. The resultant molten droplets will then begin vaporizing. Much of the basis of this analysis is formed utilizing early studies by L. Gilbert, et al, and later work by M. Eck referenced in the Cassini Environmental Impact Study.

The time dependent thermal environment for the fuel fragments and/or particles is modeled using a three dimensional (three translational equations of motion) trajectory code, 3DMP, that accounts for mass loss and dimensional characteristics of the melting/vaporizing fuel particles and resultant droplets. It is assumed that the fuel initially released from the GIS is already fragmented with initial particle size distributions based on low distortion safety test results.

These fragments/particles are exposed to the hypersonic environment and begin to melt, shedding microsphere droplets which then begin to vaporize. The onset of droplet vaporization is delayed to account for the finite time required to raise the molten droplet from its melt temperature (4635°R) to the vaporization temperature of (8100°R). It is assumed that the microspheres are isothermal as verified by computing the Biot number, N_{bi}.

The liquid layer is formed on the initial fragments, assumed spherical, by the introduction of a convective heat flux, with re-radiation

The melted mass flux is then computed utilizing the average heat flux and the parameter, Q^*, which is a function of the latent heat of fusion and molecular weight. The mass loss rate is then numerically integrated as the fragment continues along its trajectory providing the melted mass distribution.

The above liquid layer is shed and will now undergo breakup to form stable molten droplets. The determination of droplet formation and resultant stable diameter is essentially a balance between the dynamic pressure at the front of the droplet, which causes it to flatten, inflate as a parachute, and finally burst and surface tension and viscosity which tend to retard breakup. The deceleration exerts an inertial force at the rear of the droplet, moving it forward along the sides of the drop which accelerates deformation. The surface tension and viscosity will oppose this deformation force tending to hold the droplet together.

The condition for droplet stability is related through the critical Weber number, which relates the critical droplet diameter to the freestream density and velocity and the droplet surface tension.

Vaporization of the stable liquid droplet is computed as a function of the average heat flux to the surface of the droplet and the parameter, Q^*, where Q^* is now determined using the latent heat of vaporization. As with the melting initial fragments, the stable liquid droplets are modeled as spheres that lose mass and diameter as they vaporize and proceed along their trajectory flight path. The mass loss rate is numerically integrated along the droplet flight path to yield the vapor mass distribution.

For the liquid droplets a delay of the vaporization onset is computed as the time required to isothermally raise the temperature of the droplets from the melt temperature, T_{melt}, to the

vaporization temperature, T_{vapor}. The isothermal assumption is tested by computing the Biot number. For the isothermal assumption to hold the N_{Bi} must be less than 0.1. For the conditions investigated here the Biot number is always less than 0.025, implying that the isothermal assumption is valid.

The mass and particle size distribution has been determined over a range of potential fuel release conditions from the GIS. These release conditions, in general, correspond to given GIS wall recessions from 75% to 85% for -20° and -90° EGA reentry flight path angles.

The two cases most likely representing potential fuel release conditions (including effects of uncertainty and variability) are the 85% recession at -20° flight path angle and the 80% recession at -90° flight path angle. Releases below these two cases result in a thermal environment so benign as to not melt or vaporize the fuel fragments, while recessions above these cases are insufficient to yield a release of fuel.

It has been demonstrated that nearly half of the fuel will remain intact and continue to a surface impact. The remaining half will melt and stabilize into microspheres of 2 to 50 μm diameter. These microspheres will further lose 30% to 60% of their mass to vaporization.

The melting/vaporization process, for a given reentry, occurs within a very narrow band of altitude, between 23 and 25 km for a steep -90° and 30 to 32 km for a -20° reentry. The melt is completed within one to two seconds while the vaporization occurs within 100 to 200 μsec.

Consequence and Risk Analysis

During this period, the principal areas of progress are identified as:

1) Draft FSAR analysis
2) Sensitivity Studies of consequence analysis input parameters
3) Implementation of EGA reentry scenarios analysis

Draft FSAR Analysis

In support of the Nuclear Risk Analysis Document, Volume III of the Draft FSAR, a total of 6438 SPARRC evaluations was performed to predict the nuclear risks associated with from launch accidents scenarios including those leading to out-of-orbit reentries. The analysis was to provide the variability-only results using nominal input data for source term, transport and health effects. Related to the launch accident scenarios, supporting data base include the launch site-specific surface characteristics and land usage, and 150 days of dispersion meteorology conditions. In particular for phase 0 launch accidents, which could occur anytime during two hours before the launch window, the meteorological data required a concatenation of two successive 24-hour data files and an adjustment to the time boundary input of SATRAP. Ground impact analyses of out-of-orbit scenarios used 14 meteorology categories and a worldwide receptor database for 720 equal-area cells with up to 15 population density classes per cell.

The effects of variability from the source term and other transport conditions were evaluated by stratified sampling from the Latin Hypercube Sampling (LHS) code. In order to assure that LHS could sample all significant range of values, the launch accident analysis employed three clusters of source term and ten clusters of dispersion meteorology conditions. The high volume of analysis cases was made possible with the use of multiple workstations on a local network and a shell program designed to process the flow of data, executable codes and results. Consisting of high level UNIX commands and C language programs, this shell program represents the link between LASEP-T outputs, LHS random sampling, and the SPARRC family code. In terms of health effects and land contamination, all analysis results were reported for selected percentile cases and presented in the form of complementary cumulative distribution function (CCDF) curves.

Sensitivity Studies

Several sensitivity studies were performed during this period to justify the basis for key inputs parameters and adopted analysis approach. These sensitivity studies include:

1) Related to the accident scenarios with fireball, a sensitivity analysis was performed for the number of puffs to simulate the plume stem below the mixing height. Because this fraction of plume stem contributes mainly to the consequence results, it is important to know the effects of mass partition and wind shear. Using 1 to 6 puffs configurations and 128 days of meteorology data, test cases were performed. Overall, the analysis showed that a single puff modeled as a uniform column up to the mixing height is adequate because it produced equivalent results when compared with other multiple puff configurations.

2) A variability study for plume rise using the Sandia PUFF code was performed for an average source term and two liquid propellant fireball types representative (Titan core fireball and space vehicle fireball). Variations of final cloud height and cloud diameter with 150 meteorology conditions were examined and compared with previous mission risk analyses values. These results were presented to INSRP and DOE at the 8-9 May 1996 Fireball Model Review Meeting.

3) Sensitivity studies of the SPARRC consequences relative to various type of releases were conducted for developing a mass scaling model approach for the Draft FSAR. Applicable for phase 0 and phase 1 scenarios, the analysis of average source terms through all 150 meteorological conditions was performed at two accident times: 3 am and 7 am. The 3 am results were used in a consequence scaling model to analyze all phase 0 and phase 1 events for all LASEP-T trial outputs. The scaling model indicated that only 4 dominant cases (1.1, 1.3, 0.1, and 0.2) required to be analyzed with full LHS sampling. Note that, in applying the scaling method, specific particle size bins were weighted with mass relative to their corresponding pathway contribution (either inhalation dominant or ingestion dominant) to determine the consequence. The results from this sensitivity study also provided eight maximum and eight minimum consequence days for input to the approach for clustering meteorology conditions.

4) A sensitivity study of the out-of-orbit scenarios consequence results was completed. This study consisted of : (1) changing the fraction of exposed rock to a lower mean value, and (2) using the multinomial distribution function in the combination of various population density classes with breached modules. The first part of the study evaluates the effects of rock fraction on the overall consequence results and the second part gives a better probability evaluation for cases of multiple modules impacting areas with more than one population density class. For the analysis of the Draft FSAR, no credit was taken for the effective exposed rock fraction and the whole rock fraction value of the impacted was used in determining the number of breached modules. Using a fraction of exposed rock (from 70% to 80%) for various rock types, insignificant effects were found for the application of multinomial distribution in the combination of population density classes and breached modules. For case 5.3, although 75,000 combinations were evaluated, changes in probability values only affect the consequence results above the 99th percentile case. In other words, the contribution from cases with one breached module or with one population density class contributed predominantly to the out-of-orbit consequences.

5) A sensitivity study of splitting the 12th bin of the LASEP-T source term files was completed using the average source term for a ground release with no fireball (Type 1), and for a space vehicle fireball release (Type 3). The purpose of this study was to investigate the impact of splitting the 12th bin which ranges from 215 to over 10000 micron into an inhalable bin from 215 to 484 microns and a non-inhalable bin from 484 to 10000 micron. Based on a sensitivity study of the fuel particle size model from LASEP-T, the mass in the current 12th bin can be assigned approximately 15% to the range 215 to 484 micron bin and the remainder to the 484 to 10000 micron bin. The SPARRC analysis with the additional bin, using all 150 meteorology conditions, indicated only a slight difference (about 2%) in health effects. Since this study was only done for two of many possible particle size distributions and possible higher variations could apply, it was decided that future SPARRC runs would include this split for 12th bin and the relative mass fraction set at 15% and 85% for early launch accidents, for low and high particle size bin as defined above.

6) A preliminary analysis of EGA scenarios involving the high altitude release of vaporized fuel was performed. As test cases, the particle size distribution and source term values from the Environmental Impact Statement (EIS) were used to evaluate the range of consequences for small particles (<10 microns) in the shallow and steep reentry cases. For this analysis, the capability of treating multi-particle size was implemented in HIAD. Overall, the consequence results were found in the same range as the EIS results. The effects of injection latitude (equator vs. mid-latitude) is about a factor of 2, and the effects of particle sizes (0.02 micron vs. 10 micron) is about 18. The effects of altitude injection was found to be negligible due to the long half-life of Pu-238.

EGA Analysis Implementation

The approach for variability analysis and variability plus uncertainty analysis for EGA scenarios was defined and implemented. After examining the EGA event tree sequence diagrams (updated in concert with HNUS, OSC, and JHU/APL personnel), it was decided that a definition of end states oriented toward individual modules, rather than conditions of release, is required as the first step of analysis. This definition will allows the status of each GPHS module to be partitioned into groups with potential release of source term in air, and at ground level on rock/soil impact. Based on the EGA event tree, each module during reentry with shallow or steep angle can have one of the following end states:

- End State (A): Intact module with potential release upon rock impact
- End state (B): Failed aeroshell with ``GIS OK Clad OK" failure mode
- End state (C): Failed aeroshell with ``GIS OK- Clad Melt" failure mode
- End state (D): Failed aeroshell and GIS failure during reentry

For end states A and B, impact on rock is the condition for possible release of source term. For end state C, releases occur for impacts on rock, soil, or water. For end state D, release of source term at high altitudes combined with ground impact is considered. Source term characteristics (mass and particle size distribution) are dependent on the aeroshell and GIS end state, and the type of surface impacted.

Using the various branch probabilities in the EGA sequence event tree, the end state probabilities applicable to a single module can be evaluated. To accommodate the variation of these probabilities during uncertainty analysis, an analytical form of each event tree branch is generated and stored in the shell program. The partition of 54 modules into the four end states could be a multitude of combinations. Since each end state has a probability, the combinations can be predicted by the multinomial distribution sampling.

In summary, for each case of analysis, the key input variables for determining impact location and source term characteristics include:

- Latitude band of reentry
- Angle of reentry (shallow of steep)
- Equal-area cell of impact (or longitude of impact)
- Critical angle for aeroshell failure for a face-on-stable (FOS) condition
- Critical angle for aeroshell failure for a non face-on-stable (NFOS) condition
- Weather group, rock and soil fraction applicable to the impacted cell
- Mass and particle distribution of various types of source term

Other Consequence Analysis Activities

Following the DFSAR analysis, which only provided variability-only results, the shell program was reviewed and modified to accommodate additional scenarios (such as EGA scenarios) and for Uncertainty Analysis. The SPARRC codes were also modified to accept sampled parameter values. A list of uncertainty parameters with respective distributions was implemented in the shell program for the LHS code to sample and supply to the SPARRC family code. Data flows and computational steps from source term definition to final consequence results are examined and verified with sample runs.

Uncertainty Analysis

The safety analysis for the Cassini mission is tasked with determining both the naturally occurring variability and the uncertainty in the calculation of possible consequences of accidents involving the mission. Uncertainty in consequence arises from three sources: uncertainty in the probabilities of failure, uncertainty in the source terms (amount and characteristics of fuel release) models, and uncertainties in the consequence models. During the previous six months, procedures for combining these various sources of uncertainty were refined and tested.

Previously, a method for calculation of the uncertainty in consequence resulting from source term modeling and consequence modeling had been developed. Uncertainty due to limited experimental data is quantified in terms of uncertainty distributions for model parameters. Consequence uncertainty is carried out in the following ways:

1) Calculate variability-only source terms with uncertain parameters held at their nominal values. Calculate variability-only consequences from these source terms, using consequence models with their parameters at their nominal values.

2) Calculate variability-plus-uncertainty source terms with variables and parameters simultaneously changing according to their distributions. Calculate variability-plus-uncertainty consequences from the variability-plus-uncertainty source terms, using consequence models with variables and parameters simultaneously changing according to their distributions.

3) Calculate the distribution of an uncertainty multiplier for nominal consequence from the variability-only and the variability-plus-uncertainty consequence.

The procedure described above does not include uncertainty in the probability of failure. A method for combining the uncertainty in the probability of failure with the uncertainty in consequences was developed in this reporting period. This method employs a Monte Carlo simulation which separately treats variability and uncertainty. The inputs to this simulation are the variability-only consequence, the uncertainty multiplier distribution for the consequence, and the uncertainty distribution for the probability of failure. The probabilities of the variability-only consequences values are multiplied by the random numbers distributed according to the uncertainty distribution of the probability of failure. Simultaneously, the consequence values themselves are multiplied by random numbers distributed according to the uncertainty multiplier distribution for that consequence. These results are then double-sorted to construct complementary cumulative distribution functions (CCDFs) of consequence at any desired confidence level.

Preliminary consequence results for out-of-orbit accident case 3.1 were used to test the new procedure. It will be used to calculate CCDFs with confidence levels for the launch, out-of-orbit, and Earth Gravity Assist accident cases for the GPHS-RTG FSAR.

In a related area, improvements were made in the mathematical derivation of the method used to separate uncertainty from variability-only and variability-plus-uncertainty consequences. The derivation of the mathematical connection between the distributions of model variables and parameters and the family of CCDFs at various confidence levels was simplified.

Safety Tests

Test Description

The edge-on fragment safety test was completed on 26 March 1996. Testing was conducted at the Sandia National Laboratory (SNL) Rocket Sled Test Track (Area III) and was coordinated by Los Alamos National Laboratory (LANL) as described in Reference 3-6. The test setup is shown in Figure 3-48. A stack of three simulated GPHS modules was heated in a furnace with an argon atmosphere which was positioned over a simulated section of an RTG. The simulated RTG section was held in place by four rods hanging from a platform which supported the heating furnace and which allowed the rocket sled to pass underneath during the test. A motorized mechanism transferred the heat source stack into the simulated RTG. A 140 second delay allowed the heat source stack temperature to decrease from 1225°C to approximately 1090°C at the time of impact. A continuous flow of argon gas was maintained as a protective atmosphere in the furnace and in the simulated RTG.

The 7075-T6 aluminum plate fragment, 0.16 cm thick by 20.32 cm deep with an unsupported span of 58.42 cm, was mounted in the support arms of the utility sled (reference Figure 3-49). Static pretest alignment involved placing the plate centerline 4.92 cm below the intended impact point. This arrangement compensated for the expected upward displacement of the plate due to plate upward bowing and sled twist as determined in the impact point trials. The rocket sled was propelled by 15 HVAR rockets. The test was designed to have the fragment hit the converter housing edge-on and at a location directly in line with the long axis of the GIS in the center GPHS module (reference Figure 3-50).

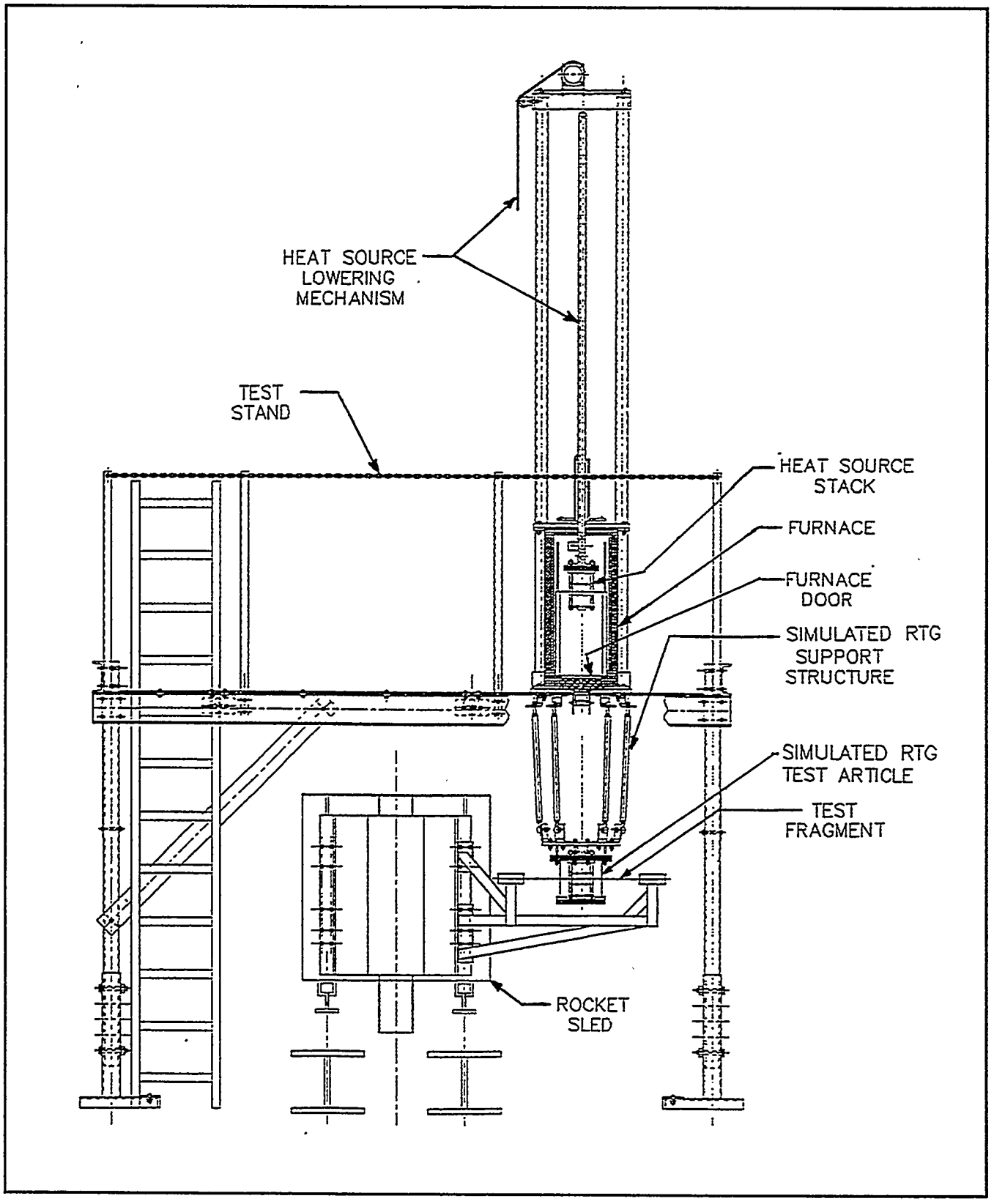

Figure 3-48. Edge-On Fragment Test Setup

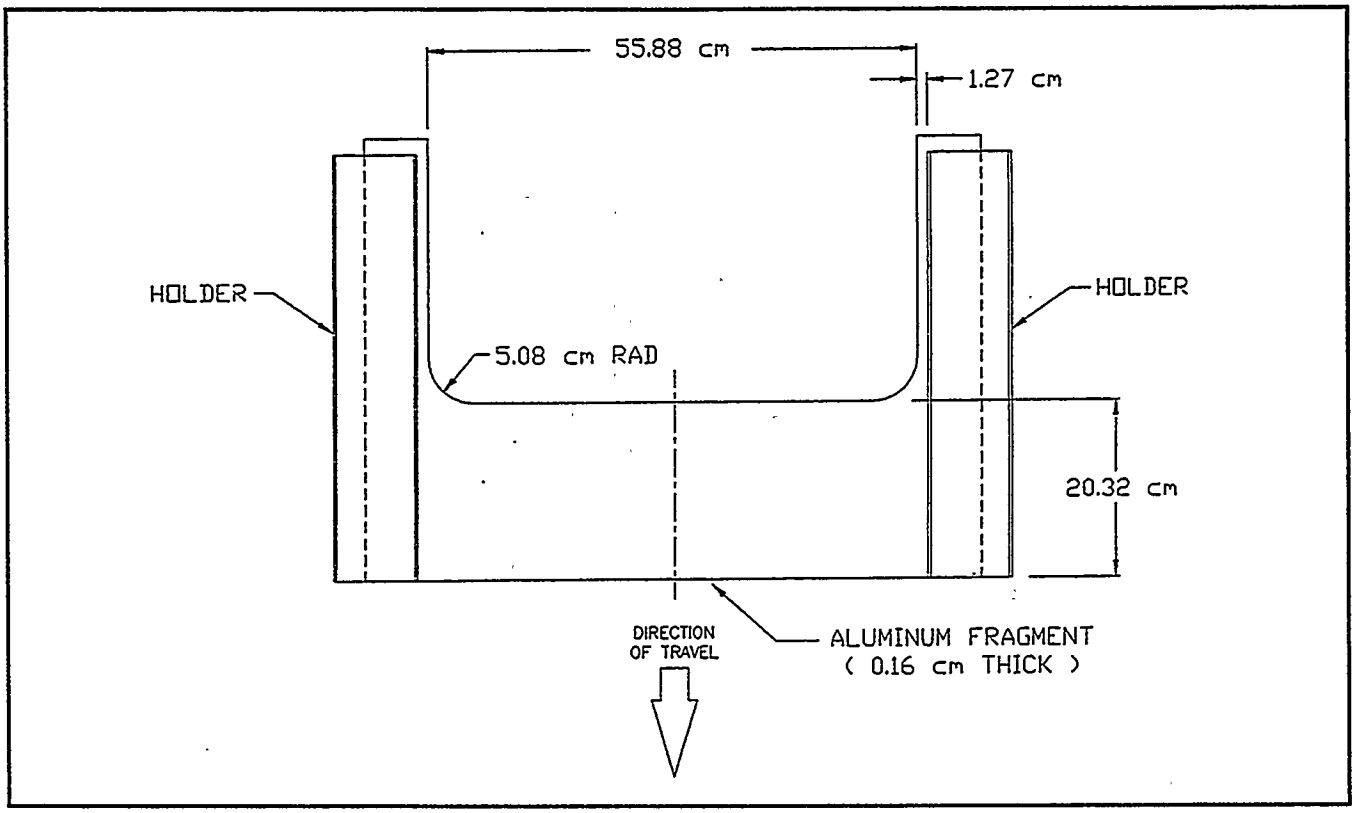

Figure 3-49. Aluminum Fragment Test Configuration

Test Hardware

The simulated RTG test article (RTG-3), shown in Figure 3-51, was prototypical of the RTG design at the point of impact with the aluminum fragment. It consisted of a section of the Al 2219 outer shell, sized to contain three GPHS modules. It contained multifoil insulation around the inner diameter and silicon germanium unicouples were installed in the vicinity of the impact. A graphite heat source support plate was located in the base of the RTG to ensure proper heat source alignment. A purge line was provided at the base of the simulated RTG to provide an inert cover gas (argon) after heat source loading to minimize oxidation. The simulated RTG test article was open at the top end after the heat source stack was installed; the bottom end was closed using an end plate as shown in Figure 3-51.

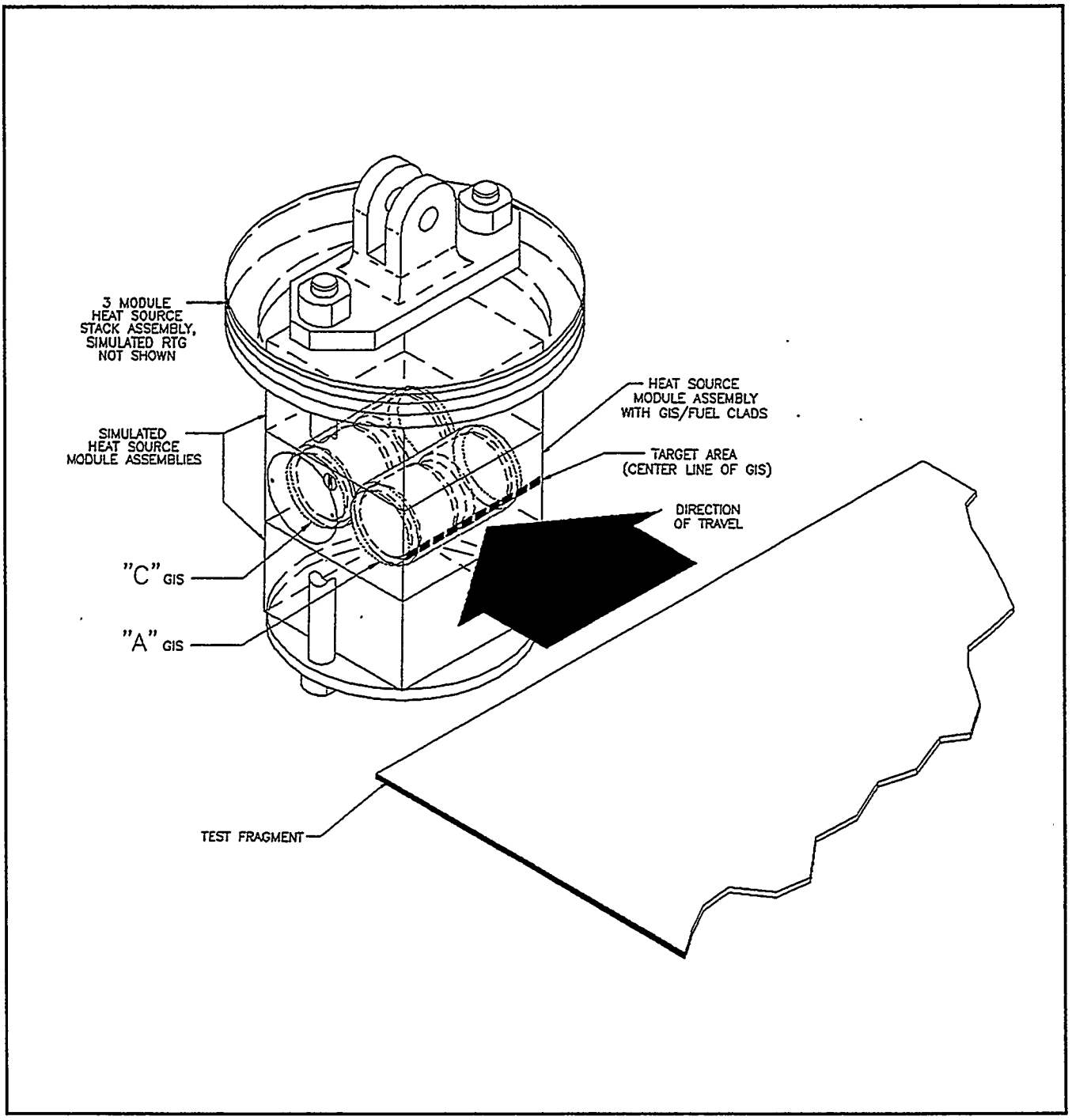

Figure 3-50. Heat Source/Fragment Impact Orientation

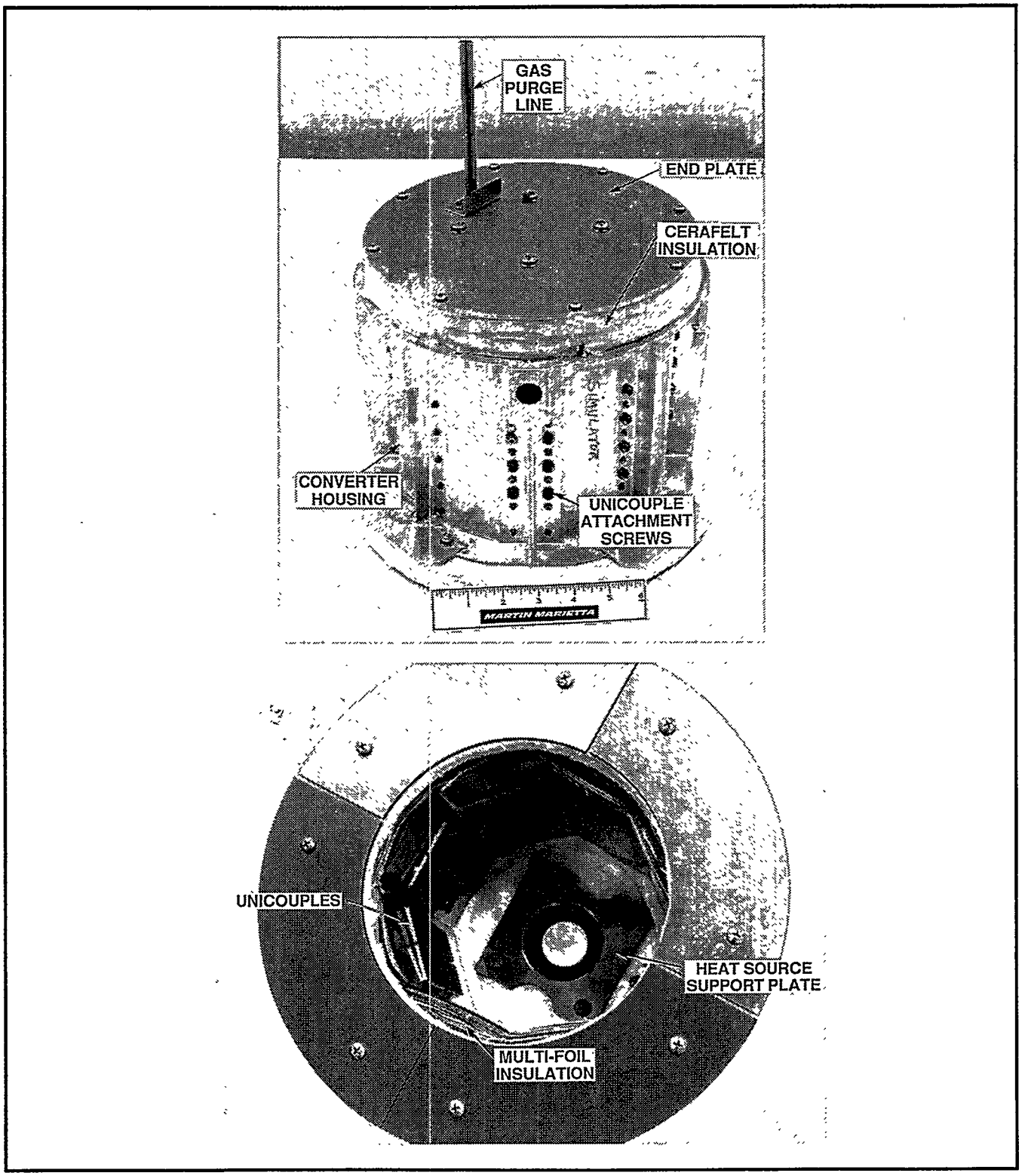

Figure 3-51. Simulated RTG Test Article (RTG-3) – Edge-On Fragment Impact Test

The design of the heat source stack is shown in Figure 3-52. The heat source test hardware was fabricated by Los Alamos National Laboratory (LANL). The heat source stack consisted of a GPHS module with flight quality graphite components and four flight quality iridium clads containing urania fuel simulant. A simulated module (POCO™ graphite aeroshell with molybdenum mass simulants) was located above and below the GPHS module to provide the correct mass simulation. The three modules were stacked using FWPF lock numbers and the modules held in place with POCO™ tie rods, as shown in Figure 3-52. A POCO™ end plate, located at the base of the stack, was used to locate the heat source in the RTG.

Test Results

The test results presented herein were obtained from Reference 3-6. The edge-on fragment test was conducted on 26 March 1996. The measured impact velocity was 306 ± 1.5 m/s as measured from the image motion camera. The heat source impact temperature was estimated to be 1090°C ± 10°C based on previous engineering cool-down tests.

High-speed photography of the impact indicated that the fragment leading edge impacted the converter approximately 0.63 cm above its midpoint. The fragment penetrated the converter shell to the depth of the fuel modules. The converter was cut and torn over approximately 80% of its circumference (Figure 3-53). The width of the gap was approximately 2 cm. The cut was clean at its upper edge but the lower edge was folded over, toward the inside of the shell. Radiological surveys of the converter outer surface and the impact vicinity conducted immediately following the impact indicated that no urania was released outside of the converter.

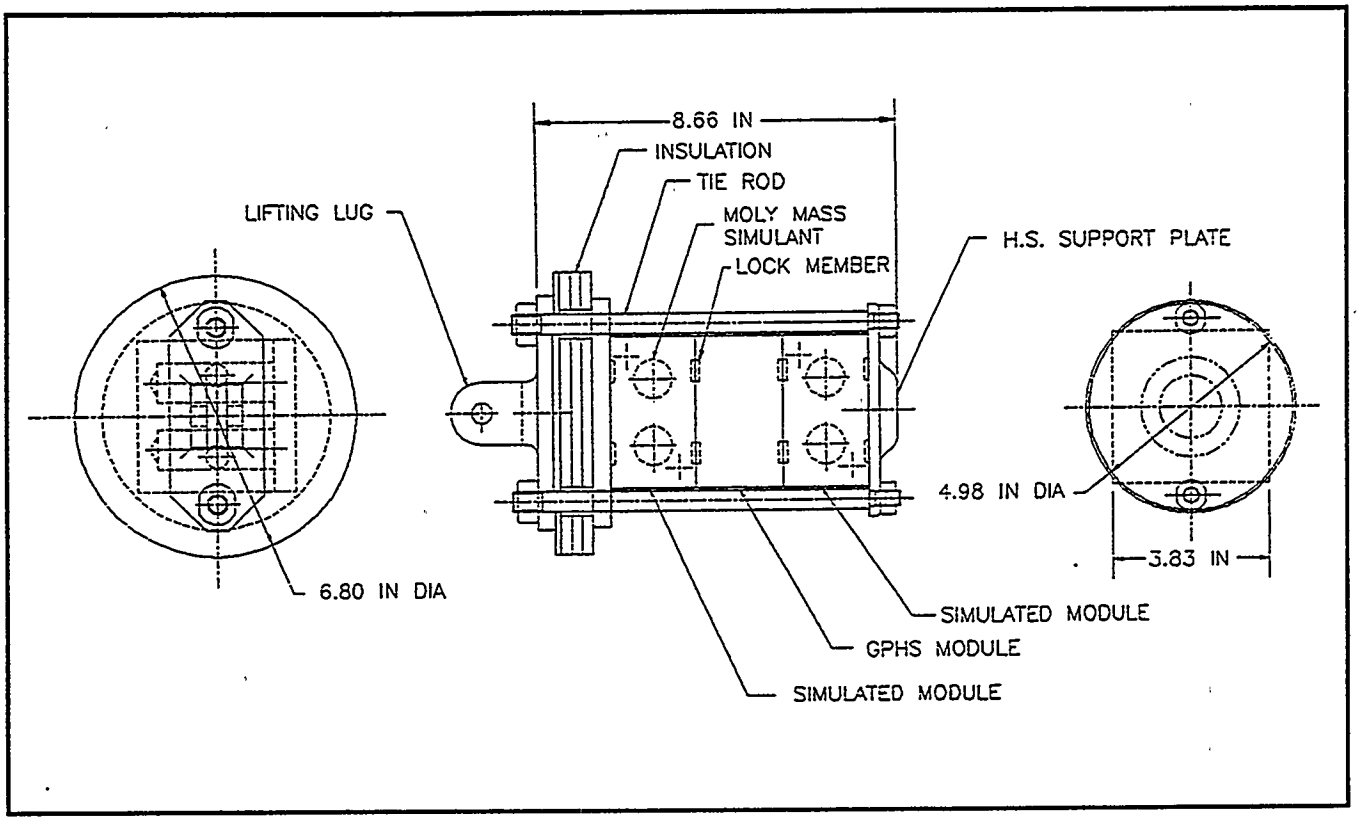

Figure 3-52. Heat Source Configuration for Edge-On Fragment Impact Test

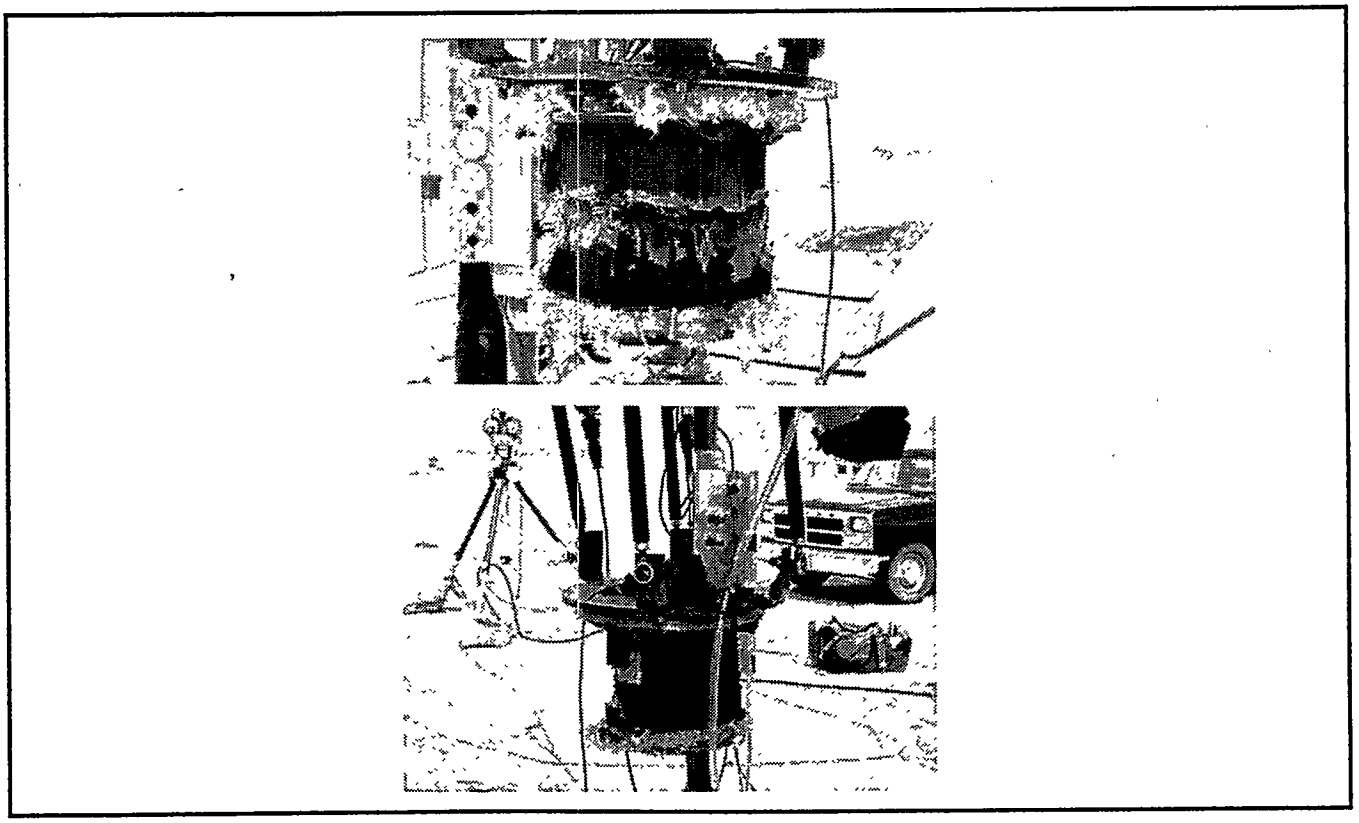

Figure 3-53. Simulated RTG after Fragment Impact Test

The top of the converter housing showed indications that materials within the housing were ejected through the top opening. One of the POCO™ graphite modules was ejected out of the top of the converter and was found lying a few feet from the converter. Lying directly next to the ejected module was a molybdenum mass simulant that was expelled from the ejected module. The other molybdenum simulant was also ejected and located within a couple of feet of the module. The POCO™ module was intact, but chipped. Preliminary field observations revealed no cracks. Other pieces of graphite were also observed in the impact area and appeared to have originated from the top part of the graphite stack. A few pieces of FWPF graphite were also found.

A relatively large area of the fragment was torn off from the sled. This area, roughly trapezoidal in shape, measured approximately 23 cm at the leading edge and 39 cm at the trailing edge. This area was not recovered in one piece, but represented the sum of several relatively small fragments. Most of these fragments were scattered outside of the converter housing, but a few fragments were seen inside the converter during preliminary investigation.

Post-mortem examination of the test components began at Los Alamos on 4 April 1996. All graphite and aluminum fragment pieces that were recovered at the test site outside of the converter were gathered together and photographed. Graphite recovered outside the converter consisted primarily of graphite components located at the top of the graphite stack including the stack lifting lug and the top POCO™ module. Graphite recovered from inside the converter consisted of the bottom POCO™ module, bottom support pieces and the FWPF module. One molybdenum mass simulant was totally dislodged from the bottom module; the other was partially dislodged. The aluminum plate fragments recovered outside the converter were severely deformed as were the fragments recovered from the converter interior. Approximately 3/4 of the fragments recovered from the converter interior had locally melted and resolidified.

Post-test disassembly of the converter revealed that the fragment penetrated into the A GIS cavity of the FWPF module. One corner of the module, at the GIS cavity, was sheared off. The graphite module cap of this cavity was dislodged and had a gash that was apparently caused by penetration of the aluminum fragment. The A GIS was ejected from the module. One half of the GIS end cap had been severed from the GIS; the other half remained in

place. A relatively large piece of the GIS at the impact area (approximately one quarter of the top end) had been sheared off. Neither clad had been dislodged from the GIS. The open end clad (SC0126) was breached on its shield cup (Figure 3-54). Further disassembly revealed no other breaches in the remaining clad in the A GIS, i.e., SC0125. The C GIS was unbreached and totally intact The two fueled clads in the C GIS, SC0127 (vent cup 3130) and SC0128 (vent cup 3132) were also unaffected.

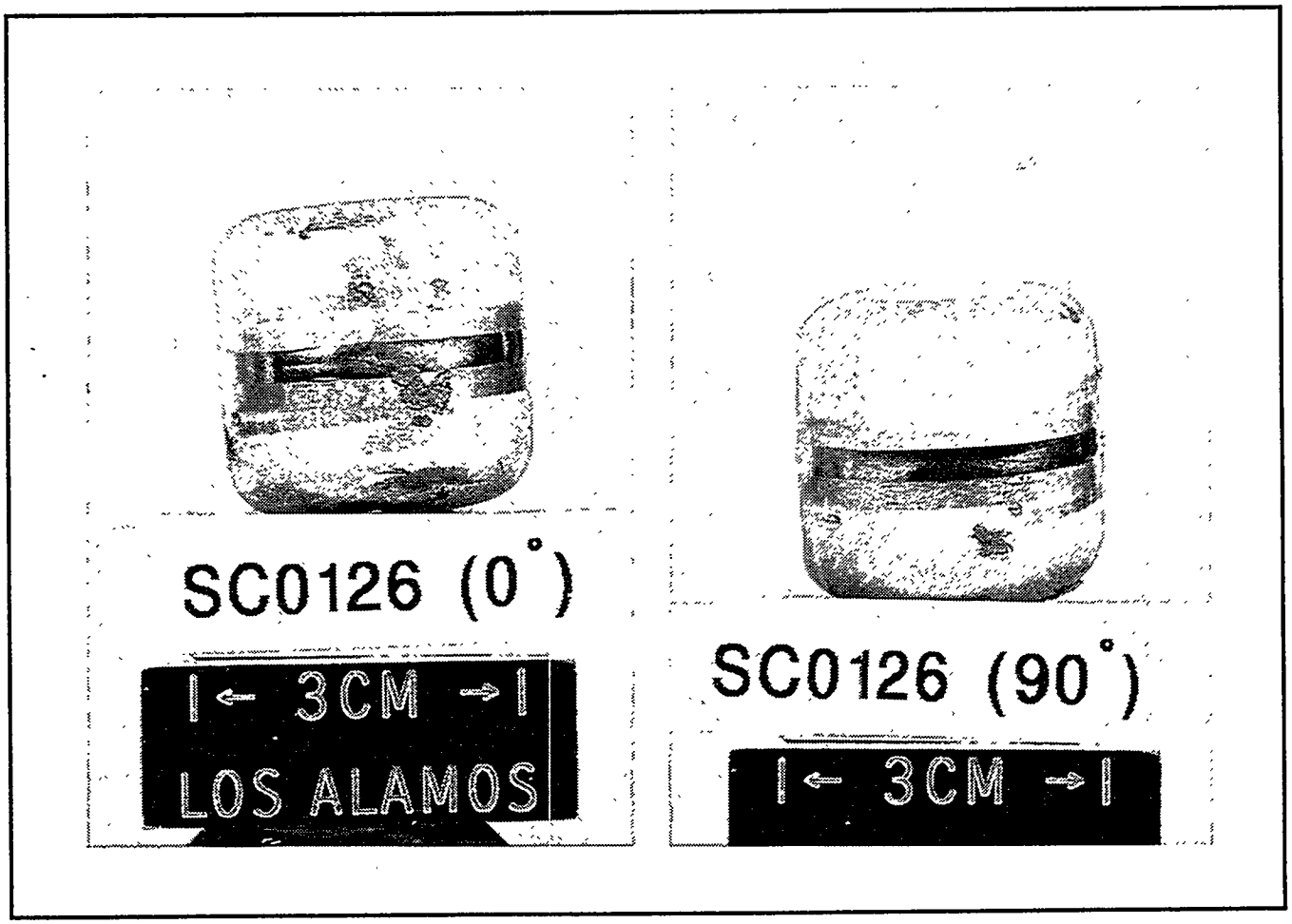

Figure 3-54. Fueled Clad SC0126 (A GIS) after Fragment Impact Test

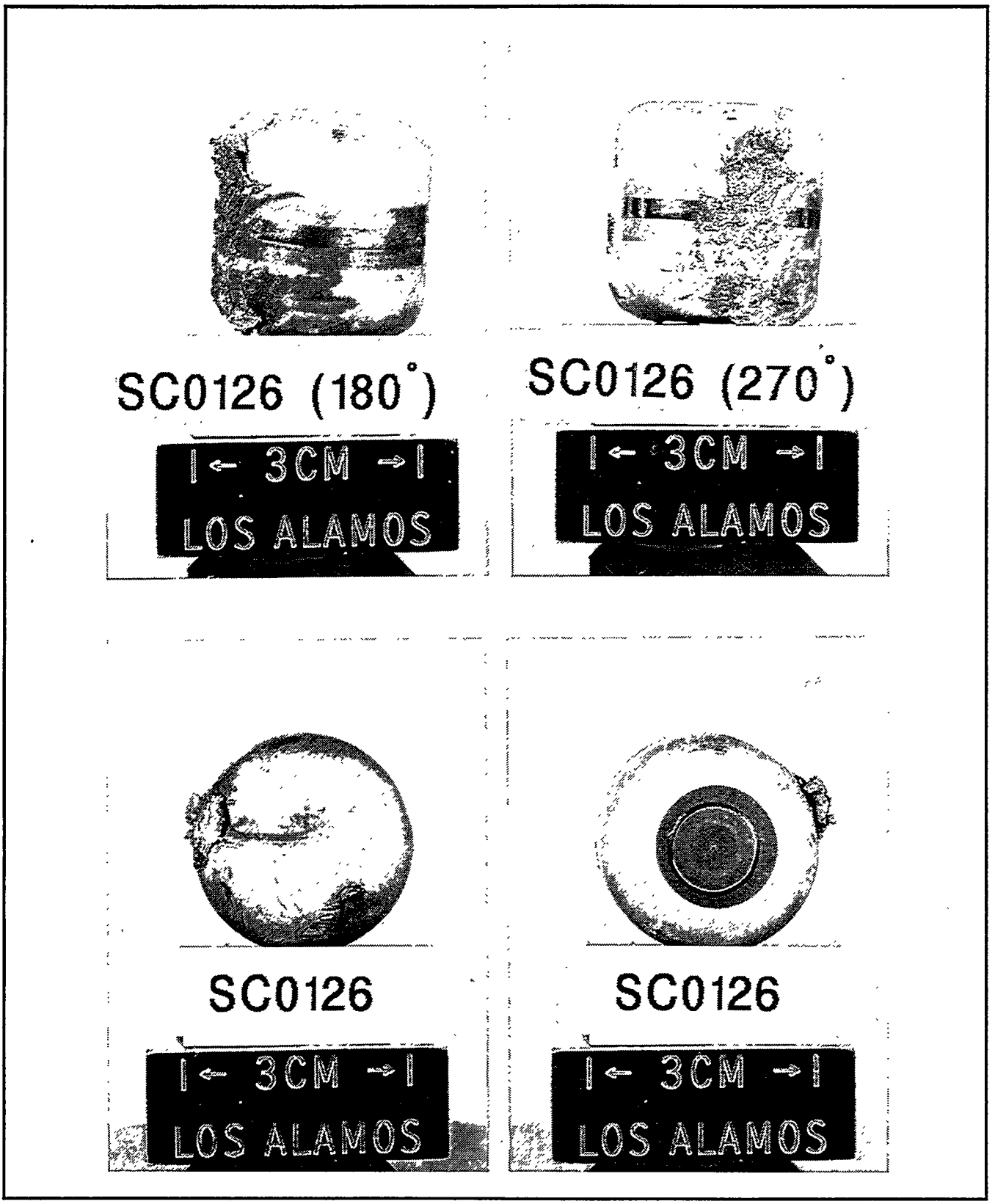

Figure 3-54. Fueled Clad SC0126 (A GIS) after Fragment Impact Test (Cont'd)

The post test dimensional inspection data for the four fueled clads are shown in Table 3-18.

Table 3-18. Fueled Clad Strain after Edge-On Fragment Test

GPHS	Axial	Strain %			
		Vent Cup, Diametral		Shield Cup, Diametral	
		Max.	Min.	Max.	Min.
SC0125	0.5539	0.5044	-1.1432	0.7734	-1.1769
SC0126	3.8102	0.7066	-1.2113	1.3786	-1.1769
SC0127	0.5682	-0.5027	-0.9383	-0.1345	-0.2017
SC0128	0.7019	-0.2690	-1.0424	-0.3693	-0.8392

Capsule SC0126, which was located at the open end of the A GIS, had a small transverse breach (1.84 mm long, 0.40 mm wide) that was apparently caused by impact with the plate fragment. This breach was located between approximately 200 to 220 degrees on the shield cup radius. Material which appeared to be an Al/Ir reaction product surrounded the breach. This material was also observed on the capsule in several locations. Upon further investigation, this single breach actually consisted of two separate breaches. One was a circle-shaped breach that measured approximately 2.1 mm in diameter (3.41 mm^2 breach area). The other breach measured approximately 3.68 mm long and 0.56 mm at its widest point (approximately 2.06 mm^2 breach area). Two other transverse hairline cracks were observed on the shield cup. One crack measured approximately 7.92 mm long and was located below the weld at approximately 115 degrees from the weld start. The other crack was located at approximately 350 degrees, on the cup radius, and measured approximately 3.58 mm. An atypical discoloration of the clad material was observed approximately 130 degrees from the weld start. The estimated amount of fuel released from the capsule was 0.0890 g, based on the weight of the recovered fuel retained by the capsule.

Because SCO126 was the most severely deformed, it was selected for metallographic analysis. It was defueled and the fuel submitted for particle size analysis. The fuel particle size analysis is provided in Table 3-19. Twelve sections were cut from SC0126 and submitted for metallographic examination. The microstructure of the single-pass weld region was typical of the microstructure usually observed in this area. The microstructure of the weld overlap region was somewhat atypical with some thinning of the weld center-line cross section. It exhibited a relatively wide heat-affected zone and a very coarse microstructure. The grain size in the single-pass weld area averaged 12.0 grains/wall thickness and the grain size in the weld overlap area averaged 8.5 grains/wall thickness.

Table 3-19. Particle Size Analysis of Fuel Retained in Fueled Clad SC0126 after Edge-On Fragment Test

Particle Size Range (μm)	Weight Fraction of Retained Fuel *
+5600	0.8533
+2000 to 5600	0.0983
+850 to 2000	0.0354
+425 to 850	0.0072
+180 to 425	0.0031
+125 to 180	0.0010
+75 to 125	0.0006
+45 to 75	0.0005
+30 to 45	0.0000
+20 to 30	0.0001
+10 to 20	0.0002
+9 to 10	0.0000
+8 to 9	0.0000
+7 to 8	0.0000
+6 to 7	0.0000
+5 to 6	0.0000
+4 to 5	0.0001
+3 to 4	0.0002
+2 to 3	0.0000
+1 to 2	0.0000
<1	0.0000
Total	1.0000

* Approximately 0.0890 g fuel released.

The microstructures of the vent and shield cup walls were typical. The grain sizes in these areas are shown in Table 3-20.

Table 3-20. Vent Shield Cup Microstructure, SC0126

Area/Orientation	Grain Size, grains/wall thickness(2)	Grain Size, μm/grain
Shield Cup/Axial	26.1	24.9
Shield Cup/Transverse	25.0	26.0
Vent Cup/Axial	27.4	23.7
Vent Cup/Transverse	25.9	25.1

(2) Grains/nominal wall thickness of 0.65 mm.

Metallographic examinations of the observed Al/Ir reaction product showed it to be clearly defined and appeared to be homogeneous. The intermetallic compound had several fractures indicating that it was a fairly brittle material. One of the intermetallic metallographic sections was submitted for SEM/EDS examination. The examination confirmed the presence of an Al/Ir reaction product having an Al:Ir atomic ratio of 7:3.

Examination of the two transverse shield cup breaches revealed intergranular failure. The fracture ends also exhibited wall thinning and grain alignment. There was a minute deposit of the Al/Ir intermetallic product in both fracture sites. Metallographic examination of the discolored area of the clad revealed no unusual microstructure.

References for Task 3:

3-1 PIR U-Cassini-018, "Background and Use of SINRAP Code" - 29 May 1996.

3-2 PIR U-Cassini-132, "Verification of SINRAP Revision C Changes" - 29 May 1996.

3-3 PIR U-Cassini-133, "CONVERT and CORRECT Programs for Creating CFD Data Input Tables to SINRAP" - 29 May 1996.

3-4 Vacek, D. J., "Nonlinear Thermostructural Reentry Analysis of the Cassini Aeroshell: 90 Degree (Steep) Reentry Flight Path Angle," Lockheed Martin PIR # U-1VC4-Cassini-134, 04-10-96.

3-5 Vacek, D. J., "Nonlinear Thermostructural Reentry Analysis of the Cassini GPHS Aeroshell: 20 Degree (Intermediate) Reentry Flight Path Angle," Lockheed Martin PIR # U-1VC4-Cassini-140, 10-04-96.

3-6 Reimus, M. A., and Hinckley, J. E., "General-Purpose Heat Source Research and Development Program: Radioisotope Thermoelectric Generator Fragment Impact Tests," LANL TBD (draft - final report to be issued).

3-7 Reimus, M. A., and George, T. G., "General-Purpose Heat Source Research and Development Program: Cold-Process Verification Test Series," Los Alamos National Laboratory report LA-13118, June 1996.

Task 4

Qualified Unicouple Fabrication

TASK 4 QUALIFIED UNICOUPLE FABRICATION

The remaining efforts in Task 4 are associated with testing of 18 couple modules. Test temperatures and life test hours are shown in Table 4-1.

Table 4-1. Test Temperatures and Life Test Hours

Module	Unicouple Source	Test Temperature Hot Shoe	Status as of 25 August 1996
18-10	Early Qualification Lot	1135°C	10,400 Hours Performance Normal Test Terminated October 1994
18-11	Full Qualification Lot	1135°C	22,672 Hours Performance Normal
18-12	Early Flight Production Lot	1035°C	18,489 Hours Performance Normal

18 Couple Module Testing

Two modules remain on life test. Testing of module 18-10 was terminated at the end of October 1994 after 10,400 hours.

Module 18-11 has has now been operating for 2.6 years of accelerated life test conditions. It continues to provide added confidence that normal unicouple performance can be expected from the flight RTGs during the Cassini mission.

Module 18-12 has been operating for 2.1 years at normal temperature levels and continues to show normal performance. Both modules continued without interruption during this reporting period.

Module 18-11 (1135°C)

On 29 September 1996 the module reached 22,672 hours at the accelerated hot shoe temperature of 1135°C. Measured performance during this period continues to fall within the data base established by MHW and GPHS 18 couple modules.

The thermoelectric performance evaluation primarily studies the trends of the internal resistance and power factor. Figures 4-1 and 4-2 show these trends in comparison to module 18-8, the last module built during the GPHS program. Agreement is excellent and provides a high degree of confidence that the GPHS unicouple manufacturing processes have been successfully replicated. Table 4-2 summarizes the initial and 22,672 hour performance data.

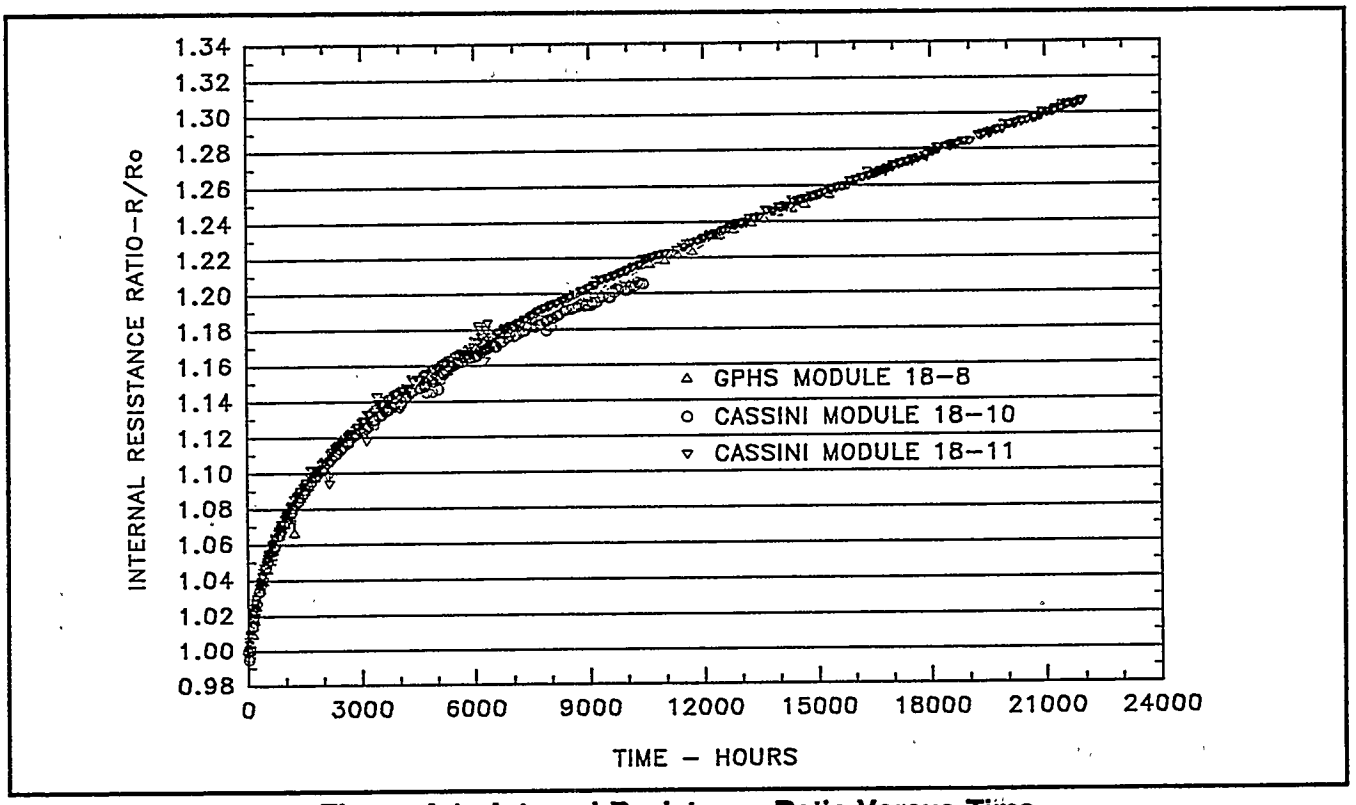

Figure 4-1. Internal Resistance Ratio Versus Time (Modules 18-10, 18-11, GPHS Module 18-8) – 1135°C Operation

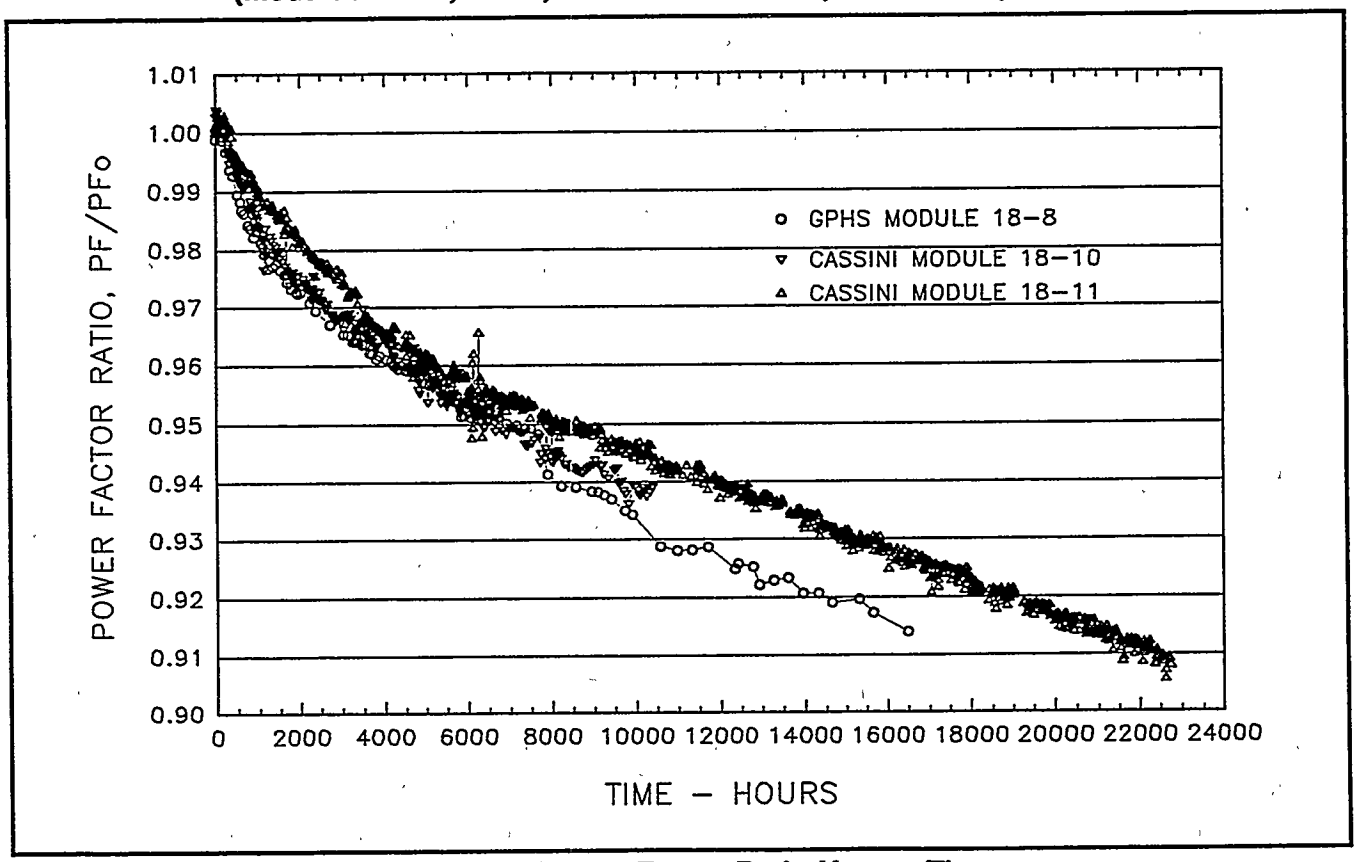

Figure 4-2. Power Factor Ratio Versus Time (Modules 18-10, 18-11, GPHS Module 18-8) – 1135°C Operation

Table 4-2. Comparison of Initial and 22,672 Hour Performance of Module 18-11 at 1135°C

	Initial 2/2/94	t = 52 Hours V_L = 3.5V 2/4/94	t = 22,672 Hours 9/29/96
Heat Input, Watts	190	192.9	193.2
Hot Shoe, °C Average	1137.8	1137.5	1103.4
Hot Shoe Range, °C	5.4	5.2	9.7
Cold Strap, °C Average (8 T/Cs)	311.9	314.3	305.3
Cold Strap Range (8T/Cs)	2.6	2.5	2.1
Cold Strap Average (12 T/Cs)	306.5	308.9	300.3
Cold Strap Range (12 T/Cs)	20.1	20.3	18.3
Load Voltage, Volts	3.895	3.499	3.498
Link Voltage, Volts	0.108	0.121	0.094
Current, Amps	2.842	3.174	2.712
Open Circuit Voltage, Volts	7.140	7.160	7.520
Normalized Open Circuits (8T/Cs)	6.319	6.359	6.898
Normalized Open Circuits (12 T/Cs)	6.276	6.316	6.854
Average Couple Seebeck Coefficient (12)	498×10^{-6}	501×10^{-6}	544.0×10^{-6}
Internal Resistance, Ohms	1.104	1.115	1.448
Internal Resistance Per Couple (Avg.)	0.0613	0.0620	0.0805
Power Measured, Watts (Load + Link)	11.375	11.492	9.74
Power Normalized, Watts (8 T/Cs)	8.909	9.065	8.20
Power Normalized, Watts (12 T/Cs)	8.789	8.942	8.09
Power Factor	40.452×10^{-5}	40.557×10^{-5}	36.78×10^{-5}
Isolation			
Circuit to Foil, Volts	-1.68	-1.36	-1.71
Circuit to Foil, Ohms	6.29K	5.95K	0.374K

The isolation resistance trend between the thermoelectric circuit and the foil is shown in Figure 4-3 along with modules from the MHW and GPHS programs. The isolation resistance plateaued at about 1000 ohms between 6,000 and 7,000 hours. It then started a slow decrease and is presently at 374 ohms. A similar plateau and gradual decline were observed in MHW module SN-1. At the accelerated temperature of 1135°C the same amount of sublimation occurs in about 1,650 hours of testing as would occur in a 16-year Cassini mission.

Consequently, approximately 13.7 times as much sublimation has occurred during the test duration of module 18-11 as will occur during the Cassini mission. The module performance, therefore, confirms the adequacy of the silicon nitride coating on the qualification unicouples.

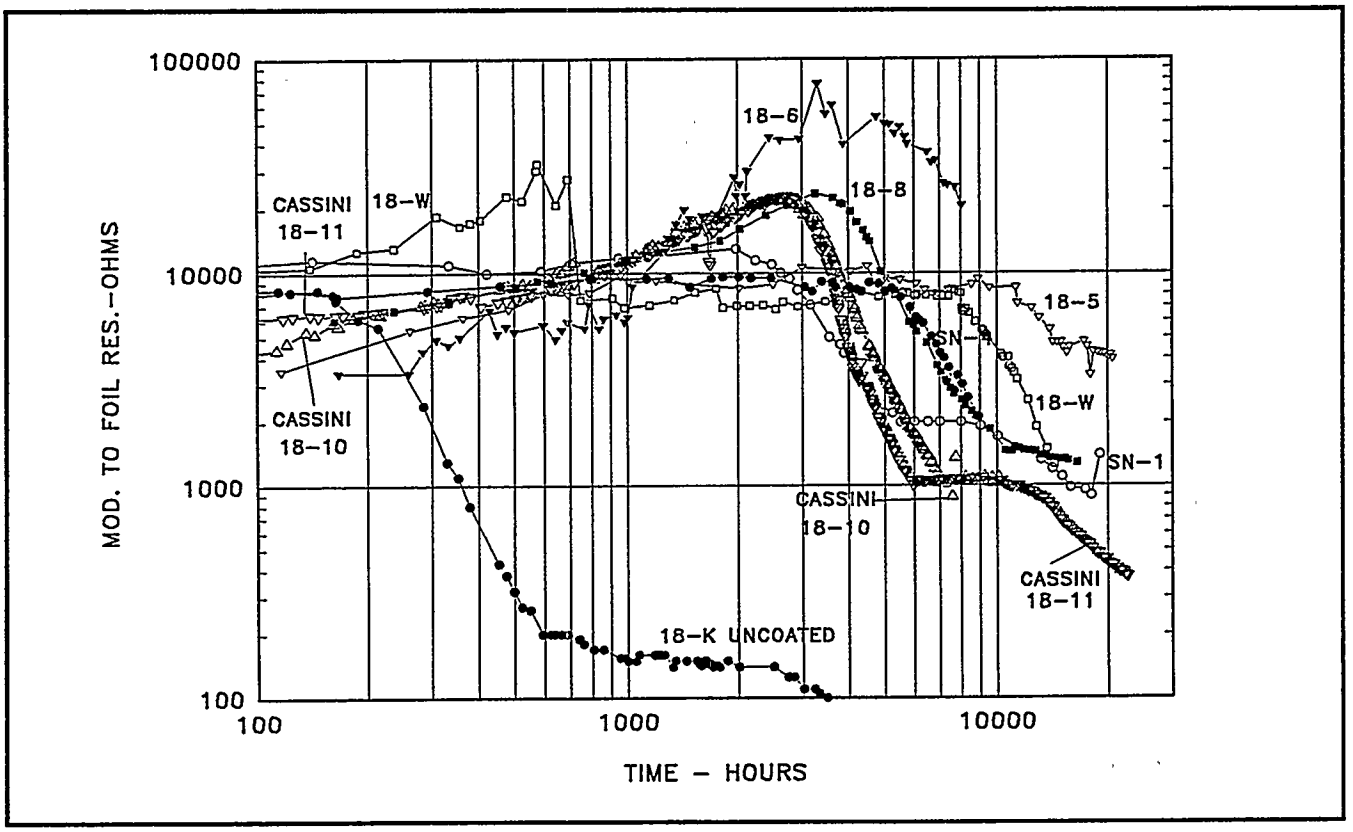

Figure 4-3. Isolation Resistance – Module Circuit to Foil (Modules 18-10, 18-11, GPHS Module 18-8) – 1135°C Operation

Individual Unicouple Performance:

The performance of individual unicouples and rows of unicouples continues to be observed. Table 4-3 shows the room temperature resistance changes and the internal resistance changes observed during operation for each of the six rows and for individual unicouples in Rows 2 and 5. The unicouples continue to perform within a narrow band.

Module 18-12 (1035°C Operation)

The module reached 18,489 hours at the normal operating temperature of 1035°C on 29 September 1996 . Thermoelectric performance, as measured by internal resistance and power factor trends, continues to be normal as shown as Figures 4-4 and 4-5, respectively. Table 4-4 shows initial performance and the performance on 29 September 1996.

Isolation Resistance

The isolation resistance between the circuit and foil continues to show the normal trend as shown in Figure 4-6.

Individual Unicouple Performance

A review of the unicouple internal resistances and open circuit voltages indicates that all unicouples are exhibiting very similar behavior with time (See Table 4-5). The data for the six individually instrumented unicouples in Rows 2 and 5 are shown in Figure 4-7.

Table 4-3. Module 18-11 Internal Resistance Changes

Position	Serial #	2nd Bond Milliohm	Preassy Milliohm	Delta ri Milliohm	T = 0 Milliohm	T=1,509 Hours	Delta ri Milliohm	Percent Increase	T=22,672 Hours	Delta ri Milliohm	Percent Increase
1.0	H2006	22.50	22.10	-0.40							
2.0	H0507	22.40	21.90	-0.50							
3.0	H0512	22.7	22.20	-0.50							
					182.30	199.70	17.40	9.54	240.00	57.70	31.65
4.0	H0439	23.20	22.70	-0.50	62.30	67.90	5.60	8.99	81.40	19.10	30.66
5.0	H0587	22.50	22.40	-0.10	61.00	66.50	5.50	9.02	79.10	18.10	29.67
6.0	H0657	22.70	22.50	-0.20	61.40	67.30	5.90	9.61	80.50	19.10	31.11
					184.10	201.10	17.00	9.23	240.20	56.10	30.47
7.0	H0585	22.90	22.50	-0.40							
8.0	H0459	22.50	22.10	-0.40							
9.0	H0562	22.70	22.30	-0.40							
					185.70	203.20	17.50	9.42	245.70	60.00	32.31
10.0	H0248	22.70	22.30	-0.40							
11.0	H0163	22.90	22.40	-0.50							
12.0	H0282	22.70	22.40	-0.30							
					184.90	201.70	16.80	9.09	240.50	55.60	30.07
13.0	H0428	23.10	22.70	-0.40	62.10	67.90	5.80	9.34	81.10	19.00	30.60
14.0	H0326	22.60	22.00	-0.60	62.20	68.30	6.10	9.81	82.50	20.30	32.64
15.0	H0232	22.60	22.00	-0.60	60.90	66.60	5.70	9.36	81.20	20.30	33.33
					184.70	202.30	17.60	9.53	244.10	59.40	32.16
16.0	H0590	22.60	22.40	-0.20							
17.0	H0393	22.60	22.10	-0.50							
18.0	H0496	22.50	22.30	-0.20							
					184.20	201.40	17.20	9.34	239.90	55.70	30.24

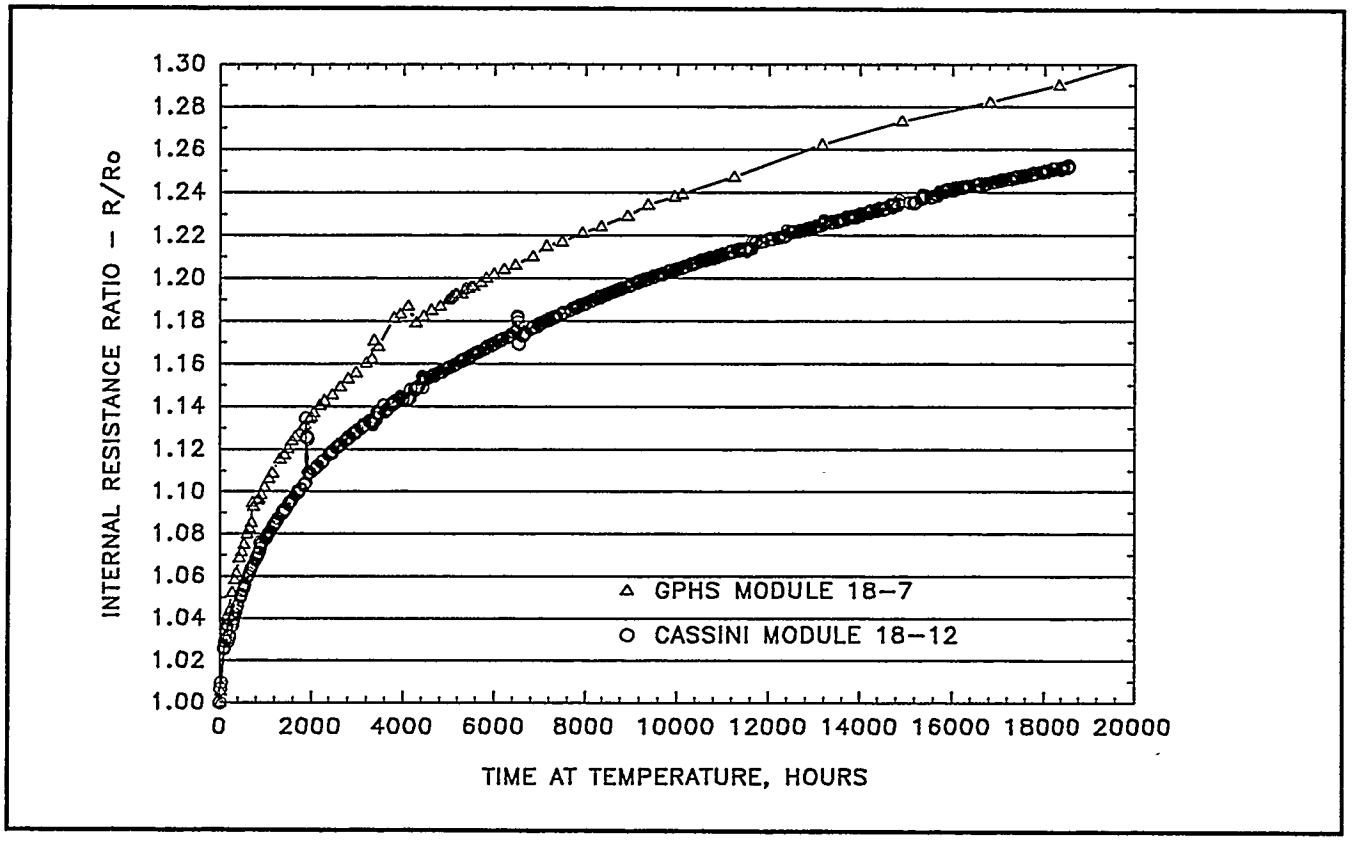

Figure 4-4. Internal Resistance Ratio Versus Time (Modules 18-12, and 18-7) – 1035°C Operation

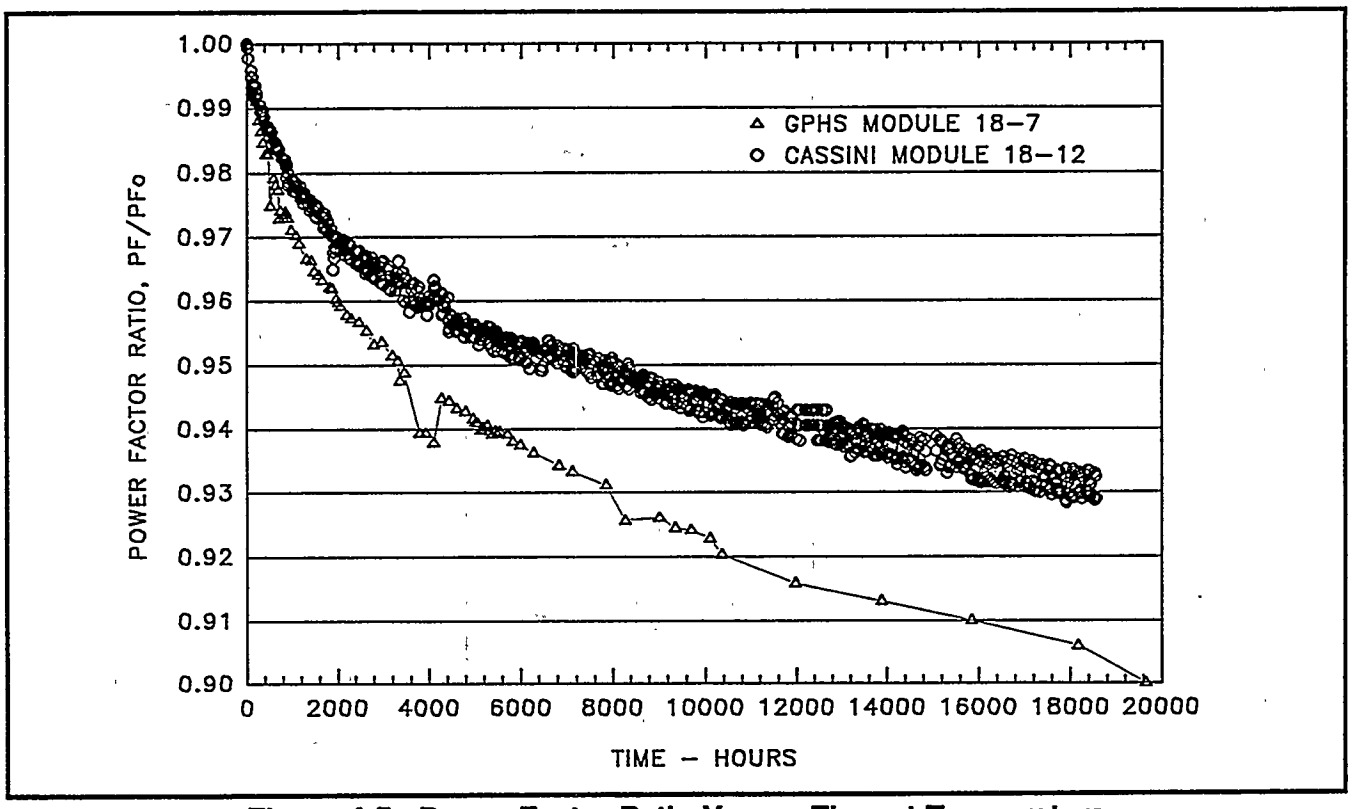

Figure 4-5. Power Factor Ratio Versus Time at Temperature (18-7 and 18-12) – 1035°C Operation

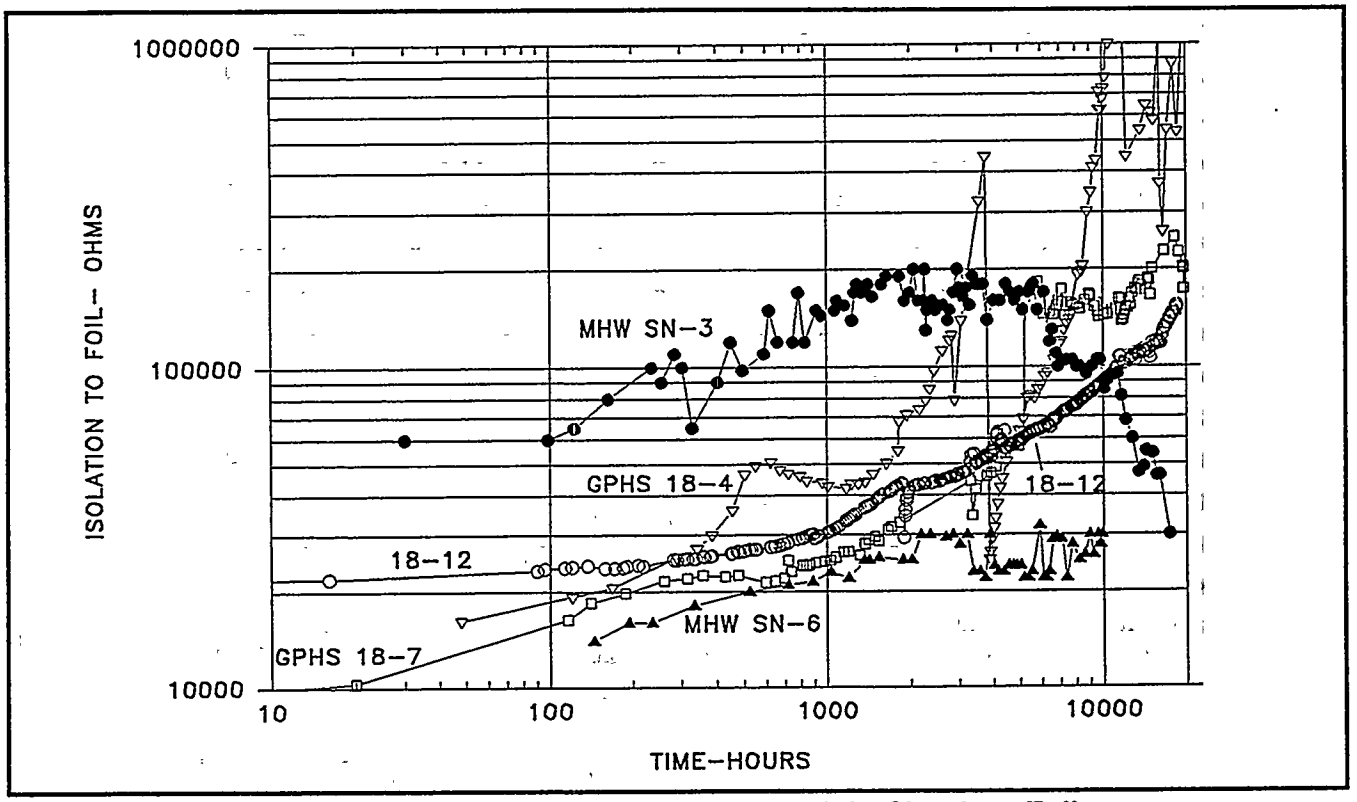

Figure 4-6. Isolation Resistance - Module Circuit to Foil (18-12, GPHS and MHW Modules) - (1035°C Operation)

Table 4-4. Comparison of Initial and 18,489 Hour Performance of Module 18-12 at 1035°C

	Initial 6/16/94	t = 18,489 Hours 9/29/96
Heat Input, Watts	169.15	169.6
Hot Shoe, °C Average	1035.9	1026.8
Hot Shoe Range, °C	5.7	4.0
Cold Strap, °C Average (8 T/Cs)	287.1	281.8
Cold Strap Range (8T/Cs)	5.0	5.0
Cold Strap Average (12 T/Cs)	282.7	277.4
Cold Strap Range (12 T/Cs)	19.8	19.4
Load Voltage, Volts	3.578	3.498
Link Voltage, Volts	0.155	0.153
Current, Amps	2.548	2.449
Open Circuit Voltage, Volts	6.431	6.897
Normalized Open Circuit (8T/Cs)	6.307	6.800
Normalized Open Circuit (12 T/Cs)	6.268	6.758
Average Couple Seebeck Coefficient (12)	497×10^{-6}	536.3×10^{-6}
Internal Resistance, Ohms	1.053	1.325
Internal Resistance Per Couple (Avg.)	0.0588	0.0736
Power Measured, Watts (Load + Link)	9.510	8.94
Power Normalized, Watts (8 T/Cs)	9.146	8.69
Power Normalized, Watts (12 T/Cs)	9.011	8.56
Power Factor	42.06×10^{-5}	39.07×10^{-5}
Isolation		
Circuit to Foil, Volts	-1.71	-0.86
Circuit to Foil, Ohms	21.3K	154K

Table 4-5. Module 18-12 Internal Resistance Changes

Position	Serial #	2nd Bond Milliohm	Preassy Milliohm	Delta ri Milliohm	T = 0 Milliohm	T=1,505 Hours	Delta ri Milliohm	Percent Increase	T=18,489 Hours	Delta ri Milliohm	Percent Increase
1.0	H2594	23.80	22.90	-0.90							
2.0	H2634	22.70	22.60	-0.10							
3.0	H2606	23.50	22.40	-1.10							
					176.80	192.10	15.30	8.65	219.00	42.20	23.87
4.0	H2168	22.20	21.70	-0.50	57.50	63.30	5.80	10.09	72.90	15.40	26.78
5.0	H2151	22.40	21.90	-0.50	57.40	62.90	5.50	9.58	72.10	14.70	25.61
6.0	H2256	22.20	21.70	-0.50	57.00	63.10	6.10	10.70	72.90	15.90	27.89
					171.20	188.60	17.40	10.16	217.10	45.90	26.81
7.0	H2597	24.40	23.20	-1.20							
8.0	H2680	22.60	23.00	0.40							
9.0	H2658	22.70	23.00	0.30							
					178.00	193.60	15.60	8.76	220.50	42.50	23.88
10.0	H1506	23.50	23.20	-0.30							
11.0	H1392	23.80	23.00	-0.80							
12.0	H1606	23.60	22.60	-1.00							
					176.20	193.40	17.20	9.76	221.30	45.10	25.60
13.0	H1344	23.60	23.50	-0.10	59.20	64.80	5.60	9.46	74.00	14.80	25.00
14.0	H1618	23.30	24.00	0.70	58.60	64.50	5.90	10.07	74.10	15.50	26.45
15.0	H1262	23.70	23.30	-0.40	59.40	65.00	5.60	9.43	74.30	14.90	25.08
					176.60	193.70	17.10	9.68	221.70	45.10	25.54
16.0	H1580	23.00	23.70	0.70							
17.0	H2127	22.80	22.10	-0.70							
18.0	H2113	22.90	22.20	-0.70							
					174.50	191.30	16.80	9.63	219.20	44.70	25.62

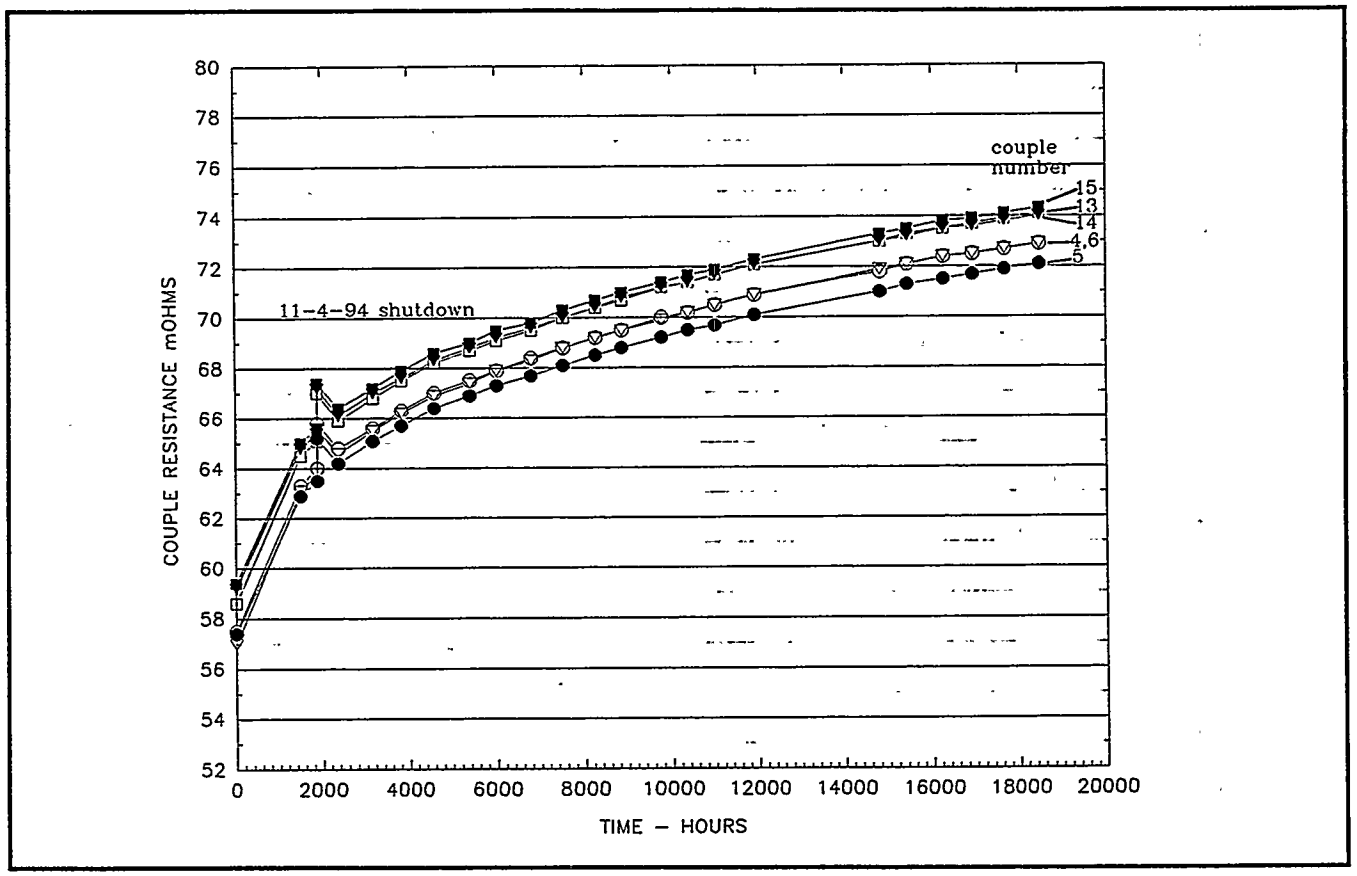

Figure 4-7. Individual Unicouple Internal Resistance Trends (Module 18-12)

Task 5

ETG Fabrication, Assembly, and Test

TASK 5 ETG FABRICATION, ASSEMBLY, AND TEST

E-6 and E-7 ETGs

Following long term storage, the E-6 ETG and E-7 ETG were transferred from their existing Converter Shipping Containers (CSCs) into refurbished and proof-loaded CSCs. The ETGs were repressurized and the CSCs were prepared for shipment to EG&G Mound. The E-6 ETG was in storage for 366 days and had been repressurized six times. The E-7 ETG was in storage for 51 days and not repressurized. At all times during storage, the ETG pressure was maintained at a minimum of 1.5 psi higher than the CSC pressure. The E-6 and E-7 ETGs were successfully shipped to Mound on 29 April and 6 May, respectively. ETG electrical and pressure measurements performed by Mound indicated no adverse effects from shipment.

E-7 Investigation Status

A topical report (GESP-7248) entitled "E-7 Processing Investigation" was issued this reporting period. The investigation concluded that the lower than expected E-7 isolation resistance observed during processing was most likely caused by the generation of aluminum vapor in the electric heat source (EHS) and condensation of this vapor on the silica wrap between the unicouples and foil insulation. It was also concluded that the source of the conductive deposit will be removed when the EHS is replaced by the isotope heat source and the deposit will have no adverse long term effect on the F-7 RTG performance.

Thermogravimetric Analysis (TGA) experiments performed at Battelle Columbus indicated that as the total pressure decreased at constant temperature, the reactivity of alumina with graphite increased. This result duplicated the trend seen during E-7 processing. It was also found that the mass loss rates of the E-7 ceramics were 3 to 5 times higher than for the E-6 ceramics.

The alumina used in the E-7 EHS was found to be different from that used in the E-6 EHS. The former was purchased on the Cassini program and the latter was purchased on the Galileo/Ulysses Program and was refurbished. Microstructure evaluation identified a smaller grain size (0.0004 inch for E-7 vs. 0.0006 inch for E-6), a similar

porosity of 3% and a smaller pore size for the E-7 alumina. These attributes could be responsible for the higher reactivity with graphite in the presence of moisture and carbon monoxide.

E-8 and Spare Converter Hardware

The E-8 Electric Heat Source (EHS) was assembled without thermocouple instrumentation. Purchase orders have been placed with two suppliers to provide the required thermocouple wire. One order is due in October and the other is due in November.

The E-8 shell and fin assembly has completed all paint overspray cleanup operations. The mounting holes were re-machined in accordance with the drawing requirements after the assembly completed the paint curing operation. Proof pressure and pressure drop testing of the ACS system were also complete. Customer review and acceptance will be performed during the next reporting period.

The spare PRD assembly successfully completed dynamic testing, bellows force testing and bellows leak testing. The assembly was conditionally accepted by the customer pending the final bellows leak test prior to launch.

All unicouples removed from E-7 have been reworked and inspected. A total of 144 unicouples were removed from E-7 and 126 were accepted after rework for a yield of 87.5 %.

Task 6

Ground Support Equipment (GSE)

TASK 6 GROUND SUPPORT EQUIPMENT (GSE)

GSE Hardware

The two shipping container bases that were previously used to store the E-6 and E-7 ETGs were proof loaded with the RTG cage and new attachment bolts. They were sent to Mound, along with a lifting yoke, in exchange for their two shipping container bases and lifting yoke. Refurbishment of this hardware to meet current configuration requirements is underway.

Two converter support ring assemblies were fabricated and sent to Mound for the new RTG transportation system. A third converter ring assembly was previously shipping to Westinghouse-Hanford for fit check purposes.

Task 7

RTG Shipping and Launch Support

TASK 7 RTG SHIPPING AND LAUNCH SUPPORT

Launch Activity

Trailblazer activities were completed at Cape Canaveral. One of its primary objectives was to determine a preferred method for hoisting the RTGs from ground level to level 14 where they will be attached to the spacecraft. Two methods were identified for evaluation: Option 1 was to hoist the RTGs from level 6 to level 14 without their shipping containers; Option 2 was to hoist the RTGs from level 6 to level 14 in their shipping containers. In both options the RTGs will be raised from ground level to level 6 in their shipping containers.

Based on the information gathered during Trailblazer, Option 1 was the approach recommended to DOE for the following reasons:

(a) It provided greater flexibility for recovery from potential crane problems on level 14;

(b) Option 2 would likely lengthen the time required to install all three RTGs because the time to maneuver all three shipping containers between level 6 and level 14 would be controlling;

(c) It required less work be performed in the more confined space of the air lock on level 14, where closer proximity to the RTGs could result in higher exposure levels.

LMMS personnel participated in Ground Operations Working Group meetings held at the launch facility. The Launch Site Support Plan and the Phase 3 Safety Report drafts were reviewed and comments provided to JPL.

Shipping Activity

LMMS witnessed the system acceptance test of the new RTG transportation system at KSC. Based on observations made during the test it was apparent that the routing of the RTG cables in the base of the package needed to be revised. A follow-up meeting was held at the trailer vendor's facility and revised routing and fastening anchor methods were agreed upon.

LMMS personnel observed the special instrumentation used during the road test of the second RTG transportation system unit. As requested, accelerometers were located

within the RTG package, and were mounted on the converter support ring (CSR). Initial indications obtained on the trip from Cincinnati to Miamisburg showed very low loads at the CSR. Westinghouse Hanford personnel plan to issue a test report on the complete road test.

Task 8

Designs, Reviews, and Mission Applications

TASK 8 DESIGNS, REVIEWS, AND MISSION APPLICATIONS

8.1 Galileo/Ulysses Flight Performance Analysis

No significant activity this reporting period.

8.2 Individual and Module Multicouple Testing

This task has been successfully completed.

8.3 Structural Characterization of Candidate Improved N- and P-Type SiGe Thermoelectric Materials

This task has been successfully completed.

8.4 Technical Conference Support

No significant activity this reporting period

8.5 Evaluation of an Improved Performance Unicouple *Module 18-Z*

This task has been successfully completed.

8.6 Solid Rivet Feasibility Study

This task has been successfully completed.

8.7 Computational Fluid Dynamics (CFD)

Work continues on the CFD task. Because this task is closely related to the Task 3 safety activities, technical progress is reported under that task.

8.8 Technical International Conference Support

This task has been successfully completed.

8.9 Additional Safety Tasks

Additional safety efforts have been assigned to this task. Because these efforts are closely related to the Task 3 safety activities, technical progress is being reported under that task.

8.10 SMALL RTG DESIGN STUDY

A small RTG Conceptual Design Study was conducted in the March to September 1996 time frame. The results were presented in August.

The conceptual designs which were evaluated included those previously proposed by Orbital Sciences Corporation and those proposed by Lockheed Martin. The system power level target was 70 watts, electrical, at the end of a ten year mission. GPHS fuel loading was treated parametrically for a range of fuel ages, from F-5 to new fuel, and the number of unicouples in each design option was varied to determine the optimum. Particular attention was paid to mechanical interfaces with the spacecraft and with ground handling and fuel loading equipment.

Baseline Description: A baseline design and four design options were evaluated. Each of the four options represented progressive design improvements to minimize mass, at the expense of development time or technical risk. The baseline design was a shortened version of the Cassini GPHS-RTG, sized for six GPHS modules rather than eighteen. This design incorporated 192 unicouples. No attempt was made to optimize the mass of the baseline design. The design of the heat source support system was retained, identical to that required for an eighteen GPHS module converter, except with no midspan support. The thermal insulation system consisted of 60 layers of molybdenum foil with layers of quartz cloth alternating with the foil.

Option 1 Description: The only changes from the baseline were to replace the three preload springs in the heat source system with a single spring which was sized for the lower axial preload required for six GPHS modules. This option had the minimum development risk of all the options considered.

Option 2 Description: For this option, the heat source support system was conceptually identical to Option 1; however, the individual components of the heat source support system were lightened to be compatible with the lower required preload for the small RTG. In addition, the PRD was downsized to be compatible with the lower internal volume of the small RTG.

A significant mass savings for this option resulted from replacement of the quartz cloth in the multifoil insulation system with zirconia powder. The technical risk for this change is regarded as moderate.

Option 3 Description: This option utilized design improvements representing significant technical risk. The most significant changes include a welded end closure at one end (in place of the bolted flange and C-seal arrangement), and a single stud heat source support system (in place of the four stud system used in Options 1 and 2). In addition, a graded multifoil insulation system with zirconia coated foils was employed.

Graded insulation utilizes selected variations in foil material through the thickness of the insulation packages depending on temperature. Lighter weight materials can be utilized on the cold side of the insulation package.

A variation of Option 3, utilizing a beryllium outer shell and end domes is representative of design changes that attain mass savings by use of alternate materials. The current study evaluated material selections that included carbon-carbon composites, aluminum beryllium composites and aluminum-lithium alloys along with beryllium, for the outer shell and fins.

Option 4 Description: Option 4 utilized four pyrolytic graphite heat source support studs at each end of the heat source stack. This concept offered the advantage of lower heat loss through the pyrolytic graphite stud material because the material has a low conductivity perpendicular to the layers. Because the material is weak in shear in the laminar direction, the support studs were positioned at an angle with the converter axis in order to take most of the load in compression. Finite element analysis indicated that a significant increase in preload and hence weight is required for this concept. When sized for the higher preloads, this approach was less attractive from a mass viewpoint.

Summary

The conceptual designs for Options 2, 3, and 4 are shown in Figure 8-1, and the power and mass summary is presented in Table 8-1.

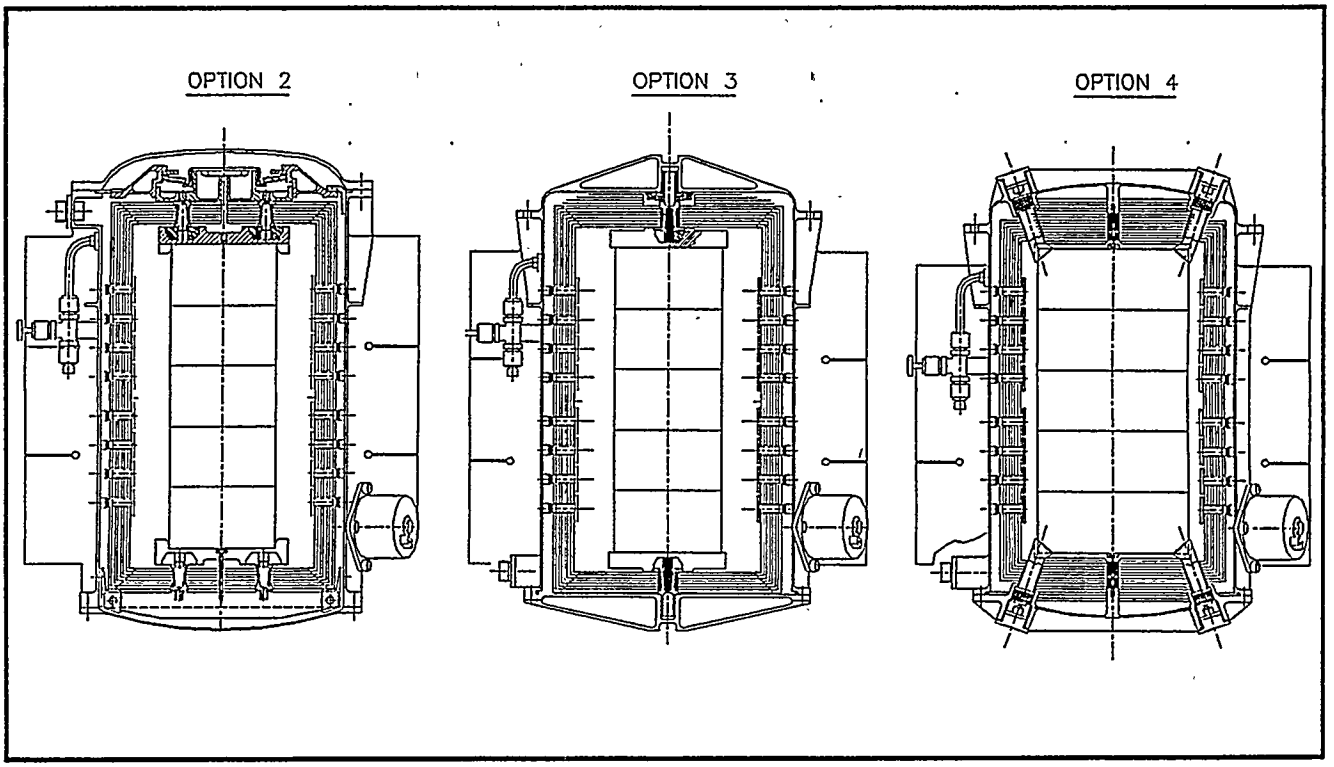

Figure 8-1. Small RTG Design Study Design Options

Table 8-1. Power and Mass Summary

Design Option	No. of Heat Source Modules	Fuel Source	Power at EOM (W)	Mass (kg)	Specific Power (W/kg)
1	5	F5	58	19.98	2.90
		F2, F6, F7	67	19.98	3.35
		New	71	20.17	3.52
	6	F5	70	22.45	3.12
		F2, F6, F7	81	22.45	3.61
		New	87	22.65	3.84
2	5	F5	61	18.20	3.35
		F2, F6, F7	70	18.20	3.85
		New	74	18.20	4.06
	6	F5	73	20.68	3.53
		F2, F6, F7	84	20.68	4.06
		New	88	20.68	4.26
3	5	F5	63	13.74	4.59
		F2, F6, F7	67	13.74	4.88
		New	71	13.74	5.17
	6	F5	76	16.22	4.69
		F2, F6, F7	81	16.22	4.99
		New	85	16.22	5.24
4	5	F5	61	13.43	4.54
		F2, F6, F7	65	13.43	4.84
		New	69	13.43	5.14
	6	F5	74	15.90	4.65
		F2, F6, F7	79	15.90	4.97
		New	83	15.90	5.22

Task 9

Project Management, Quality Assurance and Reliability, Contract Changes, Non-Capital CAGO Acquisition, and CAGO Maintenance

TASK 9 PROJECT MANAGEMENT, QUALITY ASSURANCE, AND RELIABILITY

9.1 Project Management

All weekly and monthly contractual reports and CDRLs were delivered on schedule.

LMMS personnel participated in the quarterly and monthly Cassini Program reviews during the reporting period. They also supported the Trailblazer activities and launch planning reviews at the Cape as well as witnessing the RTG transportation acceptance test.

The E-7 ETG Pre-Ship Review was held at Valley Forge in April and the E-6 and E-7 ETGs were delivered to Mound in May.

LMMS personnel supported the F-5 RTG Buy-Off Meeting, F-2 testing, and the F-7 RTG assembly operations at Mound during this reporting period.

E-8 component construction continues. With the exception of thermocouple wire for the EHS, it is expected that the E-8 kits and packaging will be completed by the end of the year.

Attached are the Cassini RTG program calendars showing 2Q96, 3Q96, and 4Q96 program meetings and important related events.

No significant environmental, health, or safety incidents occurred during this period.

9.2 Quality Assurance

Quality Plans and Documents

No plans were initiated or modified during this period.

Process Readiness and Production Readiness Reviews

No readiness reviews were conducted this month.

Quality Control in Support of Fabrication

E-6 Converter: The E-6 converter was delivered to Mound at the beginning of May.

E-7 Converter: The E-7 converter was removed from the LAS in April and placed in long-term storage in preparation for shipment to Mound. Two Class I Non-Conformance reports were written and dispositioned and a conditional Certificate of Inspection was received. NR79286 was issued because of an overweight condition. The total weight was estimated to be 67.42 lbs. versus a specifcation limit of 67 lbs. NR79348 was written to address the abbreviated acceptance testing caused by the degradation in isolation resistance. Both NRs were dispositioned (preliminary) to continue fueling and testing. The ETG was shipped to Mound on May 6.

E-7 Unicouple Rework : All of the unicouples removed from the E-7 converter have been reworked and dispositioned, with most being accepted and placed back in stock.

E-8 Converter Assembly: Work on sub-assemblies for the E-8 converter is continuing. E-8 hardware is being assembled into kits to facilitate converter assembly at a future date, if required.

Assembly of the EHS for E-8 has been successfully completed, less thermocouple installation. Procurement of acceptable thermocouple wire is in process. Work is continuing on obtaining customer acceptance of E-8 parts such as the inboard pressure dome, shell and fin assembly, flex hoses, and other parts.

Shipping Containers

Inspection and rework is continuing on shipping containers to assure acceptance to the latest drawing revisions. Shipping containers and associated lifting equipment are being proof loaded to meet requirements for handling at the Cape for launch support.

Material Review Board

There were no Class I (major) nonconformances generated this reporting period. Preliminary dispositions were accepted for E-7 NRs 79286 and 79348.

Quality Assurance Audits

There was no activity in this area during this reporting period.

Quality Assurance Status Meeting

There were no meetings held during this period.

Task H

Contract Acquired Government-Owned Property (CAGO) Acquisition

TASK H CONTRACTOR ACQUIRED GOVERNMENT OWNED (CAGO) PROPERTY ACQUISITION

Task H.1 CAGO Unicouple Equipment

No significant activity during this reporting period.

H.2 CAGO - ETG Equipment

No significant activity during this reporting period.

H.3 CAGO - MIS

No significant activity during this reporting period.

Program Calendars

Cassini RTG Program Calendar

As of 3 July 1996

2nd QTR 1996

	M	T	W	T	F	S	S	FW
APRIL	1	2	3 Pre-Ship Review of E-7 ETG Converter - Valley Forge -	4	5	6	7	14
	Trailblazer Activities							
	8	9 Dynamic Test - Mound - Miamisburg, OH *Rosko/Kauffman*	10	11 Cassini Quarterly Program Review - JPL - CA - *Hemler, Cockfield, Reinstrom, DeFillipo, Kelly, Haley*	12	13	14	15
	Trailblazer Activities							
	15	16 Fireball Meeting - Sandia Nat'l Labs - *DeFillipo/Chang*	17	18	19 Semi-Annual Reports Due to DOE	20	21	16
	22	23 Monthly Reports Due to DOE	24	25	26	27	28	17
MAY	29 Ship E-6 to Mound	30 F-5 Buy-Off - Mound - Miamisburg, OH *Reinstrom/Cockfield/ Douglas*	1	2	3	4	5	18
	6 Ship E-7 to Mound	7 FSII Briefing - Kirtland AFB, NM - *DeFillipo/Rosko*	8 INSRP Review Fireball Model - Kirtland AFB, NM - *DeFillipo/Chang/Deane/Rosko*	9 E-7 Processing Investigation Coupon Test - Valley Forge -	10	11	12	19
	13	14	15	16	17	18	19	20
	20	21	22 Magnetics Testing EG&G Mound, Miamisburg, OH *Reinstrom/Kugler*	23 Monthly Reports Due to DOE	24	25	26	21
JUNE	27	28	29	30	31	1	2	22
	3 DFSAR Vol I Review - DOE HQ - *Hartman*	4 RTG Transportation System Final System Acceptance Test - Cape Canaveral, FL - *Reinstrom./Cockfield/Haley*	5	6 INSRP Review Reentry Analysis Results - Valley Forge - Bldg. B - *DeFillipo et al*	7	8	9	23
	10 Mass Properties Test - EG&G - Mound - *Gosling*	11 Cassini Monthly Program Review - OSC - *Hemler, et al*	12	13	14	15	16	24
	17 Module Assembly Readiness Review - EG&G - Mound - *Cockfield*	18	19 Dynamic Test Check Out - Mound- *Kauffman* Launch Planning - Cape Canaveral, FL - *Reinstrom*	20 DFSAR Vol II Review - DOE HQ - *DeFillipo et al*	21 Monthly Reports Due to DOE	22	23	25
	24	25	26 DFSAR Vol III Review - Valley Forge - *DeFillipo et al*	27	28 AIAA Nuclear Space Power Meeting - Washington, DC *Hemler*	29	30	26

Cassini RTG Program Calendar

As of 2 October 1996

3rd QTR 1996

	M	T	W	T	F	S	S	FW
JULY	1	2 DOE/HNUS Review of DFSAR - Valley Forge - *DeFillipo/Ruiger/Firstenburg*	3	4	5	6	7	27
	8	9	10	11	12	13	14	28
	15	16	17	18	19	20	21	29
	22	23 Monthly Reports Due to DOE	24 Cassini Quarterly Program Review - OSC, Germantown, MD - *Hemler, Cockfield, Reinstrom, DeFillipo*	25 F-2 Vibration Test - EG&G Mound - Miamisburg, OH - *Haley/Rosko/Kauffman/Rickenbach*	26	27	28	30
AUGUST	29	30	31	1	2	3	4	31
	5	6	7	8 GPHS EGA Reentry Event Tree Probabilities - JHU/APL - *DeFillipo/ Letts/ Ha/ Tobery / Kampas*	9	10	11	32
	12	13 RTG Data Package and P/FR Classification - EG&G Mound - *Reinstrom*	14	15	16	17	18	33
	19 F-7 Assembly Segment Readiness Review - EG&G Mound - *Reinstrom*	20	21	22	23 F-7 Assembly - EG&G Mound - Miamisburg, OH *Cockfield* Monthly Reports Due to DOE	24	25	34
SEPTEMBER	26	27 Rad Worker Training - EG&G Mound - *Haley/Dickinson*	28 RTG Adapter Fit Check - EG&G Mound - *Haley/Dickinson*	29 Small RTG Design Review - OSC, Germantown - *Hemler, et al* Full Stack Intact Impact INSRP Briefing - JPL - Pasadena, CA *DeFillipo/ Rosko / Chan*	30	31	1	35
	2 Labor Day 	3 F-2 T/V Segment Readiness Review - EG&G Mound - *Kelly/Klee*	4 F-7 Assembly Support - EG&G Mound - *Gosling* MET/BEES INSRP Meeting - LMMS San Jose -	5 PSSP/LASP INSRP Meeting - LMMS Valley Forge -	6	7	8	36
	9	10	11	12	13	14	15	37
	16	17	18 Cassini Montly Program Review - OSC, Germantown, MD - *Hemler/Reinstrom/ DeFillipo*	19 F-7 Assembly Support - EG&G Mound - Cockfield/Douglas	20	21	22	38
	23 Monthly Reports Due to DOE	24	25	26	27	28	29	39

Cassini RTG Program Calendar

As of 16 October 1996

4th QTR 1996

	M	T	W	T	F	S	S	FW
OCTOBER	30	1 F-7 Dynamic Test Support - EG&G Mound - Haley/Kauffman	2 DOE Review of Volume I - FSAR - Valley Forge - DeFillipo/Hartman	3	4	5	6	40
	7	8	9	10	11	12	13	41
	14	15	16	17	18 Annual and Semi Annual Reports Due to DOE	19	20	42
	21	22	23 Monthly Reports Due to DOE	24 DOE Review of Volume II - FSAR - Valley Forge - DeFillipo, et al	25	26	27	43
NOVEMBER	28	29	30 Quarterly Program Review - OSC, Germantown, MD - Hemler/Cockfield/ Reinstrom	31	1	2	3	44
	4	5	6	7	8	9	10	45
	11	12	13	14	15	16	17	46
	18	19	20	21	22 Monthly Reports Due to DOE	23	24	47
DECEMBER	25	26	27	28	29	30	1	48
	2	3	4	5	6	7	8	49
	9	10	11	12	13	14	15	50
	16	17	18	19	20	21	22	51
	23 Monthly Reports Due to DOE	24	25	26	27	28	29	52